

ABSTRACT

CRAFT, HUGHES SPALDING. Spectroscopy of Oxide-GaN Interfaces. (Under the direction of Jon-Paul Maria.)

GaN-based devices are of interest for applications requiring high-frequency, high-power operation at elevated temperatures. As in traditional, silicon-based devices, integration of semiconducting phases with insulators is critical. Additionally, applications involving the integration of GaN with polar oxides such as perovskite ferroelectrics have been proposed, due to the coupling that may be achieved between the respective polar vector. Devices utilizing such a coupling behavior would make possible two-dimensional electron gases of high charge densities that could be modulated by the oxide's polarization. The current status of oxide-GaN research is far behind that of oxide-Si research, and large-scale realization of GaN devices will require detailed understanding of oxide-GaN interfaces. This thesis focuses on the characterization of several oxide-GaN interfaces using x-ray photoelectron spectroscopy (XPS), as well as the identification of issues relating to the GaN surface.

The rocksalt oxides MgO and CaO have been proposed as candidates for GaN MOSFET gate oxides, passivating layers, and buffer layers in GaN-ferroelectric structures. Thus, knowledge of film growth modes and band alignments is critical. Utilizing *in-vacuo* molecular beam epitaxy (MBE) and XPS, the growth of MgO on GaN was found to occur by the Volmer-Weber mode, with coalescence occurring at ~12 nm. This coalescence behavior was not found to affect the band alignment. As measured by XPS, the valence band offset at the MgO-GaN interface is 1.2 ± 0.2 eV, leading to a conduction band offset of 3.5 eV.

A similar study was undertaken for the CaO-GaN system, in which more rapid coalescence was observed, leading to the conclusion of a Stranski-Krastanov growth mode. The difference in coalescence behavior is attributed to the increased reactivity of the CaO surface. The band offsets at the CaO-GaN interface were found to be 1.0 ± 0.2 eV at the valence band, and 2.5 eV at the conduction band. The band structures measured in this thesis are considered to be sufficient for limiting leakage current by Schottky emission for high-temperature devices.

Surface chemical stability of rocksalt oxides is a known issue with respect to hydroxylation through water adsorption. XPS characterization of water uptake was performed using the O 1s photoelectron line after several *in-vacuo* exposures, culminating in a one-hour exposure to a water/oxygen mixture at 1×10^{-6} Torr. Characterization of polycrystalline MgO showed a saturating coverage of -OH groups at approximately 1 monolayer, regardless of exposure. CaO films exhibited increased reactivity, with hydroxyl coverage increasing to 3 monolayers, in addition to a similar amount of physisorbed water, suggesting the possibility for further reaction. Complete recovery of both oxide surfaces is shown to be achievable using mild vacuum anneals.

Finally, the surface of GaN has been characterized with respect to several issues encountered during these investigations. GaN surfaces are found to be significantly Ga-rich, with surface stoichiometries routinely in excess of Ga₂N. Several wet chemistries for GaN preparation were evaluated for their ability to modify the electrical behavior of subsequently grown oxide films. XPS could not unambiguously identify any change in surface chemistry that promotes these effects. Finally, p-type GaN films were noted to consistently possess greater oxide contamination in the as-grown state. Typical n-type or

undoped GaN were marked by submonolayer quantities of oxide surface coverage, while p-type GaN typically exhibited coverages in the 1-2 nm scale. This difference has been found to be due to the p-type dopant activation anneal, during which GaN oxidation cannot be suppressed.

Spectroscopy of Oxide-GaN Interfaces

by
Hughes Spalding Craft

A dissertation submitted to the Graduate Faculty of
North Carolina State University
in partial fulfillment of the
requirements for the Degree of
Doctor of Philosophy

Materials Science and Engineering

Raleigh, North Carolina

2009

APPROVED BY:

Dr. Zlatko Sitar
Professor of Materials Science

Dr. Donald Brenner
Professor of Materials Science

Dr. Thomas Pearl
Assistant Professor of Physics

Dr. Jon-Paul Maria
Associate Professor of Materials Science
Chair of Advisory Committee

Biography

Spalding Craft was born in Atlanta on April 22, 1982, to proud parents Spalding, Sr. and Sandy Craft. A six-year career in catholic school served him well in establishing a lifelong desire to learn, while a longer stint in public schools taught a healthy distrust of authority figures. Spalding moved with his family to Morehead City, NC in 1991, where he attended Morehead City Middle School and West Carteret High School, finally developing a late-blooming aptitude for science and math that would eventually lead to his career in engineering at North Carolina State University.

At NC State, Spalding arrived in 2000 fully expecting to pursue a degree in aerospace engineering, but instead was beguiled by a materials science demonstration in an Introductory Engineering course. The exhibits of work hardening, annealing, and shape memory alloys had little to do with Spalding's eventual interest in electronic materials, but they presented fundamentally satisfying explanations for materials behavior that are observed daily, and so appealed to Spalding's general curiosity about phenomena in general.

Spalding stayed at NC State for graduate school, having found the research he wanted to do in the laboratory of Prof. Jon-Paul Maria. Starting with oxide MBE of rare earth oxides on silicon, Spalding moved on to the spectroscopic investigations of oxides on gallium nitride presented in this dissertation. After obtaining his PhD in materials science, Spalding will continue to work in the NC Research Triangle area at Hexatech, where he will be involved in the bulk growth of aluminum nitride for future substrate applications.

Acknowledgements

First and foremost, I owe a tremendous debt of gratitude to my advisor and friend, Prof. Jon-Paul Maria. Without his guidance, my graduate career would not have been nearly as successful or enjoyable. Whether through mysteriously prescient processing advice, the Midas touch with equipment, or a well-timed, insightful question, JP was always able to keep nudging me in the right direction throughout my time at NC State, and I will always be grateful for that.

I would be remiss if I did not express my sincere thanks for Dr. Ramon Collazo, who was always an enthusiastic surrogate advisor in all matters spectroscopic. Ramon never hesitated to take time away from his own work to teach me about some new aspect of XPS I was running into, or to zealously engage in endless arguments about details of data interpretation. I never left a conversation with Ramon without having learned something new.

The past and current members of JP's Electronic Oxides Group, and the other student denizens of RB1, have been integral to my success and enjoyment at NC State. To Brian, Jon, Dipankar, Alissa, Seymen, Beth, Peter, Jess, Michelle, Mark, James, Seiji, Xianglin, and Tony, thanks for making a better difference. My tenure as a grad student would not have been the same without the long Bojangles lunches, golf, Text Twist, and late-night arm biting incidents. I have truly been lucky to be part of such a tightly knit group of students, and I can't imagine grad school without it.

Finally, I wouldn't have been able to do any of this without my family. To my parents, my sister, and Beth: there's just no way I would have made it through eight and a half years of school without your love and support. Thank you for being there when things got crazy, and sharing my successes with me. I couldn't have done it without you guys!

Table of Contents

List of Tables	viii
List of Figures	ix
1. Semiconductor Interfaces	1
1.1 Metal-Semiconductor Contacts	2
1.1.1 <i>The Schottky-Mott Rule</i>	2
1.1.2 <i>The Bardeen Limit</i>	4
1.1.3 <i>The Development of MIGS Theory</i>	11
1.2 Semiconductor Heterostructures	20
1.2.1 <i>The IFIGS Model</i>	20
1.2.2 <i>Correlating Experiment and Theory</i>	23
REFERENCES	26
2. X-ray Photoelectron Spectroscopy	28
2.1 Historical Development	29
2.1.1 <i>Early Experiments</i>	29
2.1.2 <i>Modern XPS</i>	31
2.2 Fundamentals of XPS	33
2.2.1 <i>Practical Aspects of Theory</i>	33
2.2.2 <i>Instrumentation</i>	40
2.3 Techniques of Interest	46
2.3.1 <i>Surface Composition Measurements</i>	47
2.3.2 <i>Thin Film Growth Modes</i>	48
2.3.3 <i>Band Offset Measurements</i>	53
REFERENCES	57
3. Materials	62
3.1 Gallium Nitride	62
3.1.1 <i>Properties of GaN</i>	63
3.1.2 <i>GaN Growth: Controlling GaN Polarity</i>	73
3.2 Dielectrics on GaN	81
REFERENCES	86
4. Experimental Procedure	90
4.1 Experimental Equipment	90
4.1.1 <i>Surface Analysis Chamber: XPS</i>	91
4.1.2 <i>Molecular Beam Epitaxy: Film Growth</i>	93
4.1.3 <i>Annealing Chamber: Surface Preparation</i>	95
4.1.4 <i>Electron Beam Evaporator: Metal Deposition</i>	96
4.1.5 <i>Additional Equipment</i>	96

4.2 Substrate Preparation.....	97
4.3 Experimental Details	98
4.3.1 Growth Mode Measurements	98
4.3.2 Band Offset Measurements	100
REFERENCES	102
5. Band offsets and growth mode of MBE-grown MgO (111) on GaN (0002) by X-ray photoelectron spectroscopy.....	103
Abstract	104
Introduction	105
Experimental Procedure	106
Results and Discussion.....	108
<i>Characterization of MgO Growth Mode</i>	108
<i>Band Offset Measurements</i>	110
Conclusion	117
Acknowledgements	118
REFERENCES	119
6. Spectroscopic analysis of the epitaxial CaO (111) - GaN (0002) interface	120
Abstract	121
Introduction	122
Results and Discussion.....	124
Conclusion	130
Acknowledgements	130
REFERENCES	131
7. Surface water reactivity of polycrystalline MgO and CaO films investigated using x-ray photoelectron spectroscopy	132
Abstract	133
Introduction	134
Experimental Procedure	135
Results and Discussion.....	137
Conclusion	145
Acknowledgements	146
REFERENCES	147
8. GaN Surfaces.....	148
8.1 Surface Stoichiometry	148
8.2 GaN Chemical Treatments	158
8.3 Surface oxidation differences arising from GaN doping.....	164
REFERENCES	169
9. Conclusions and Future Work.....	170

9.1 Conclusions.....	170
9.2 Future Work.....	173
Appendix	175
Band offsets of SrTiO ₃ , GdScO ₃ /SrTiO ₃ , and LaAlO ₃ /SrTiO ₃ epitaxial heterostructures with (0001) GaN	175
REFERENCES	184

List of Tables

Table 2.1: Characteristics of common x-ray sources ³⁰	43
Table 3.1: Summary of the band gap (E_G), hole mobility (μ_n), saturation electron velocity (V_{sat}), critical electric field (E_C), thermal conductivity (λ), and dielectric permittivity (ϵ_r) of GaN, and several other semiconductors.	63
Table 5.1: Summary of XPS data used for valence band offset calculations.	115
Table A.1: Summary of band offsets determined for the heterostructures in this study.....	187

List of Figures

Figure 1.1: Schematic band diagram of Schottky's space charge model for rectifying metal-semiconductor contacts.	2
Figure 1.2: (a) Band diagram illustrating Bardeen's modification to the Schottky-Mott model; note the schematic depiction of surface gap states. (b) Plot comparing the degree of band bending to the relative densities of surface and space charge.....	6
Figure 1.3: Demonstration of the effect surface states may have on semiconductor surfaces, using a <i>p-n</i> junction.....	8
Figure 1.4: Modification of the plot given in Figure 1.2b, with the addition of the first electric field term of Equation 1.8	9
Figure 1.5: Plot from Kurtin, <i>et al.</i> showing slope parameter S versus Pauling ionicity ΔX for various dielectric materials	16
Figure 1.6: Kurtin <i>et al.</i> 's data after Schlüter's rescaling of S to S_x	17
Figure 1.7: Mönch's data showing the quadratic relationship between the slope parameter and the electronic polarizability.....	19
Figure 1.8: Schematic band diagram showing two semiconductors in intimate contact.....	34
Figure 2.2: Plot of the electron inelastic mean free path for electrons of kinetic energies up to >1000 eV	36
Figure 2.3: Model demonstrating the origin of the XPS chemical shift in terms of the change in valence band electron density upon oxidation of metallic lithium	39
Figure 2.4: Greatly simplified diagram of an XPS analysis chamber	41
Figure 2.5: Diagram of a typical XPS x-ray source, showing the usual dual-anode arrangement with the aluminum anode in operation.....	44
Figure 2.6: Schematic showing the operating principles of the concentric hemispherical analyzer.....	45
Figure 2.7: The three essential thin film growth modes	49
Figure 2.8: Plot of theoretical photoelectron intensity attenuation versus thickness for the three thin film growth modes.....	52
Figure 2.9: Generic band diagram showing the measurements necessary for determining valence band offsets	54
Figure 3.1: The electron drift velocities versus electric field for Si, GaAs, InP, and GaN ...	65
Figure 3.2: A comparison of the temperature dependence of the intrinsic carrier concentration of Si, SiC, and GaN.....	67
Figure 3.3: The structure of GaN viewed along [110], inclined slightly towards the c axis, using Ga- or N-centered tetrahedral to visualize the polarity.....	70
Figure 3.4: Structure forming a 2DEG (in red) at the AlGaN/GaN interface, and schematic band diagram showing the conduction band of GaN bending below the Fermi level at the interface, thus inducing the 2DEG	72
Figure 3.5: The use of the intrinsic polarity of the wurtzite structure to control the location and sign of the carrier gases at AlGaN/GaN interfaces.....	73

Figure 3.6: Ga supersaturation as a function of V/III ratio and F ratio	78
Figure 3.7: Schematic interfacial bonding arrangements for N- and Ga-polar GaN on a sapphire substrate	80
Figure 4.1: Schematic diagram of the Sitar surface analysis cluster	91
Figure 5.1: Comparison of integrated intensity of Ga 2p photoelectric peak with theoretical predictions as MgO thickness increases	110
Figure 5.2: Representative XPS data showing Ga 3d and Mg 2p core levels, and the corresponding valence band regions (insets)	113
Figure 5.3: Simplified band diagram of MgO/GaN interface	117
Figure 6.1: Comparison of Ga 2p integrated intensity as CaO thickness increases with prediction for two-dimensional film growth	125
Figure 6.2: Schematic illustration of the relative coalescence behaviors of CaO and MgO on GaN (0002).	127
Figure 6.3: Sample spectra showing Ga 3d and Ca 3p core levels as well as valence band spectra from bare GaN and 40 nm CaO, respectively	128
Figure 6.4: Simplified band diagram of the CaO/GaN interface	129
Figure 7.1: XPS survey scans of (a) MgO and (b) CaO polycrystalline films used in this study.	138
Figure 7.2: O 1s photoelectron spectra of MgO film following various exposures.	139
Figure 7.3: O 1s photoelectron spectra of CaO film following various exposures.	141
Figure 7.4: O 1s spectra comparing CaO surface following 500 °C recovery anneal to as-deposited surface	143
Figure 7.5: Free energies for the bulk reactions of CaO and MgO with water to form hydroxide phases	144
Figure 8.1: Representative data showing the Ga 2p _{3/2} and N 1s photoelectron line from an undoped GaN sample	150
Figure 8.2: Ga 2p _{3/2} and N 1s photoelectron lines taken from GaN exposed to Ar ion beam sputtering for ten minutes at 600 °C.	152
Figure 8.3: Evolution of surface stoichiometry of p-type GaN following one-hour vacuum anneals at 700, 800, and 900 °C	153
Figure 8.4: Survey scans taken using Mg K α radiation of GaN surfaces subsequent to each annealing stage	154
Figure 8.5: Ga:N ratio vs. Ga supersaturation for several GaN films	155
Figure 8.6: Ga:N ratio as a function of growth time	157
Figure 8.7: O 1s photoelectron spectra of untreated GaN, the standard HCl-HF etch, and the HCl-buffered HF etch	160
Figure 8.8: Atomic force microscopy images of GaN surfaces after the denoted chemical treatments	161
Figure 8.9: Valence band spectra of the GaN surface after the HCl-HF etch (red), and the HCl-HF:NH ₄ F etch (blue)	162
Figure 8.10: XPS scans of Cl 2p core level photoelectron lines of GaN surfaces exposed to an HCl-last treatment and the standard HCl-HF treatment.	163

- Figure 8.11:** O 1s core levels comparing the surface oxygen contamination for p- and n-type GaN surfaces. 165
- Figure 8.12:** Survey scans using Al K α radiation illustrating the relative contamination differences arising from the p-type dopant activation anneal. 167
- Figure 8.13:** O 1s core level scan of an unactivated p-type GaN surface. 168
- Figure A.1:** RHEED images collected along the substrate $\langle 11\bar{2}0 \rangle$ azimuth of (a) GaN, (b) 5 ML (100)-oriented TiO₂, (c) 2 nm (111)-oriented SrTiO₃, (d) 40 nm (111)_p-oriented GdScO₃, and (e) 40 nm (111)_p-oriented LaAlO₃. 188
- Figure A.2:** (a) θ - 2θ and scan of a 40nm LaAlO₃ / 2nm SrTiO₃ / (0001)-oriented GaN heterostructure. (b) Azimuthal ϕ -scans of the LaAlO₃ $20\bar{2}4$ family (top) ($\chi=35.33^\circ$) and GaN $10\bar{1}1$ family (bottom) ($\chi=28.03^\circ$) with 0° aligned parallel to the $[10\bar{1}0]$ GaN direction. 189
- Figure A.3:** X-ray photoelectron spectra of the (a) Ga 3d, (b) Ti 3p, (c) Al 2p, and (d) Sc 3p photoelectron lines 190
- Figure A.4:** Simplified schematic band diagram of the (a) LaAlO₃ / SrTiO₃ / GaN interface and (b) GdScO₃ / SrTiO₃ / GaN interface. 191

1. Semiconductor Interfaces

The electronic properties of semiconductor interfaces constitute a central theme of the research to be presented in this thesis. Of those properties, the band alignment (or the mutual offsets between the conduction bands and valence bands of the two phases) is perhaps the most critical, as it establishes the conditions of current transport across the interface: the extent to which it can occur and the mechanisms that will govern it. Therefore, the mechanisms that establish this band lineup are worth investigating.

This chapter presents a review of those mechanisms in the form of a historical outline of the research aimed at understanding these interfaces. The formation of metal-semiconductor contacts is reviewed in somewhat greater detail than semiconductor heterostructures, as the debate over these contacts lasted for nearly three quarters of a century, and the understanding of Schottky barriers led to a much more rapid understanding of heterostructures.

The state-of-the-art understanding of metal-semiconductor contacts evolved from the simplistic Schottky-Mott Rule (1938), to the Bardeen limit (1947), in which surface and interfacial effects are considered, to the most recent elucidations of the Metal-Induced Gap States (MIGS) theory (~1980-2000). The present MIGS theory is finally accepted and has a strong theoretical and experimental basis. The advent of high-quality heterostructures prompted the relatively rapid adoption of MIGS theory (such as it was) to explain their band alignments in the late 1970's. Thus, with a reasonably thorough understanding of the

mechanisms governing the formation of Schottky contacts, the behavior of semiconductor heterostructures will be seen to be analogous, and comparatively easy to understand.

1.1 Metal-Semiconductor Contacts

1.1.1 The Schottky-Mott Rule

The unusual properties of metal-semiconductor contacts were first observed by Braun in 1874,¹ who observed rectification behavior in Cu/Cu₂O contacts. Their commercial use followed quickly, but it was not until 1938, when Schottky published his paper² proposing the formation of a depletion layer extending into the semiconductor from the metal-semiconductor interface, that sustained research investigating the mechanisms underpinning the devices began in earnest. Schottky's proposed mechanism for rectifying behavior is shown schematically in Figure 1.1, for an n-type semiconductor.

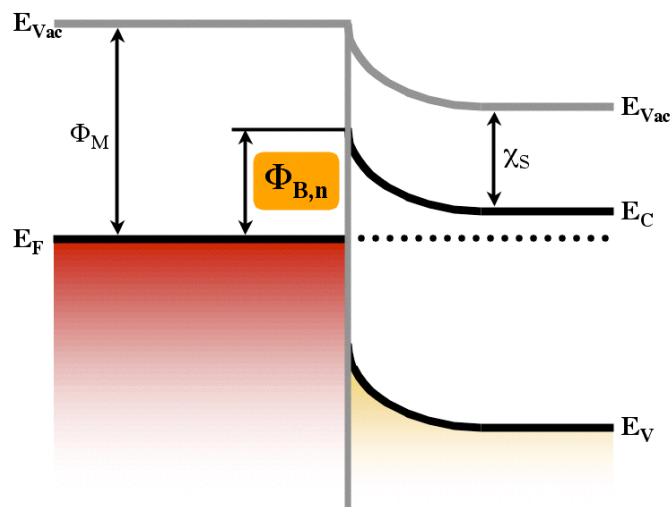


Figure 1.1: Schematic band diagram of Schottky's space charge model for rectifying metal-semiconductor contacts.

In Schottky's model, the metal and semiconductor form a clean, abrupt interface. The semiconductor surface is assumed to be bulk terminated, and consequently, no surface states are present, and no band bending occurs until the semiconductor and metal are brought close to one another. As the two materials make contact, charge transfer at the interface occurs in order to bring the Fermi levels into equilibrium. If the work function, Φ_M , of the metal is larger than that of the semiconductor, as is the case in Figure 1.1 above, then electrons are transferred from the semiconductor into the metal, consequently a depletion region and a space charge layer form in the semiconductor. In the metal, the charge incurred by the interface formation is screened over atomic distances, and thus the band bending is negligible. In the semiconductor, the electric field is screened over a much larger distance, as described by the Debye length, typically on the order of 10 nm.³ Thus, the degree of rectification is determined by the amount of band bending in the semiconductor.

Schottky finalized his theory in 1940,⁴ and Mott in 1938⁵ arrived independently at the same rule for determining the magnitude of the barrier height Φ_B at the metal-semiconductor contact:

$$\Phi_{B,n} = \Phi_M - \chi_S, \quad [1.1]$$

where the subscript B,n refers to the barrier height for an n-type semiconductor. For a given semiconductor, the behavior of the junction can be varied from ohmic, using a low work function ($\Phi_M < \chi_S$) metal, to rectifying ("Schottky" behavior) using a high work function metal. The barrier height scales linearly with the metal work function. This leads to the

definition of the Slope Parameter, S , which describes the variation of the barrier height with the metal work function, for a particular semiconductor:

$$S \equiv \frac{d\Phi_B}{d\Phi_M}. \quad [1.2]$$

For a semiconductor following the Schottky-Mott rule, $S = 1$. The use of an identical model, with appropriate changes in sign, can be used to derive a similar relationship for the barrier height on a p-type semiconductor.

Experimental work to test this theory was performed quickly, but the data for the semiconductors of interest at the time (Ge, Se, and Cu_2O) did not match Schottky's predictions, and thus much of it was not published until later. For a summary of some early experimental work that suggested the insufficiency of Schottky's theory, see ref [6].

1.1.2 The Bardeen Limit

Although the Schottky-Mott rule established an important basis for the interpretation and prediction of metal-semiconductor contacts, its inadequacy was quickly apparent, as the behavior of most semiconductors was found to deviate significantly from a linear, one-to-one variation in barrier height with metal work function. The first substantive insight into the failure of this theory was proposed in 1939, but not seriously adopted until much later. In 1939 Shockley theorized, building on earlier work from the Soviet Union, that for a one-dimensional crystal, surface states must exist as a result of the termination of the crystal periodicity.⁷ Extending his model to three dimensions, Shockley concluded that there should

be one surface state per surface atom, existing in a half-filled band. These states decay exponentially into the crystal, and their energies reside within the band gap. The existence of surface states, whether intrinsic or extrinsic, provides the central paradigm for all further understanding of semiconductor junctions.

Bardeen, in 1947, identified the two essential deficiencies of the Schottky-Mott rule. First, he pointed out that the work function of either surface contains a term due to the surface dipole, and thus its value may be modified by the formation of the contact. Second, he utilized Shockley's argument of surface states to explain the experimental observations of metal-semiconductor junctions with slope parameters of much less than one.⁶ Bardeen's contribution is fundamental to further understanding of semiconductor contacts, so some attention will be given to its derivation here. The basic quantities needed are given in the metal-semiconductor band diagram, again for an n-type semiconductor, shown in Figure 1.2a. Here, the important quantity to note is ϵ_s , or the topmost energy level of surface states within the band gap, referenced to the bottom of the conduction band.

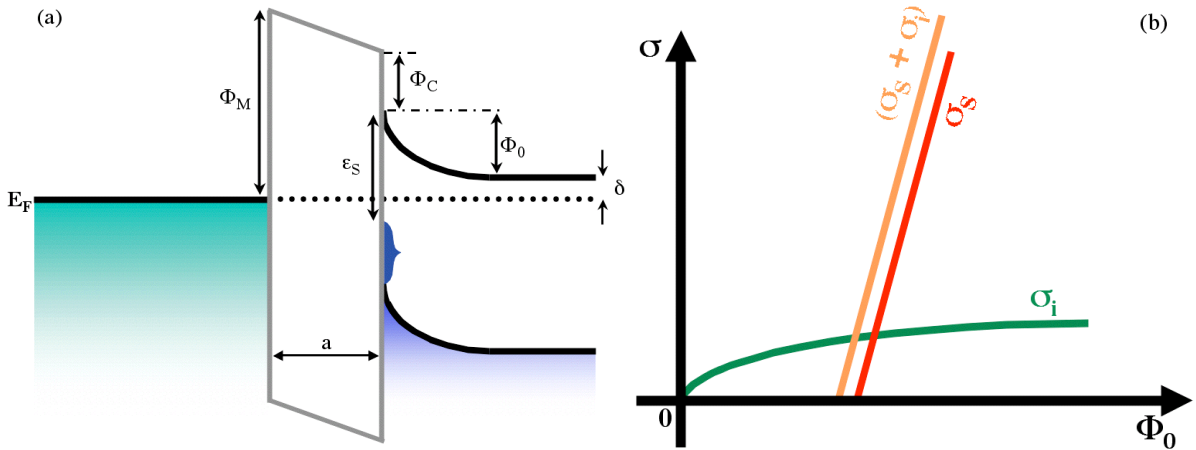


Figure 1.2: (a) Band diagram illustrating Bardeen's modification to the Schottky-Mott model; note the schematic depiction of surface gap states. (b) Plot comparing the degree of band bending to the relative densities of surface and space charge. (a) and (b) adapted from ref[6].

As shown in Figure 1.2a, the Fermi level at the surface is above ϵ_s , so the surface states are filled, and the surface will be negatively charged, leading to the compensating upward band bending, as shown. The band bending leads to the formation of space charge within the bulk of the semiconductor, the density of which is determined by the amount of surface states. At equilibrium, the band bending is just enough to compensate the surface charge. At the surface, the semiconductor work function, Φ_s , then, depends on the degree of band bending according to:

$$\Phi_s = \Phi_C + \Phi_0 + \delta. \quad [1.3]$$

The relationships between the two charge densities (σ_s and σ_i , or the surface and interior charges, respectively), and Φ_0 are shown in Figure 1.2b. For a volumetrically

uniform space charge, σ_i is dependent on the square root of Φ_0 . The trace of σ_s with Φ_0 has a steep slope indicating a high density of surface states. Its zero occurs when

$$\Phi_0 = \varepsilon_s - \delta, \quad [1.4]$$

since ε_s represents the level to which the surface states must be filled to give zero net surface charge. For a very high density of surface states, the trace of σ_s is nearly vertical, thus the zeros of the traces σ_s and $(\sigma_s + \sigma_i)$ coincide. For this case, combining equations 1.3 and 1.4 gives

$$\Phi_s = \Phi_C + \varepsilon_s. \quad [1.5]$$

The Fermi level of the semiconductor does not affect the work function, thus the effective *surface* Fermi level becomes ε_s , which fixes the amount of band bending and consequently, the metal-semiconductor barrier height Φ_B . Figure 1.3 illustrates this effect in terms of a semiconductor band diagram in which the doping is varied from n-type to p-type from one end of the semiconductor to the other. In order for the surface band bending due to surface states to be significant (i.e. for Φ_0 to be on the order of ε_s), Bardeen estimates a density of $\sim 10^{12}$ states/cm², or about one state for every 1000 surface atoms.

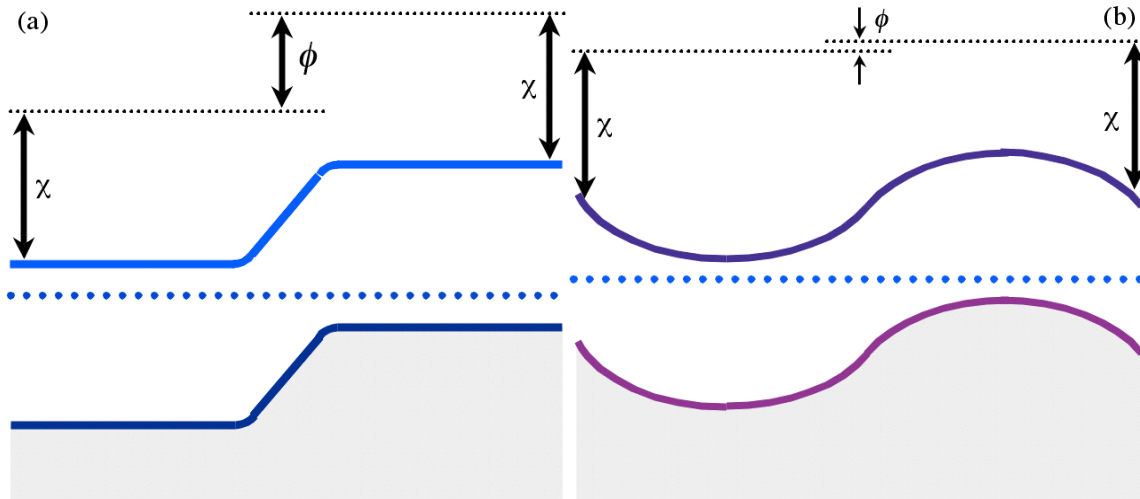


Figure 1.3: Demonstration of the effect surface states may have on semiconductor surfaces, using a *p-n* junction. In (a), no surface states are present and the difference in contact potential (ϕ) for the same metal is large between the *p* and *n*-type sides of the crystal. In (b), a large quantity of surface states exists, and ϕ in this case is much smaller. Adapted from ref[6].

Examining Figure 1.2a, the electric fields formed at the interface can be evaluated, and the amount of surface charge required to completely erase the effect of the bulk semiconductor Fermi level can be estimated. The field between the metal and semiconductor is given by

$$\frac{(\Phi_M - \Phi_S)}{qa} \quad [1.6]$$

The field itself is caused by the charges existing at the semiconductor surface, so can be expressed as the total charge density

$$4\pi(\sigma_s + \sigma_i). \quad [1.7]$$

Equating the two expressions, and substituting Equation 1.3 into 1.6, finally yields

$$\frac{\Phi_M - \delta - \Phi_C - \Phi_0}{4\pi qa} = \sigma_s + \sigma_i, \quad [1.8]$$

where σ_s and σ_i are functions of Φ_0 . Now, Figure 1.2b is revisited in Figure 1.4. The left-hand side of Equation 1.8 is added to the plot, and its solution is the intersection of the new line with $(\sigma_s + \sigma_i)$.

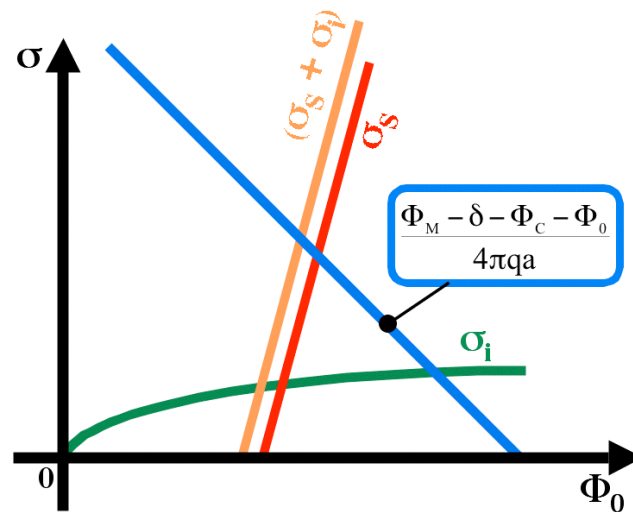


Figure 1.4: Modification of the plot given in Figure 1.2b, with the addition of the first electric field term of Equation 1.8

If the density of surface states is high, then $(\sigma_s + \sigma_i)$ will have a steep slope, and the intersection of Equation 1.8 and $(\sigma_s + \sigma_i)$ will occur at nearly the same value for Φ_0 as given by Equation 1.4. Thus, again the barrier height is practically independent of the Fermi level. In the standard Schottky-Mott picture of metal-semiconductor interface formation, the value of Φ_0 is determined by the difference in work functions between the two phases. The Fermi levels align at equilibrium, and band bending occurs to bring the vacuum levels into registry. According to Bardeen's picture, however, at some value of σ_s , the work function of the metal

would cease to be of importance in determining the barrier height, because the semiconductor already determines the band bending, before the two materials are brought together. For this to take place, the absolute value of the slope of the line σ_s (and consequently $(\sigma_s + \sigma_i)$) must be much larger than that of the line describing the left side of Equation 1.8. This occurs for $\sigma_s > 10^{13} \text{ cm}^{-2}$, or approximately one order of magnitude higher density than is required for appreciable band bending to occur.⁶ In this case, the slope parameter, S , is equal to zero. This is referred to as the Bardeen limit.

Concomitantly to Bardeen's work, Meyerhof published results further supporting the concept of Fermi level pinning by surface states.⁸ Meyerhof measured the Schottky barrier heights of 11 elemental metals and alloys on n- and p-type silicon. No discernible relationship between the metal work function and Φ_B is present, and in fact very little variation in Φ_B exists through the series of metals. Additionally, referring back to Figure 1.3, it can be seen that the work function for a semiconductor doped p-type, should differ from that of the same semiconductor doped n-type by approximately the value of the semiconductor band gap. Meyerhof measured the work functions of n- and p-type silicon, and found a variation of only 0.3 eV. The results are interpreted in the context of a metallic silicon surface, which screens the contact potential of the metals, thus reducing the dependence of the metal work function. This interpretation is similar to Bardeen's surface state approach; in Shockley's seminal paper regarding surface states, he notes that the states should exist as a half-filled band, and would be conductive in the surface plane.⁷

Brattain and Bardeen,⁹ and Morrison¹⁰ first reported experimental studies explicitly setting out to prove the existence of surface states, by changing the surface exposure of Ge crystals and measuring the contact potential,⁹ and the surface conductivity.¹⁰ The results suggested that surface states existed and had significant influence on the properties of semiconductors, but the states probed in these studies would not prove to be those fundamentally important to Schottky barrier formation.

1.1.3 The Development of MIGS Theory

For the next several years, research into metal-semiconductor contacts continued in much the same vein as Meyerhof's contribution: numerous reports of materials systems in which the variation of Φ_B with Φ_M is much smaller than that predicted by the Schottky-Mott rule, with little further progress in the understanding of the proposed surface states and their origins. For metal-Si contacts, Crowell *et al.* measured the barrier heights of evaporated Au, Ag, Cu, and Pd films on Si using the spectral response of the photocurrents.¹¹ Archer and Atalla performed differential capacitance measurements of Cu, Au, and Ni contacts on n-type silicon.¹² Mead and Spitzer reported Φ_B data collected using current-voltage measurements of Au-Si contacts.¹³ In all cases, Φ_B was found to be essentially independent of the metal work function. Crowell, Sze and Spitzer reported in 1964 that the temperature dependence of Φ_B for Au films on n-type Si was identical to the temperature dependence of the Si band gap.¹⁴ The increase in Φ_B is due to the decrease in the Si band gap with temperature. The bulk

Fermi level tends toward the middle of the gap as temperature increases, and thus Φ_B , had it been determined by the Fermi level, would decrease as temperature increases.

During the same period, a similar set of data evolved for several compound semiconductors. See, for example, references[13,15,16] for an overview of work performed on GaAs, InSb, GaP, AlSb, InP, GaSb, InAs, and CdS. For all materials except for CdS, a very weak dependence of Φ_B with Φ_M is observed. In particular, the insensitivity of Si and GaAs suggested that the density of surface states for these materials must be near to the Bardeen limit value of $> 10^{13} \text{ cm}^{-2}$. Notable among this work is the appearance of the “ $E_G/3$ rule,”¹³ the first of several attempts to establish broad trends for predicting interface behavior. This rule was based on the observation that the Fermi level pinning always seemed to occur above the valence band maximum by a value of approximately 1/3 of the band gap. The observation was based on a serendipitously limited data set, and the inclusion of more complete data, along with appropriate account of experimental scatter, disproved the trend.

Concomitantly to much of the work cited above in metal-semiconductor contacts, two major contributions to their understanding were put forward. First, Cowley and Sze finally quantified Bardeen’s predictions, by synthesizing the body of experimental work into a unifying equation for predicting the barrier height at such interfaces.¹⁷ Taking into account the image force barrier height lowering $\Delta\Phi_n$ (the Schottky effect), the slope parameter S , and finally referencing the highest occupied surface state Φ_s to the top of the valence band, rather than the bottom of the conduction band (as in [6]), Cowley and Sze derived the barrier height as given by

$$\Phi_B = S(\Phi_M - \chi_s) + (1 - S)(E_G - \Phi_s) - \Delta\Phi_n. \quad [1.9]$$

By considering the variation in band bending with the density of surface states, S can be derived as

$$S = \frac{1}{1 + \frac{q^2 D_{SS} \delta}{\epsilon_i \epsilon_0}}. \quad [1.10]$$

Here, then, is the first description of the slope parameter explicitly as a function of the density of surface states, D_{SS} . Also included is some accounting for the chemical and electrical quality of the interface, expressed as the interface thickness δ and its dielectric behavior ϵ_i . In considering Equation 1.9, there are two obvious limiting cases: **(1)** as $S \rightarrow 1$, then the density of surface states is small, and the Schottky-Mott rule applies (with the additional image force term), and **(2)** as $S \rightarrow 0$, then the density of surface states is very large, and the Bardeen limit is in effect; the barrier height is controlled by the energy distribution of the gap states. Additionally, differentiation of Equation 1.9 with respect to temperature shows that if the temperature dependence of Φ_M and X are approximately equal, then the change in Φ_B with temperature is equal to the change in band gap with temperature, as observed in.¹⁴ Cowley and Sze compiled much of the experimental data referenced above and applied Equations 1.9 and 1.10 in an attempt to consistently explain the observations. They determined slope parameters for Si, GaP, GaAs, and CdS, finding that in all cases the data, which had previously been fit using the Schottky-Mott approach, was better described when some Fermi level pinning was taken into account.

Also in 1965, Heine argued that the surface states discussed by Bardeen and proven to exist through experimental data are not necessarily the result of the crystal surface being intrinsically different from the bulk (i.e. they do not exist as “dangling bonds”).¹⁸ Instead, the surface states are a result of the bulk states of the metal contact, which tail exponentially into the semiconductor, in the energy range of the band gap. The states into which the metal states decay are derived from the “virtual gap states,”³ which are states in the intrinsic band structure of a semiconductor, which possess complex wave vectors. Such states either grow or decay exponentially, and thus can only exist at interfaces, from which they can decay.¹⁹

Heine’s theory was largely ignored experimentally for many years, but slowly gained traction, as theoreticians explored the concept. Louie and Cohen used pseudopotential calculations to model the electronic structure of Al-Si contacts using a jellium to approximate the Al metal.²⁰ They found four types of interface states: **(1)** states falling in the energy region of the semiconductor valence band and the metal conduction band, **(2)** bulk semiconductor states lying below the metal conduction band which decay into the metal, **(3)** localized interface states lying in energy gaps below the semiconductor valence band, and **(4)** states in the range of energies where the metal conduction band overlaps the semiconductor band gap. In the fourth case, the states result in a continuum of metal-induced gap states (MIGS), which are filled up to the Fermi level.

Louie *et al.* expanded upon the previous work by including calculations for GaAs-, ZnSe-, and ZnS-Al (jellium) interfaces,²¹ and found the same behavior. Further, they calculated the MIGS density of states for the four semiconductors investigated over the

previous two references, and found values in the range of $1-5 \times 10^{14} \text{ cm}^{-2}$, from which they determined the slope parameters. Although this work did not take into account the possibility of interface chemical and structural effects, the calculated S values agreed well with experimental observations, and suggested a trend towards a smaller density of MIGS (and thus smaller degree of Fermi level pinning), as the ionicity of the compound increased.

The ionicity trend presented the tantalizing possibility of a predictive link between an easily obtained quantity (the Pauling ionicity) and the Schottky barrier height, which had proved so elusive to understanding. Kurtin *et al.* first proposed the relation in 1969.²² They collected the known experimental data of the time (23 semiconductors and oxides), and plotted the slope parameters as a function of the Pauling ionicity (or the difference in the electronegativity X between two constituents of a binary compounds). The data is reproduced in Figure 1.5, and shows a pronounced S-shaped trend, with a step in the slope parameter at $\Delta X \sim 0.8$.

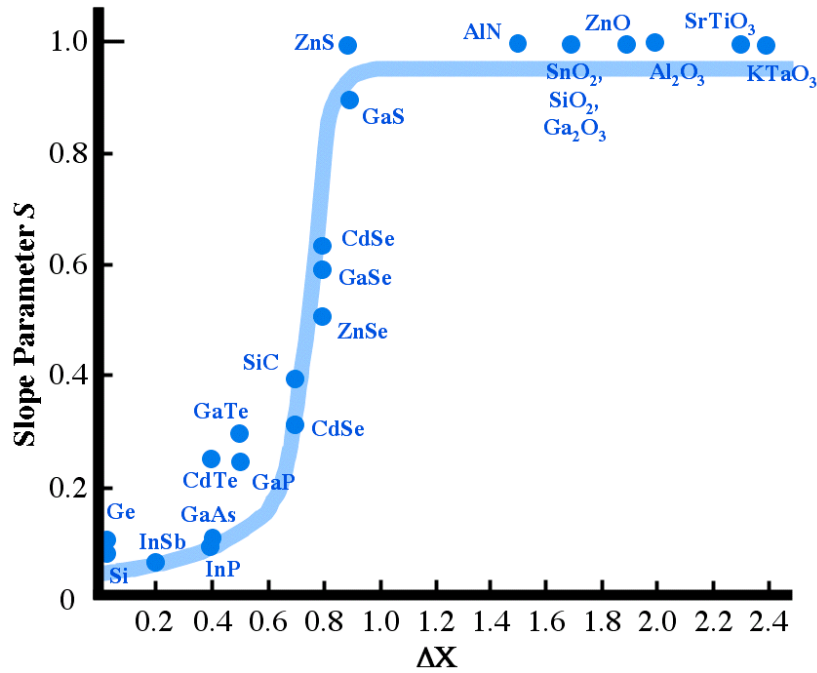


Figure 1.5: Plot from Kurtin, *et al.* showing slope parameter S versus Pauling ionicity ΔX for various dielectric materials. Data reproduced from ref[22].

The authors cite that for highly ionic solids, Madelung potential calculations show that the electrostatic binding energy of a surface atom is nearly identical to that of an atom in the bulk, and thus the surface of an ionic solid is not unique in its electrical properties. This explanation also serves to highlight the early resistance to Heine's MIGS theory, as it ignores the concept of the complex band structure.

Schlüter²³ later pointed out that in considering the slope parameter as a function of electronegativity, the correct definition for S is

$$S_X \equiv \frac{\partial \Phi_B}{\partial X_M}, \quad [1.11]$$

or the change in barrier height with respect to the change in metal electronegativity, rather than the metal work function. Values for S can easily be converted to S_x , since the work function and electronegativity are linearly related, but the Schottky limit for S_x is not unity. Rescaling the slope parameters from Kurtin *et al.*, and accounting for experimental scatter, Schlüter ruled out the S-shaped trend, as shown in Figure 1.6.

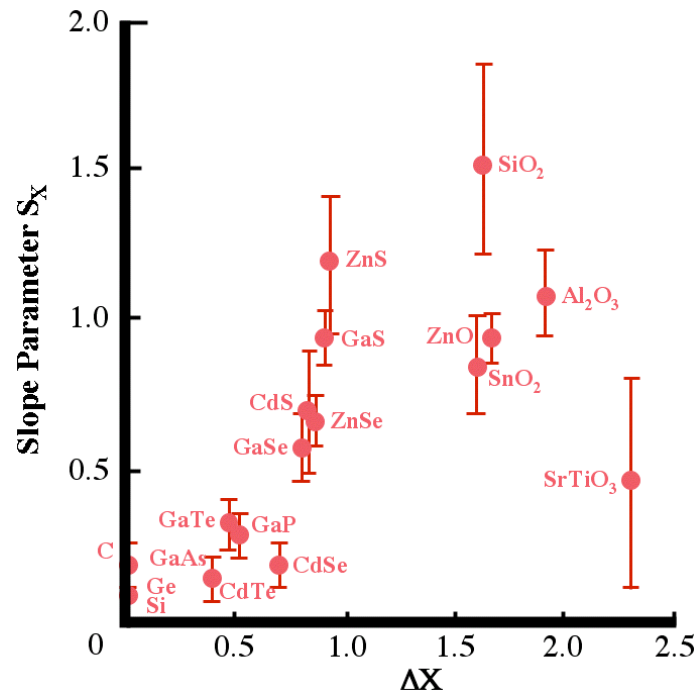


Figure 1.6: Kurtin *et al.*'s data after Schlüter's rescaling of S to S_x . No S-shaped trend is discernible by a least-squares fit. Still, the correlation of S with a fundamental materials parameter seems possible. Reproduced from ref[²³].

The attempt to correlate the slope parameter with electronegativity was not successful, but the drive to connect S to fundamental material properties continued. Phillips²⁴ reasoned that since S describes the screening of the metal work function by a double layer at the semiconductor interface, and that it is semiconductor (not metal) dependent, then it must

still be derived from the bonding of the semiconductor, as Kurtin *et al.* had attempted to show. Phillips' suggestion, which had far-reaching influence, was a correlation based on the electronic polarizability ($\epsilon_\infty - I$) of the semiconductor. Schlüter²⁵ attempted to prove this correspondence by plotting S_X vs ($\epsilon_\infty - I$), but the results were no more definitive than his adjustment of Kurtin *et al.*'s result (Figure 1.6).

Mönch later showed that the product $D_{SS}\delta$ (see Equation 1.10) is related to the average band gap of the semiconductor, which can also be related to the electronic polarizability ($\epsilon_\infty - I$).²⁶ Thus, by rearranging Equation 1.10, it can be seen that to relate S to the polarizability, the correlation should be $(I/S - I)$ vs. ($\epsilon_\infty - I$). These results are shown in Figure 1.7; the data shows a quadratic relation between $(I/S - I)$ and ($\epsilon_\infty - I$), and brings the C (diamond) data point into agreement (diamond presented an interesting case for the test of the two correlations; it is covalent, $\Delta X = 0$, but has a large band gap, and thus small polarizability).

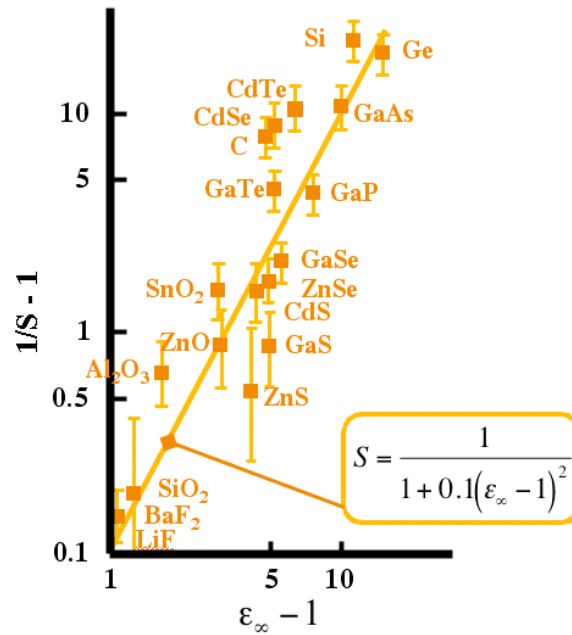


Figure 1.7: Mönch's data showing the quadratic relationship between the slope parameter and the electronic polarizability. The regression coefficient r is 0.91. Note the agreement for diamond; Schlüter had previously attempted a simple S vs. $(\epsilon_{\infty} - 1)$ correlation, but the diamond data fell well outside of any trend. Reproduced from ref^[26].

The slope parameter correlation discovered by Mönch provided strong support for MIGS theory. Mönch went on to show that the decay length of the MIGS is inversely proportional to the average band gap width,²⁷ and thus materials with wide band gaps (and small $(\epsilon_{\infty} - 1)$) should be less affected by Fermi level pinning.

In the meantime, Tersoff^{28,29} and Cardona and Christensen³⁰ had undertaken an effort to calculate the branch point energies, E_B , of semiconductors. Tersoff states²⁹ that the surface Fermi level should correspond with the highest occupied energy of the MIGS, which corresponds to the branch point energy. This is the energy at which the virtual gap states transition from donor- to acceptor-like states. The net charge density in the MIGS, then, is

negative, zero, and then positive when the Fermi level is above, equal to, and below E_B , respectively. For this reason, E_B is frequently called the charge neutrality level (CNL).

Both Tersoff²⁸ and Cardona and Christensen³⁰ show (for Si, Ge, GaP, InP, AlAs, GaAs, InAs, and GaSb) that the determination of the CNL depends only upon accurate knowledge of the *bulk* band structure (as Heine had predicted in 1965), and achieve excellent agreement with experimental data without considering interfacial structure or chemistry. These contributions, along with the correlation of the slope parameter and electronic polarizability, effectively provided the final necessary support for MIGS theory. With additional experimental input, MIGS was eventually accepted to be the fundamental mechanism determining Φ_B for metal-semiconductor contacts.³¹

1.2 Semiconductor Heterostructures

1.2.1 The IFIGS Model

Having reviewed the development of the MIGS model for predicting metal-semiconductor band alignment, the mechanisms determining the band alignment at semiconductor-semiconductor (or more generally, dielectric-dielectric) interfaces will be shown to be simply an extension of the MIGS model. As the technology for growing high-quality semiconductor heterostructures was not developed until well into the metal-semiconductor contacts debate, the relative lack of confusion in the heterostructures literature is striking in comparison. Experimentally, the premier method for determining the band

alignment at such interfaces is photoemission spectroscopy; such measurements will be covered in detail in Chapter Two.

Figure 1.8 shows a band diagram of two semiconductors in contact, neglecting band bending. The electron affinity χ , the ionization energy I , band gap E_G , Fermi level E_F , valence band offset ΔE_V , and the conduction band offset ΔE_C are depicted.

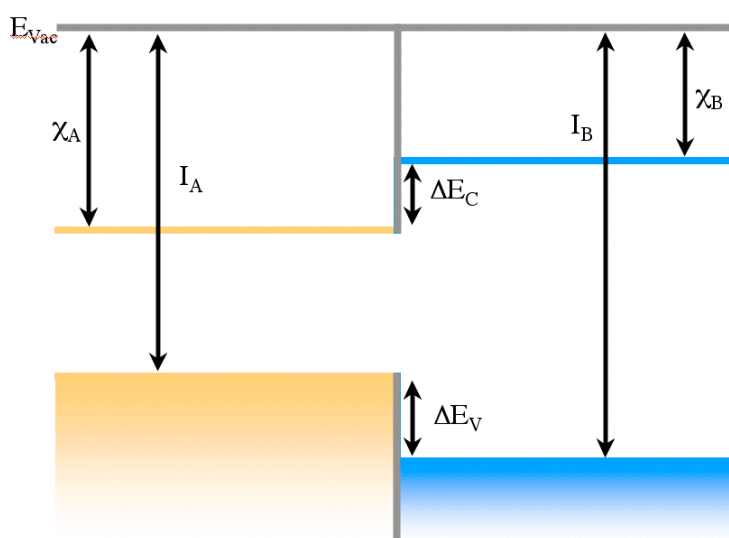


Figure 1.8: Schematic band diagram showing two semiconductors in intimate contact, giving the quantities used in Anderson's first explanation of heterostructures band alignment. For more complex models, the charge neutrality levels of each semiconductor align to establish the band offset and bending.

Anderson studied Ge-GaAs heterostructures and made a first attempt to explain their behavior in terms of band alignment in 1962.³² This study was published three years prior to both Cowley and Sze's quantification of Bardeen's surface state theory,¹⁷ and Heine's prediction of MIGS,¹⁸ and thus the understanding of any semiconductor interface formation was far from complete. Anderson's approach therefore remains within the confines of the

Schottky-Mott rule. Anderson accordingly defines the conduction band offset as resulting from the difference of the two electron affinities:

$$\Delta E_C = \chi_A - \chi_B, \quad [1.12]$$

and the valence band offset is then the difference of the ionization energies:

$$\Delta E_V = I_B - I_A. \quad [1.13]$$

Like the Schottky-Mott rule, Anderson's rule assumes a zero density of surface states, and uses quantities (I and χ) more appropriate to free surfaces than interfaces.³

Harrison attempted to solve the problem by using a linear combination of atomic orbitals (LCAO) approach.³³ He calculated the positions of the valence band maxima of 37 different semiconductors (elemental and compound) with respect to their vacuum levels. To calculate the valence band offset ΔE_V , then, Harrison simply placed the two valence band maxima on a common energy scale and evaluated the difference. The conduction band offset ΔE_C could then be estimated if the two band gaps were known.

Harrison's theory had the advantage of being extremely simple in its use for predicting band offsets and enjoyed reasonably good agreement with experimental results at the time. It makes no predictions, however, on the nature of the interface, specifically the tailing of the states from one semiconductor into the gap of the other. This concept was well established by this time (at least theoretically), and its dominating influence on band alignment was beginning to be understood.

Tejedor and Flores first extended the CNL model to semiconductor heterostructures in 1978.³⁴ In their model, the valence band offset is expressed simply as the difference in branch point energies E_B of the two semiconductors:

$$\Delta E_V = E_{B,A} - E_{B,B} + \Delta, \quad [1.14]$$

where Δ represents an interface dipole term. Δ is essentially an experimental correction factor, which encompasses effects ranging from dipoles resulting from polar interfaces, strain, and the ionicity of the interface bonds (for most semiconductor interfaces, this last effect can be neglected). Tersoff also arrived at Equation 1.14 in 1984,²⁹ and with the collection of CNL's tabulated by Tersoff²⁸ and Cardona and Christensen,³⁰ the basic underpinning of the IFIGS (InterFace Induced Gap States) model was established. The mechanism is analogous to the MIGS concept: filled bulk states from the valence band of one semiconductor tail into the virtual gap states of the other, providing the charge transfer that aligns the CNL's of the semiconductors, and establishing the band offset.

1.2.2 Correlating Experiment and Theory

Because of the technological importance of semiconductor heterostructures, a wealth of experimental data exists which allows the utility of the IFIGS theory to be assessed. For an excellent review of band alignment measurements of elemental/compound semiconductor heterostructures, ternary and quaternary III-V heterostructures, and chalcopyrites, see Chapter Six of ref[3]. As a general rule, agreement between theory and experiment is excellent (within 0.1 eV, or inside the limits of experimental error). The case of the band

alignment between semiconductors and oxide dielectrics is somewhat more ambiguous, as the value of Δ from Equation 1.14 becomes larger due to large lattice mismatches, differences in electronegativity, and polar effects.

The interest in oxide/semiconductor band alignment has ballooned since the need emerged for dielectrics with permittivities higher than that of SiO_2 (~ 3.9). This requirement was driven initially by the increased scaling of Si-based transistors to smaller and smaller dimensions, which necessitated the need for thicker gate dielectrics to mitigate tunneling losses. In this respect, the band alignment at the oxide/Si interface is a chief parameter in determining the behavior of the interface. The significance of compound semiconductors, and the relatively poor quality of their native oxides, has extended this focus to III-V/oxide interfaces.

To date, Robertson^{35,36} has provided the most complete application of the CNL/IFIGS theory to predict the band alignment between Si and a wide range of dielectrics, including ferroelectric oxides. Robertson calculated slope parameters and CNL's for 16 dielectrics of interest using Mönch's empirical relation for S (see Figure 1.7), and Tersoff's method for the CNL. Agreement with experimental data is similar in quality to studies mentioned above in semiconductor/semiconductor heterostructures. Robertson also shows that the band alignment for most transition metal oxides is asymmetric (i.e. a much larger ΔE_V than ΔE_C), because the CNL for the oxides of interest lies relatively high in the band gap. This is because the position of the CNL depends on a weighted average of the density of states; increasing the conduction band density of states can shift the CNL lower in the gap. Since the

conduction band in metal oxides derives from metallic states, this can be accomplished by decreasing the valence of the metal cation, or by using unary, rather than binary, oxides.

Robertson also applied the CNL/IFIGS theory to III-V/oxide interfaces.³⁷ Experimental values, where available, compare less favorably in this case. It should be noted that the calculations of Robertson do not account for chemical or structural effects at the interface, i.e. they do not account for Δ in Equation 1.14. Such effects may have a much larger influence for these materials. For example, some of the poorest agreement is obtained in the case of oxides on GaN, a polar semiconductor. The polarization charge at the [0001] surface of GaN must be compensated; this would surely have some effect on the interface formation, and thus, the band alignment. Robertson's value of ΔE_c for MgO on GaN differs from the value measured in this thesis by $\sim 25\%$. A similar disagreement is found for SiO₂ on GaN, though it should be noted that not all comparisons with experiment are this unfavorable, so it is difficult to quantify the effect of Δ in all cases; indeed, it is likely to be oxide-dependent for a given semiconductor. This highlights the need for extensive experimental studies of such interfaces.

REFERENCES

- ¹ F. Braun, *Annalen der Physik und Chemie* **153**, 556 (1874).
- ² W. Schottky, *Naturwissenschaften* **26**, 843-843 (1938).
- ³ W. Monch, *Electronic properties of semiconductor interfaces* (Springer-Verlag, New York, 2004).
- ⁴ W. Schottky, *Physikalische Zeitschrift* **41**, 570-573 (1940).
- ⁵ N. F. Mott, *Proceedings of the Royal Society of London Series a-Mathematical and Physical Sciences* **171**, 0027-0038 (1939).
- ⁶ J. Bardeen, *Physical Review* **71**, 717-727 (1947).
- ⁷ W. Shockley, *Physical Review* **56**, 317-323 (1939).
- ⁸ W. E. Meyerhof, *Physical Review* **71**, 727-735 (1947).
- ⁹ W. H. Brattain and J. Bardeen, *Bell System Technical Journal* **32**, 1-41 (1953).
- ¹⁰ S. R. Morrison, *Journal of Physical Chemistry* **57**, 860-863 (1953).
- ¹¹ C. R. Crowell, L. E. Howarth, W. G. Spitzer, and E. E. Labate, *Physical Review* **127**, 2006-& (1962).
- ¹² R. J. Archer and M. M. Atalla, *Annals of the New York Academy of Sciences* **101**, 697-& (1963).
- ¹³ C. A. Mead and W. G. Spitzer, *Physical Review Letters* **10**, 471-& (1963).
- ¹⁴ C. R. Crowell, S. M. Sze, and W. G. Spitzer, *Applied Physics Letters* **4**, 91-& (1964).
- ¹⁵ W. G. Spitzer and C. A. Mead, *Journal of Applied Physics* **34**, 3061-& (1963).
- ¹⁶ C. A. Mead and W. G. Spitzer, *Physical Review a-General Physics* **134**, A713-& (1964).
- ¹⁷ A. M. Cowley and S. M. Sze, *Journal of Applied Physics* **36**, 3212-& (1965).
- ¹⁸ V. Heine, *Physical Review* **138**, 1689-& (1965).

- 19 W. Monch, Surface Science **300**, 928-944 (1994).
- 20 S. G. Louie and M. L. Cohen, Physical Review B **13**, 2461-2469 (1976).
- 21 S. G. Louie, J. R. Chelikowsky, and M. L. Cohen, Physical Review B **15**, 2154-2162 (1977).
- 22 S. Kurtin, T. C. McGill, and C. A. Mead, Physical Review Letters **22**, 1433-& (1969).
- 23 M. Schluter, Physical Review B **17**, 5044-5047 (1978).
- 24 J. C. Phillips, Journal of Vacuum Science & Technology **11**, 947-950 (1974).
- 25 M. Schluter, Thin Solid Films **93**, 3-19 (1982).
- 26 W. Monch, Physical Review Letters **58**, 1260-1263 (1987).
- 27 W. Monch, Applied Surface Science **92**, 367-371 (1996).
- 28 J. Tersoff, Surface Science **168**, 275-284 (1986).
- 29 J. Tersoff, Physical Review Letters **52**, 465-468 (1984).
- 30 M. Cardona and N. E. Christensen, Physical Review B **35**, 6182-6194 (1987).
- 31 W. Monch, Journal of Vacuum Science & Technology B **17**, 1867-1876 (1999).
- 32 R. L. Anderson, Solid-State Electronics **5**, 341-& (1962).
- 33 W. A. Harrison, Journal of Vacuum Science & Technology **14**, 1016-1021 (1977).
- 34 C. Tejedor and F. Flores, Journal of Physics C-Solid State Physics **11**, L19-L23 (1978).
- 35 J. Robertson, Integrated Ferroelectrics **32**, 943-950 (2001).
- 36 J. Robertson and C. W. Chen, Applied Physics Letters **74**, 1168-1170 (1999).
- 37 J. Robertson and B. Falabretti, Journal of Applied Physics **100**, - (2006).

2. X-ray Photoelectron Spectroscopy

X-ray photoelectron spectroscopy (XPS) is the principle analysis technique used in the experimental work presented in this thesis; all of the experiments were designed around its use, and the conclusions drawn derive chiefly from spectroscopic data. This chapter is divided into three sections. The first section is concerned with the history of XPS, dating from the late 19th century. This section highlights the development of the technique from the standpoint of the early investigators' struggles with technological limitations despite an evident appreciation for the possibilities offered by the method, through the development of adequate instrumentation that enabled those possibilities to be quickly realized.

The second section of the chapter is a brief discussion of the fundamentals of XPS, from basic aspects of theory to practical features of the instrumentation. The theory section focuses on the fundamental equation describing XPS experiments and its consequences, the origin of the "surface sensitive" label for the technique, and the mechanism leading to the observation of chemical shifts in photoelectron spectroscopy. The section on instrumentation highlights the two most important components of a surface analysis system: the x-ray source and the spectrometer.

Finally, the third section of this chapter discusses the three analysis techniques employed in this thesis: surface composition analysis, thin film growth mode determination, and band offset measurements.

2.1 Historical Development

2.1.1 Early Experiments

The history of XPS stretches back to the discovery by Hertz, in 1887, of the photoelectric effect.¹ He found that an electric arc between two electrodes of a certain metal could be triggered by the ultraviolet radiation given off by a second arc; it was later shown that the arc was triggered by photoelectrons ejected from the cathode by the UV radiation. Einstein was able to explain this behavior in 1905 with his seminal paper on the quantum nature of light.²

Arguably the first true photoelectron spectroscopy experiment was performed at Princeton in 1912. Richardson and Compton reported an experiment using monochromatic UV light from a mercury lamp to irradiate strips of eight elemental metals.³ The spectrometer used was a spherical conductor with an unspecified energy resolution; however, the spectra collected consisted only of nearly Gaussian electron distributions centered about a maximum kinetic energy, which would have corresponded to the metal work function. No mention is made of any fine spectral features. This resolution limitation would persist for decades.

Several investigators originating from Ernest Rutherford's laboratory at Manchester, England, primarily H. Robinson, took up most of the early development of XPS. Robinson's apparatus consisted of a Cu K α x-ray source aimed at the sample, or "target." The ejected photoelectrons were deflected by a magnetic field onto photographic plates, which enabled the radius of their trajectory, and hence their energy, to be determined. Although several small studies from Rutherford's laboratory had been published earlier, the most complete

early XPS experiment was published in 1923.⁴ Despite the poor instrumental resolution, in studying 19 samples, Robinson was able to locate several photoelectric lines for each material, as well as visually estimate their intensities, even though given the state of quantum mechanics at the time, no explanation of them could be possible. Combined with the second extensive tabulation of spectroscopic data by Robinson (carried out under “exasperating conditions”),⁵ as well as the first definitive observation by M. DeBroglie of Auger electrons in a photoemission experiment,⁶ an impressive and significant contribution to the field of photoelectron spectroscopy was provided much earlier than often realized.

Perhaps the most remarkable of the early work, however, is the report by Robinson and Young of their observation of chemical shifts in the K levels of Cr compounds.⁵ They note a decrease in the kinetic energy of the photoelectric lines between Cr metal and Cr(OH)₃, as well as in the Cr Auger series (“fluorescent lines”). This represents the first clear report of chemical state identification by XPS, and also hints at the use of the Auger parameter in future spectroscopic studies.

The final early contribution of significance came in 1937, when M. Ference reported an accurate measurement of the KLL and KLM Auger series using Ag radiation.⁷ Following this, Robinson and others published sporadic results through the 1940’s, but were constantly plagued by poor instrumental resolution, which prevented the technique from developing any further; it would not be until Siegbahn’s advancements that interest in XPS would be revived. For a far more complete and in-depth review of the early history of XPS, see ref[8].

2.1.2 Modern XPS

Following the extensive work of Robinson and others, interest in XPS as an experimental technique waned; the poor resolution negated any possible advantage it could have over x-ray absorption experiments. However, starting in 1950, K. Siegbahn of Uppsala University began developing a new spectrometer based on his earlier work in nuclear physics.⁸ Siegbahn's essential contribution was adapting a double-focusing magnetic spectrometer for β -ray spectroscopy to be used as a photoelectron analyzer.^{9,10} This provided a two order of magnitude improvement in energy resolution, in addition to improving the signal intensity.

The early experiments by Siegbahn¹⁰ focused on Cu films using Mo $K\alpha$ (17,479 eV) radiation. Using radiation of this energy, the authors were able to investigate deep core levels in Cu (down to the 1s photoelectron line), but the radiation had a broad natural line width and an intense $K\alpha_2$ component, which limited the results somewhat. The authors claim a possible error in their line position measurements of 1.7 eV, providing the various errors combine in a linear fashion. Later, in 1965, Siegbahn and his group began using Cr $K\alpha$ radiation, with significantly lower energy (5417 eV) and line width.¹¹ The change in radiation allowed them to accurately correct earlier values of binding energies for several light elements (Al, Mg, and O). Additionally, although following the first description by Robinson of chemical shifts by nearly 40 years, Siegbahn's report¹² of chemical state identification in Cu and CuO is the first account of such data using the vastly improved technology of the day.

In the 1960's, and especially the 1970's, the worldwide use of XPS increased quickly, and investigators rapidly found a number of ways to employ the technique. In this time period, a wide range of organic molecules was characterized.¹³⁻¹⁶ The results were compared to electronic structure calculations, and in particular, the investigations of organic molecules highlighted the usefulness of the chemical shift observed in XPS, as many organic compounds contain atoms of the same element in different bonding arrangements. Siegbahn's group in particular was active in the XPS study of gases and liquids. They investigated methane and ethane gases,¹⁵ vapors of Bi and Pb,¹⁷ and Hg.¹⁸ The interest in vapors was driven by the desire to correlate cohesive energies of metals with the binding energy differences observed between solids and vapors, and the observations of metal spectra without the inherent features from a solid sample, such as shakeup lines, and plasmon loss peaks. Similar interests, especially in the case of ionic solutions, motivated the study of liquids where studies of the solid were complicated by long-range Madelung potentials.^{19,20} Metal alloys and compounds, being Siegbahn's first conception of the utility of XPS,²¹ also received considerable attention. For example, Shimodaira's group at Tohoku University performed extensive studies of Fe and Cr alloys,^{22,23} studying surface composition and passivation. Studies of Ni were instrumental in providing explanations for final state effects,²⁴ and surface termination effects on valence band regions.²⁵

2.2 Fundamentals of XPS

2.2.1 Practical Aspects of Theory

Photoemission results from the irradiation of an atom with photons of sufficient energy to eject electrons from its core levels (and valence band levels if the atom is part of a solid). For core levels, electrons are confined by binding energies ranging from ~ 10 to $>10^3$ eV, so in general, x-ray radiation is used for such experiments. The kinetic energies of the electrons emitted, then, is the difference between the energy of the incoming radiation, the electron binding energy, and the work function. When collected by an electron energy analyzer (to be described in 2.2.2), the kinetic energies can be determined, and providing the x-ray energy is known accurately, the binding energies (E_B) can be determined according to the following equation:

$$E_B = h\nu - E_K - \Phi_{SP}, \quad [2.1]$$

where $h\nu$ is the x-ray energy, E_K the measured electron kinetic energy, and Φ_{SP} the spectrometer work function. A schematic demonstrating the origin of Equation 2.1 is shown in Figure 2.1.

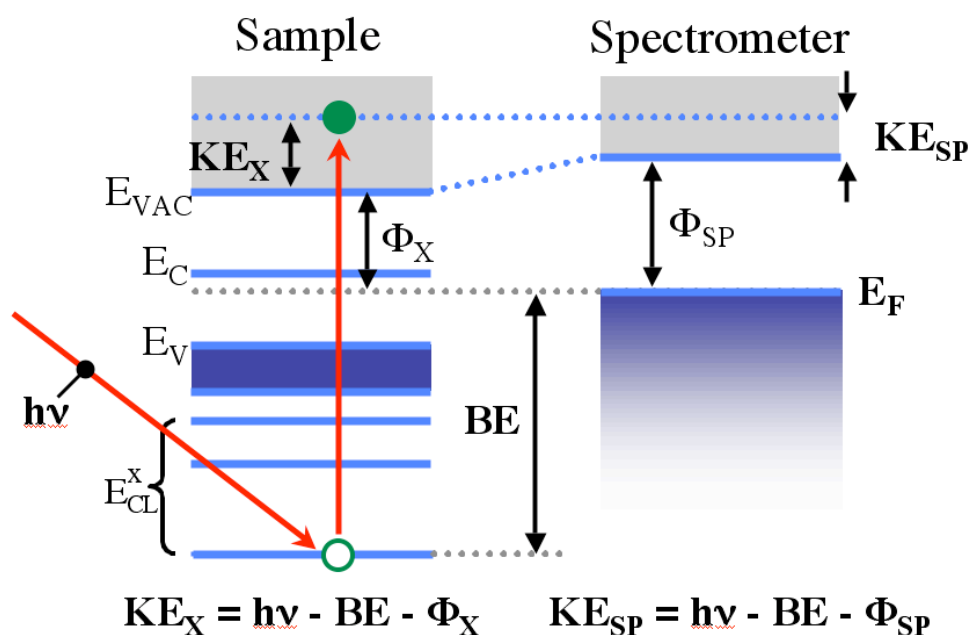


Figure 2.1: Schematic energy level diagram showing the core levels and valence band of a semiconducting sample in equilibrium with the spectrometer. The equivalence of the sample Fermi level and the spectrometer Fermi level allows the experiment to be performed without knowledge of the sample work function.

The substitution of the spectrometer work function with the sample work function is due to the assumption that the sample and the spectrometer are in equilibrium (as seen in Figure 2.1, the Fermi level of the sample and of the spectrometer coincide). This assumption is vital, as it allows practitioners to establish the position of the Fermi level of any sample under investigation (relative to that of the spectrometer). The spectrometer work function is not the energy an electron must gain to escape the spectrometer (the classical sense of a work function), rather, it is a catch-all instrumental term that encompasses all of the processes within the collection equipment that occur to thermalize the collected electrons. Referring to Figure 2.1, where the Fermi levels are depicted as equal, the sum of the kinetic energy at the

spectrometer and the spectrometer work function, is equal to the sum of the kinetic energy at the sample and the sample work function. Provided Φ_{sp} is known (this is determined through instrumental calibration), it is therefore not necessary to know the work function of the sample under investigation in XPS.

Any spectroscopic technique based on the detection of photoelectrons is surface sensitive by default. The inelastic mean free path (IMFP) of escaping photoelectrons determines the surface sensitivity. In XPS, the photoelectrons have kinetic energies up to approximately 1000 eV. The IMFP is controlled mainly by electron-electron interactions, which is described by the dielectric loss function,²⁶ but the dependency of the IMFP on kinetic energy shows a broad minimum in the range of energies accessible by XPS. As shown in Figure 2.2, the IMFP is on the order of 1-10 monolayers for a broad range of energies.

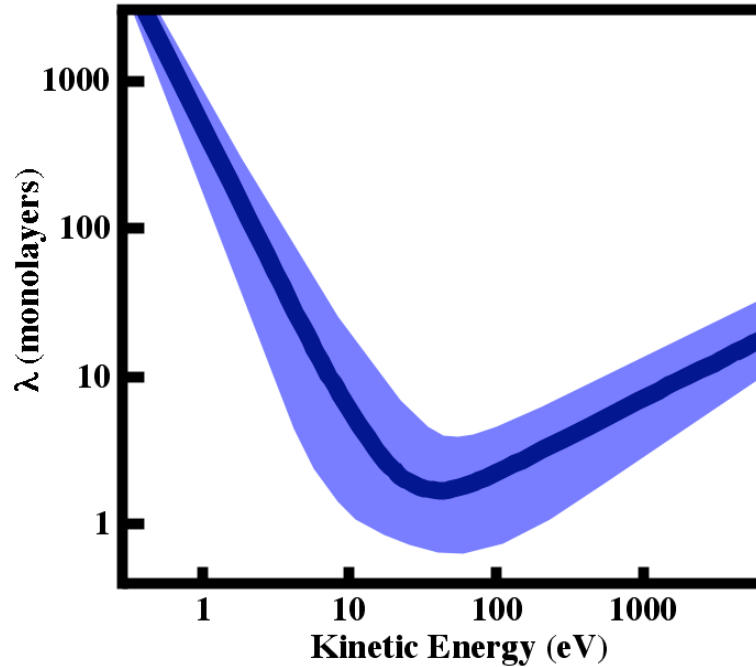


Figure 2.2: Plot of the electron inelastic mean free path for electrons of kinetic energies up to >1000 eV. The heavy line is an empirical fit to the data; the lighter region encompasses the approximate range of values observed for elemental metals. Adapted from ref[27].

Since the IMFP is determined through the dielectric loss function, it should in principle be material-specific. However, one can see from Figure 2.2 that there is actually a fairly narrow band of IMFP's for a given energy, and thus the heavy curve can be considered more or less universal. The lack of a dramatic material dependency stems from the fact that in the energy range of interest, the specific bonding properties of the material are not important, and the average electron-electron distance describes the loss function. This distance is effectively the same for all materials, thus the energy dependence of the IMFP is similar.²⁶ Empirically, the IMFP can be determined, for elements, by the relation

$$\lambda = 538KE^{-2} + 0.41\sqrt{a \cdot KE}, \quad [2.2a]$$

where λ is the IMFP (in units of monolayers), KE is the kinetic energy of the photoelectrons, and a is the monolayer thickness, in nm.²⁸ For inorganic compounds, the relation is slightly different:

$$\lambda = 2170KE^{-2} + 0.72\sqrt{a \cdot KE} . \quad [2.2b]$$

Equations 2.2a and 2.2b are useful for obtaining rough estimates for IMFP's. Since, in many experiments, it is useful to know an approximate degree of surface sensitivity, the sampling depth (the depth less than which 95% of all photoelectrons which have not lost energy originate) is taken by convention to be 3λ .²⁸ It is also often useful in general practice to possess an estimate of how surface sensitivity varies across the entire range of kinetic energies available in an XPS experiment. From Equation 2.2b, one can see that for a monolayer thickness of 0.3 nm, the sampling depth varies from ~1 nm at a kinetic energy of 50 eV, to 13.5 nm at a kinetic energy of 1500 eV. This encompasses the approximate range of energies available when using an Al Ka x-ray source, and demonstrates that the technique is considerably less surface sensitive in the high kinetic energy (or low binding energy) valence band region of spectra.

The unique electronic structure of every element allows for unambiguous elemental identification of effectively any sample (allowing for potential spectral artifacts and overlap). However, XPS is seldom used as simply an elemental technique, because the core level spectra contain sufficient information to identify chemical states. Although the core levels are, by definition, not involved in chemical bonding, they contain chemical information by virtue of the fact that bonding necessarily entails a change in the electronic structure of the

valence levels. Though this change in the valence region can be observed directly via photoelectron spectroscopy of these states, quantitative analysis is difficult as the band structures are generally complex.

The chemical shift effect of the core level photoelectrons is due to the rearrangement of the valence shell. As a photoelectron escapes the atom, it encounters a potential based on the charge distribution in the valence levels. A change in this charge distribution (brought about by a change in chemical state) thus affects the potential encountered by the escaping photoelectron, and its kinetic energy is increased or decreased accordingly. Figure 2.3 demonstrates a simple example of this effect: the difference between a metal and its oxide.

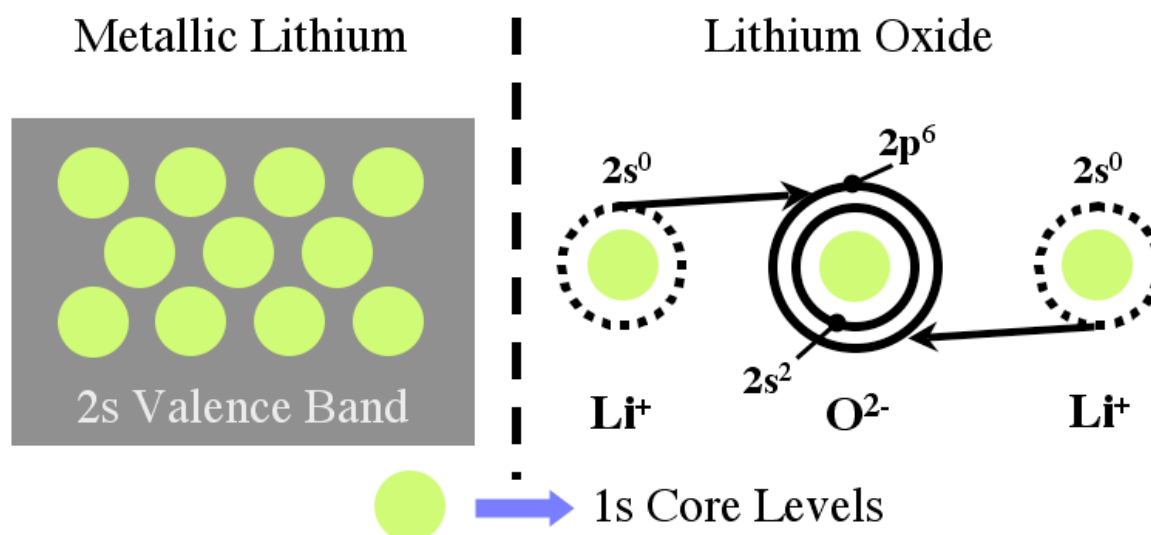


Figure 2.3: Model demonstrating the origin of the XPS chemical shift in terms of the change in valence band electron density upon oxidation of metallic lithium. In the metallic state the atom cores (including the 1s electron levels) are surrounded by a 2s valence band density. Upon oxidation, the 2s valence electrons are taken up by the oxygen 2p level to create a full octet. This decrease in valence band density surrounding the lithium ions reduces the screening of the nuclear charge observed by the escaping photoelectrons, thus the binding energy of the lithium 1s core level increases. For less ionic bonds, the effect is not as pronounced. Adapted from ref[26].

As Figure 2.3 shows, the decrease in valence band electron density experienced by Li atoms upon oxidation leads to the emerging photoelectrons encountering a potential that is positive with respect to the metallic state. This serves to decrease the kinetic energy of the photoelectrons, thus increasing the observed binding energy. The increase in binding energy of a metal photoelectric line is one of the ubiquitous observations of chemical shifts in XPS practice. In general, the binding energy of a photoelectron line is the negative of the corresponding orbital energy, with the addition of some relaxation energy that accounts for

the rearrangement of the electrons within the atom and surrounding atoms after photoemission.²⁸ To a first approximation, then, the chemical shift can be considered as the change in orbital energy that occurs due to chemical bonding. The shift in binding energy can also be approximated by the free energy of the corresponding chemical reaction, this correlates well with observed chemical shift values, showing agreement within ~ 0.5 eV.²⁶

2.2.2 Instrumentation

A standard XPS arrangement includes a radiation source, some mechanism for sample manipulation, and a spectrometer, all contained within an ultra-high vacuum (UHV) chamber. A typical analysis system is shown schematically in Figure 2.4. This section will focus on a brief discussion of relevant practical issues regarding the source and spectrometer (the sample manipulation is of logistical interest only, unless angle-resolved studies are necessary). Additional equipment can include crystal monochromators for the x-ray source, an ultraviolet radiation source (typically in the form of a He glow discharge lamp and its accompanying differential pumping mechanism), an Ar ion beam source for sputter depth profiling, and a low energy electron flood gun for neutralization of charging effects.

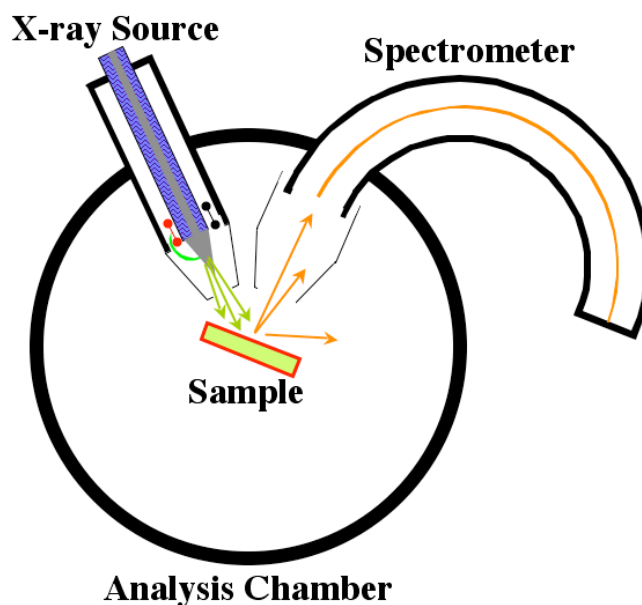


Figure 2.4: Greatly simplified diagram of an XPS analysis chamber. For clarity the sample transfer, pumping, and pressure measurement equipment are omitted.

The desire for UHV conditions in a chamber used for XPS experiments is straightforward. XPS, being a surface sensitive technique, depends a system's ability to maintain a surface in a given state (free of unwanted physisorbed or chemisorbed gases, within the limits of detection) for a sufficient time to carry out the desired experiment. Using a simple gas kinetics argument, the impingement rate for gas molecules on a surface as a function of pressure, in Torr,²⁹ is given by

$$\Phi = 3.51 \times 10^{22} \frac{P}{\sqrt{MT}}, \quad [2.3]$$

where M is the molecular weight of a gas species of interest, T is the absolute temperature, and Φ is in units of atoms (or molecules) per $\text{cm}^2 \cdot \text{s}$. Thus, at a pressure of $\sim 3 \times 10^{-6}$ Torr, a

surface receives approximately one monolayer of gas molecules in one second. This is a conservative estimate based on a sticking coefficient of unity, at room temperature. If it is desired to maintain a clean surface for ~30 minutes, or a typical duration for data collection in XPS, the pressure must be kept to a level at or below $\sim 1 \times 10^{-9}$ Torr. This is well within the capabilities of a standard UHV system. The collection of electrons at the spectrometer also requires a long mean free path, and thus a low pressure. In practice, however, at the pressures necessary for surface cleanliness, the mean free path requirement is satisfied by several orders of magnitude.

The choice of x-ray sources boils down to two factors: the natural line width, and the energy of the radiation. If no crystal monochromators are employed, the line width of the source must be sufficiently narrow so as not to limit resolution in typical XPS experiments. For characterizing most photoelectron lines and chemical shifts, an energy resolution of ~ 1.0 eV is sufficient. The energy of the excitation should be sufficiently high so that a reasonable range of electron core levels can be investigated for all elements. Table 2.1 presents a tabulation, reproduced from ref.³⁰ of common x-ray sources, their energies, and line widths.

Table 2.1: Characteristics of common x-ray sources³⁰

X-ray Line	Energy (eV)	FWHM (eV)
Y M ζ	132.3	0.47
Zr M ζ	151.4	0.77
Nb M ζ	171.4	1.21
Mo M ζ	192.3	1.53
Ti L α	395.3	3.0
Cr L α	572.8	3.0
Ni L α	851.5	2.5
Cu L α	929.7	3.8
Mg Kα	1253.6	0.7
Al Kα	1486.6	0.85
Si K α	1739.5	1.0
Y L α	1922.6	1.5
Zr L α	2042.4	1.7
Ti K α	4510.0	2.0
Cr K α	5417.0	2.1
Cu K α	8048.0	2.6

As shown in bold in Table 2.1, the Mg and Al K α lines have suitable energies and widths for most XPS experiments. For maximum flexibility, the most common arrangement is a dual anode Mg/Al x-ray source. Such a source is shown schematically in cross section in Figure 2.5. The two anodes are deposited as thin films on opposing faces of an angled, water-cooled Cu block. The filament for each respective anode is resistively heated at low voltage, and the resulting thermionic electrons are deflected by focusing elements onto the anode, which is biased at an accelerating voltage of up to +15 kV. The x-ray radiation results from core level ionizations in the target material, and emerges from the source through a thin Al window, which is in place to filter any radiation from possible source contamination, as well as shield the sample from stray electrons.

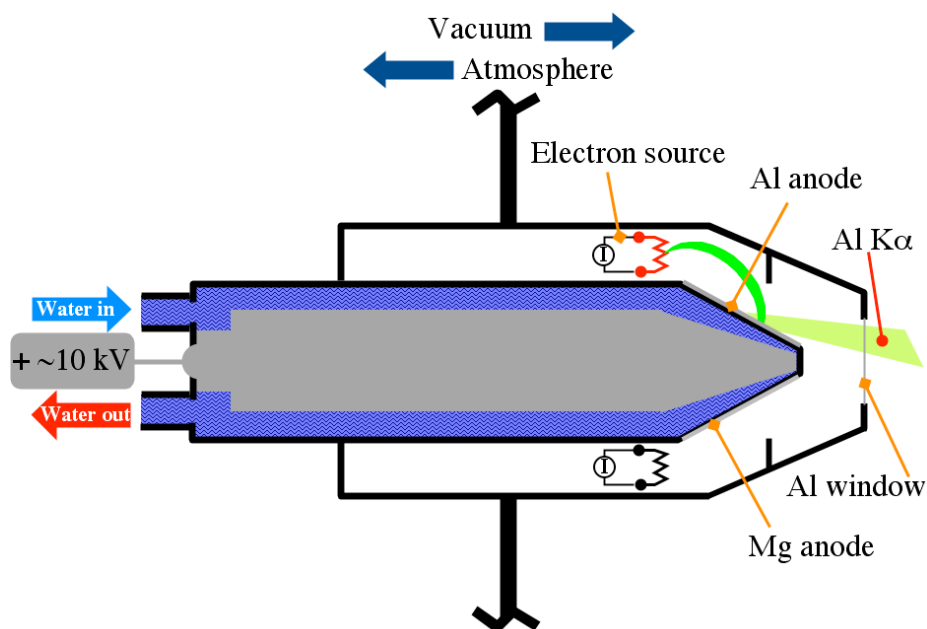


Figure 2.5: Diagram of a typical XPS x-ray source, showing the usual dual-anode arrangement with the aluminum anode in operation. For simplicity, the source is depicted as being rigidly mounted to the vacuum chamber. In practice, the source is typically mounted to a bellows so that it may be moved out of the way during sample transfer.

The most critical component of an XPS analysis system is the spectrometer. The spectrometer passes electrons of an arbitrary kinetic energy of interest to the detector, and rejects electrons of all other energies. The concentric hemispherical analyzer is the most commonly used design for XPS experiments,³⁰ and is shown schematically in Figure 2.6.

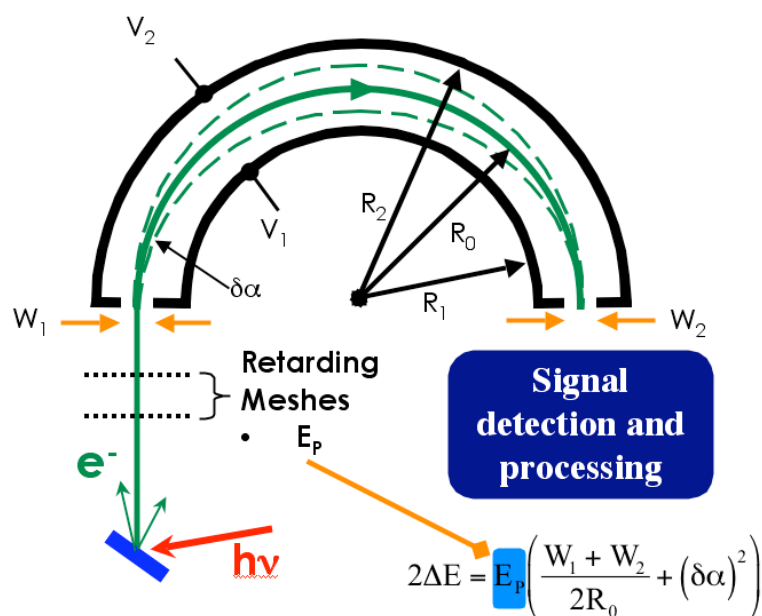


Figure 2.6: Schematic showing the operating principles of the concentric hemispherical analyzer. The escaping photoelectrons (and Auger electrons) are slowed by the retarding meshes; only those electrons slowed to the pass energy are collected at the far end of the spectrometer. The equation is included to show the direct effect the pass energy has on the spectrometer's energy resolution.

Ultimately, the defining characteristic of a spectrometer is the absolute energy resolution, which is defined³⁰ as the full width at half maximum (FWHM) ΔE of a given peak. The relative resolution, R , is defined as:

$$R = \frac{\Delta E}{E_0}, \quad [2.4]$$

where E_0 is the kinetic energy of the photoelectron line in question. In XPS, desire for chemical state analysis demands high absolute resolution over a wide range of kinetic energies. The resolving power of a concentric hemispherical analyzer is inversely related to

the radius of the analyzer and the energy of interest (i.e. narrow features are resolvable for a larger analyzer and for smaller kinetic energies), according to equation 2.4:

$$\frac{2\Delta E}{E_0} = \frac{W}{R_0} + (\delta\alpha)^2. \quad [2.5]$$

Therefore, for sufficient energy resolution over all kinetic energies of interest, the spectrometer would have to be prohibitively large. The solution is the use of retarding electric fields for electrons entering the analyzer, which decrease the kinetic energy of the electrons to a fixed value, called the pass energy E_p . The retarding field can be varied such that all kinetic energies can be selected serially. Thus, the spectrometer plates operate at a fixed potential, set to allow electrons with kinetic energies equal to the pass energy through to be detected (E_0 becomes E_p in Equation 2.4). This not only allows the spectrometer to operate at high resolution when investigating high kinetic energy electrons (e.g. valence band electrons), but also has the effect of making the resolution over the entire range of energies constant.

2.3 Techniques of Interest

In this thesis, three spectroscopic techniques constitute the bulk of the experimental work. Those techniques are: the use of XPS to determine surface molar ratios (or the measurement of surface stoichiometry), growth mode determination of thin films, and the measurement of valence band offsets at semiconductor interfaces. The following section will address practical aspects of these techniques.

2.3.1 Surface Composition Measurements

In XPS, each element has a specific sensitivity to x-ray-stimulated photoemission. Rigorously, the current of photoelectrons escaping a surface is a function of many parameters, including the x-ray flux, the photoelectric cross section for the given orbital, geometric effects based on both the instrumentation and orbital geometry, and the IMFP. These parameters have been empirically distilled into a single factor S , the atomic sensitivity factor for a given orbital, for each element detectable by XPS ($Z \geq 3$). Values for S for each element have been tabulated in [31].

The atomic sensitivity factors allow one to normalize the integrated intensity of photoelectron lines originating from different elements within the same sample. Thus, the peak areas may be placed on a common scale and directly compared. The molar ratio of the surface under investigation can be determined as:

$$X_N = \frac{\frac{I_N}{S_N}}{\sum_j \frac{I_j}{S_j}}, \quad [2.6]$$

where I is the integrated intensity of the peak in question, N is the chemical species of interest, and the summation in the denominator represents the total intensity of the different chemical species desired for comparison. Alternatively, a chemical formula can be obtained by simply referencing all previously normalized peak areas to a peak of choice, thus quantitatively comparing the intensities to one peak. In either case, the analysis is simple, however the surface sensitivity of XPS should not be forgotten. In general, whether through

contaminants such as adventitious carbon or oxygen, or surface chemical reactions, the molar ratios or stoichiometries will differ from those in the bulk, often significantly. Despite these caveats, surface stoichiometries are almost always reported in XPS studies, because they are easily determined and are of general interest.

2.3.2 Thin Film Growth Modes

There are three general mechanisms describing thin film nucleation and growth. In Frank-van der Merwe growth (or 2-D layer by layer growth), the evolution of the film is described by the condensation of the adsorbing atoms into complete monolayers in a smooth growth front. In Volmer-Weber (or 3-D island growth), the adatoms condense on the substrate surface and form individual nuclei that grow and eventually coalesce. Finally, in the Stranski-Krastanov mode, the initial stages of growth follow the Frank-van der Merwe mode for the first few monolayers, after which islands nucleate. The three growth modes are shown in Figure 2.7.

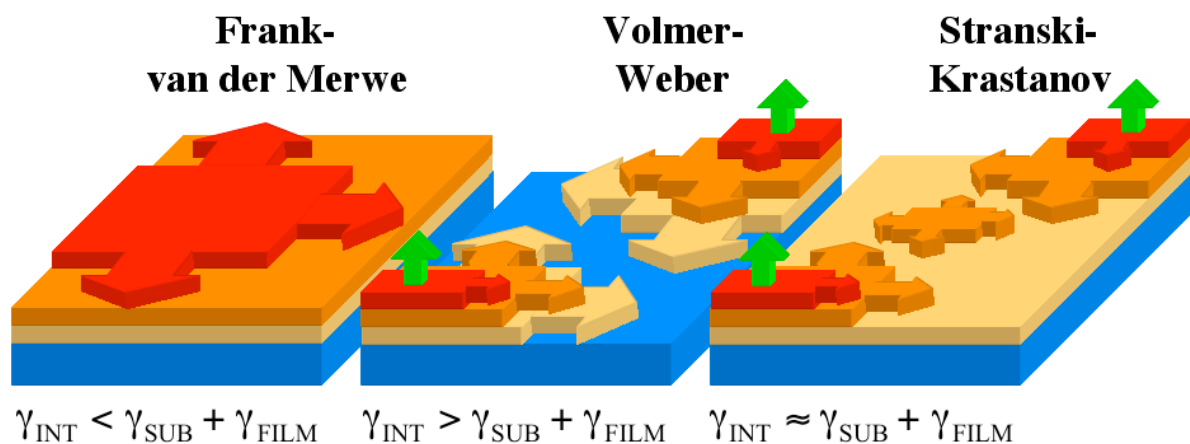


Figure 2.7: The three essential thin film growth modes. In each schematic, three monolayers have been deposited to varying stages of completion. The growth mode is globally dictated by the energy balances depicted under each schematic between the film-substrate interfacial energy, the energy of the substrate free surface, and the energy of the film free surface. In a broad sense, the presence of a Frank-van der Merwe suggests a strong film-substrate interaction, while the Volmer-Weber mode suggests a weak interaction. The Stranski-Krastanov mode is an intermediate case in which the film-substrate interaction decreases rapidly in strength as the film grows, as a result of strain energy or other factors.

Frank-van der Merwe growth typically occurs in systems that are chemically similar or in which the growth atoms otherwise have a strong affinity for the substrate.³² The strong adatom-substrate binding encourages the formation of complete monolayers rather than the segregation into island clusters, and if the substrate-adatom interaction decreases monotonically as the number of layers increases, then layer by layer growth continues. Otherwise, the adatoms may segregate into islands, initiating Stranski-Krastanov growth. The opposite case is true for Volmer-Weber growth, which tends to occur in cases where there is

a weak interaction between the substrate and adatoms, which instead segregate into nuclei, which become stable and grow if they reach a critical size.³³

XPS is a technique well suited to studying growth modes, because the attenuation of photoelectron intensity by an overlayer is dependent on the morphology of that overlayer. Thus, by tracking the intensity of a well-defined photoelectron peak originating from the substrate, as film growth proceeds, the data can be fit to one of several decay functions, which uniquely describe each growth mode. For Frank-van der Merwe growth, the film grows as a dense overlayer, and the photoelectrons originating from the substrate attenuate as

$$\frac{I_s}{I_o} = \exp\left(-t/\lambda\right), \quad [2.7]$$

where I_s is the attenuated photoelectron intensity, I_o the initial intensity (prior to growth), t is the film thickness and λ is the IMFP as determined from Equation 2.2. The measurement is sensitive to partial monolayers, and since exponential decay only occurs for full monolayer coverage, the quantity na can be substituted for t , where a is the thickness of one monolayer and n is the number of complete monolayers. Additional accounting can be made for attenuation due to partial monolayers, but this only necessary at small thicknesses and if very precise control over the deposition is possible.

For the Volmer-Weber (3-D) growth mode, the attenuation of the photoelectrons is still an exponential function, but it is mitigated by the rate of coalescence of the film islands. For this type of growth, the area fraction of the islands' coverage over the substrate is expressed as Θ : as Θ increases from zero, the area fraction increases, and at $\Theta = 1$, the film has coalesced. Volmer-Weber growth attenuates the substrate photoelectron intensity as:

$$\frac{I_s}{I_o} = (1 - \Theta) + \Theta \exp\left(-t/\lambda\right). \quad [2.8]$$

In this case, the first term represents the intensity due to exposed areas of the substrate, and the second term represents the exponential decay due to the film growth.

The Stranski-Krastanov growth mode represents an intermediate case between the previous two modes, and the form of the electron attenuation in this mode is therefore intermediate to the other two modes:

$$\frac{I_s}{I_o} = (1 - \Theta) \exp\left(-na/\lambda\right) + \Theta \exp\left(-t/\lambda\right). \quad [2.9]$$

Here, the attenuation due to the initial 2-D monolayer(s) formed is exponential but damped by the $(1 - \Theta)$ term, and is added to the attenuation due to the 3-D islands (the second term of Equation 2.8). Depending on how quickly Θ increases as deposition proceeds, Equations 2.7 and 2.8 can lead to attenuation very close to that of the Frank-van der Merwe case (if Θ increases rapidly), or to attenuation that is much slower (if Θ increases slowly). For example, in examining Equation 2.7, one can see that if Θ increases very slowly (i.e. it does not approach unity until t is much larger than λ), then the attenuation will be effectively linear with respect to thickness. Figure 2.8 depicts the relative rates of decay for the three growth modes, and at two rates of coalescence for the Volmer-Weber and Stranski-Krastanov modes.

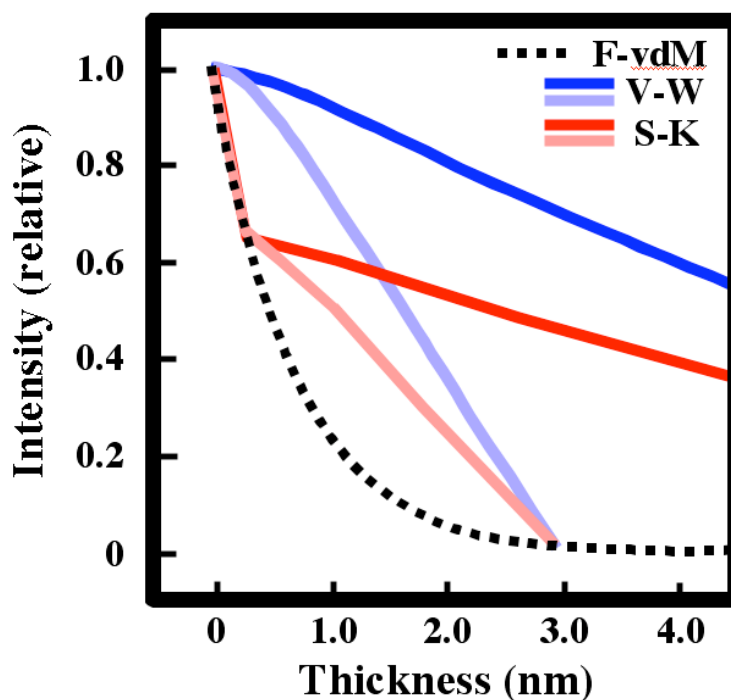


Figure 2.8: Plot of theoretical photoelectron intensity attenuation versus thickness for the three thin film growth modes. For the Volmer-Weber and Stranski-Krastanov modes, the lighter line shows the attenuation in the case of a film coalescing at a thickness of 3 nanometers. The darker line shows data for a film that does not fully coalesce until a thickness of 10 nanometers. Note that significant signal from the substrate is still measurable after the intensity corresponding to the Frank-van der Merwe growth mode is nearly zero.

The use of XPS to determine thin film growth modes is useful if the deposition rate of the material of interest can either be measured *in-situ* (i.e. by a quartz microbalance) or is reliably known from other measurements (profilometry, ellipsometry). Since the attenuation of the substrate photoelectrons is exponential, errors in thickness can have large effects on attempts to fit the data to the three models. Additionally, these models assume that the substrate is ideally flat and sharp (i.e. the film is conformal to any local topography, and no

chemical reaction occurs at the interface). If this condition is not met, then the attenuation will be significantly slower due to local thickness variations and intermixing at the interface.

2.3.3 Band Offset Measurements

While other methods exist for determining band alignment at metal-semiconductor contacts and semiconductor heterojunctions, photoelectron spectroscopy is the preferred technique because it provides a method for directly observing the electronic structure at the interface between two materials. Although ultraviolet photoelectron spectroscopy provides enhanced resolution at low binding energies, as well as improved sensitivity for angle-resolved studies, XPS provides sufficient resolution and energy to excite core levels to carry out complete band alignment measurements with good accuracy ($\pm \sim 0.1$ eV).

Grant, Waldrop, and Kraut first developed the technique for XPS measurements of band offsets in the late 1970's, studying Ge-GaAs heterojunctions grown via molecular beam epitaxy.³⁴ Since the first paper of 1978, the technique has remained essentially unchanged: the measurement is carried out in three steps, using a substrate (GaAs in the case of the earliest experiments) upon which a film (Ge) is grown in stages, ideally without having exposed the sample to atmosphere. The measurement is described by the generic band diagram shown in Figure 2.9.

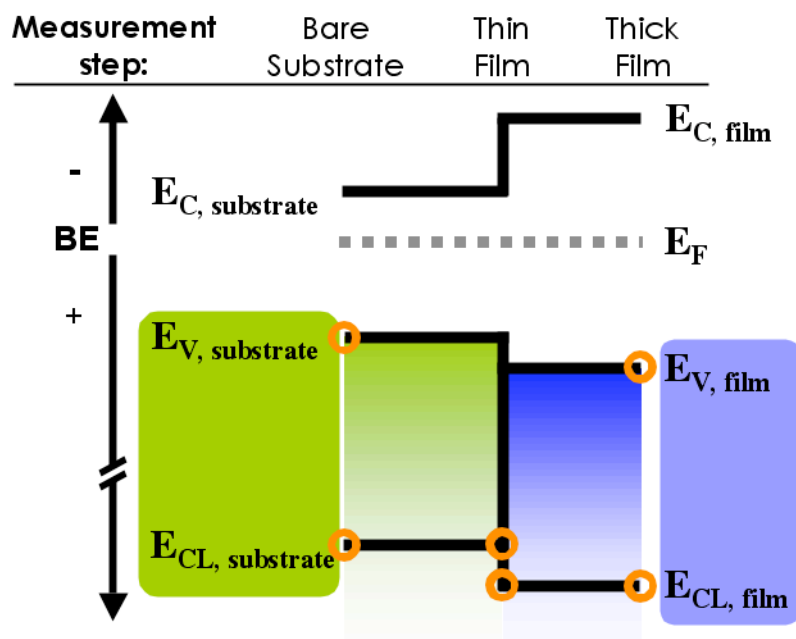


Figure 2.9: Generic band diagram showing the measurements necessary for determining valence band offsets. The open circles denote the features to be measured at each measurement stage, denoted above the diagram.

The three steps are as follows: 1) the positions of a core level and the valence band maximum are determined for the substrate. 2) The positions of the same substrate core level and a core level from the film (or second phase of the heterostructures) are measured. This measurement is performed on a film thin enough that both the substrate and film are “visible” by XPS. 3) The difference between the film core level and valence band maximum is measured. This measurement is performed after the film has been grown to a sufficient thickness that any vestiges of signal from the substrate are no longer present. The complete procedure consists of four core level measurements and two valence band measurements. Finally, valence band offset ΔE_V can be calculated using the relation

$$\Delta E_V = (E_{CL} - E_{VBM})^{\text{Substrate}} - (E_{CL} - E_{VBM})^{\text{Film}} - \Delta E_B. \quad [2.10]$$

XPS is not capable of probing states above the Fermi level, thus the conduction band offset ΔE_C cannot be determined independently. However, the sum of the band discontinuities must equal the difference in the band gaps of the two materials (see Figure 2.9), thus ΔE_C can be determined through the relation

$$\Delta E_C = \Delta E_G - \Delta E_V. \quad [2.11]$$

Since Grant *et al.* established the method for measuring band discontinuities, the technique has been heavily used, since the band alignment is a key parameter for predicting and describing the electrical behavior at semiconductor interfaces. Given silicon's status as the standard material in semiconductor devices, there have been extensive studies of band alignment at Si-insulator interfaces. For example, the Si-SiO₂ interface is particularly well characterized (see ref[35] for an extensive review) given its critical importance. The need to replace SiO₂ as the gate dielectric in Si transistors has necessitated studies of other insulators on Si, most notably the Zr- and Hf-based oxides and silicates.³⁶⁻⁴¹ II-VI heterostructures, particularly the selenides and tellurides, have also undergone significant investigation due to their applications in optical technologies such as IR detectors, and multijunction solar cells.⁴²⁻

⁴⁶ However, perhaps the most active area of band offset research is III-V heterostructures, due in part to the very wide variety of alloys available, and the fact that the nature of their technological use (quantum wells for optical (LED's, lasers) and electrical (two-dimensional electron gases) applications) depends on accurate knowledge of the band discontinuities.

Thus, extensive studies of nitride, phosphide, and arsenide structures and alloys have been performed.^{34,47-53} Finally, the interest in GaN-based transistors and related devices has highlighted the desire for knowledge of GaN-insulator band alignments. Most experimental work has focused on Ga₂O₃ and Gd₂O₃, resulting in a valence band offset of 0.9 eV,⁵⁴ but to date, studies have also been performed on Sc₂O₃, SiO₂, HfO₂, Al₂O₃, and MgO.⁵⁵⁻⁶⁴

REFERENCES

- ¹ H. Hertz, *Annalen der Physik* **267**, 983-1000 (1887).
- ² A. Einstein, *Annalen der Physik* **17**, 132 (1905).
- ³ O. W. Richardson and K. T. Compton, *Physical Review* **34**, 393-396 (1912).
- ⁴ H. Robinson, *Proceedings of the Royal Society of London Series a-Containing Papers of a Mathematical and Physical Character* **104**, 455-479 (1923).
- ⁵ H. Robinson and C. L. Young, *Proceedings of the Royal Society of London Series a-Containing Papers of a Mathematical and Physical Character*, 71-75 (1930).
- ⁶ M. De Broglie, *Seance*, 179-180 (1925).
- ⁷ M. Ference, *Physical Review* **51**, 0720-0725 (1937).
- ⁸ J. G. Jenkin, R. C. G. Leckey, and J. Liesegang, *Journal of Electron Spectroscopy and Related Phenomena* **12**, 1-35 (1977).
- ⁹ E. Sokolowski, C. Nordling, and K. Siegbahn, *Arkiv fur Fysik* **12**, 301-318 (1957).
- ¹⁰ C. Nordling, E. Sokolowski, and K. Siegbahn, *Physical Review* **105**, 1676-1677 (1957).
- ¹¹ A. Fahlman, K. Hamrin, R. Nordberg, C. Nordling, and K. Siegbahn, *Physical Review Letters* **14**, 127 (1965).
- ¹² E. Sokolowski, C. Nordling, and K. Siegbahn, *Physical Review* **110**, 776-776 (1958).
- ¹³ R. Nordberg, R. G. Albridge, T. Bergmark, U. Ericson, a. Fahlman, K. Hamrin, J. Hedman, Johansso.G, C. Nordling, K. Siegbahn, and B. Lindberg, *Nature* **214**, 481 (1967).
- ¹⁴ K. Hamrin, G. Johansson, A. Fahlman, C. Nordling, K. Siegbahn, and B. Lindberg, *Chemical Physics Letters* **1**, 557-559 (1968).
- ¹⁵ K. Hamrin, G. Johansson, U. Gelius, A. Fahlman, C. Nordllng, and K. Siegbahn, *Chemical Physics Letters* **1**, 613-615 (1968).
- ¹⁶ J. Delhalle, J. M. Andre, S. Delhalle, J. J. Pireaux, R. Caudano, and J. J. Verbist, *Journal of Chemical Physics* **60**, 595-600 (1974).

- 17 Y. S. Khodeyev, H. Siegbahn, K. Hamrin, and K. Siegbahn, *Chemical Physics Letters* **19**, 16-20 (1973).
- 18 S. Svensson, N. Martensson, E. Basilier, P. a. Malmqvist, U. Gelius, and K. Siegbahn, *Journal of Electron Spectroscopy and Related Phenomena* **9**, 51-65 (1976).
- 19 J. Nordgren, L. O. Werme, H. Agren, C. Nordling, and K. Siegbahn, *Journal of Physics B-Atomic Molecular and Optical Physics* **8**, L18 (1975).
- 20 B. Lindberg, L. Asplund, H. Fellnerfeldegg, P. Kelfve, H. Siegbahn, and K. Siegbahn, *Chemical Physics Letters* **39**, 8-10 (1976).
- 21 K. Siegbahn, *Science* **217**, 111-121 (1982).
- 22 K. Asami, K. Hashimoto, T. Masumoto, and S. Shimodaira, *Corrosion Science* **16**, 909-914 (1976).
- 23 K. Asami, K. Hashimoto, and S. Shimodaira, *Corrosion Science* **17**, 713-723 (1977).
- 24 S. Hufner and G. K. Wertheim, *Physics Letters A* **51**, 299-300 (1975).
- 25 C. R. Brundle, *Journal of Vacuum Science & Technology* **13**, 301-309 (1976).
- 26 S. Hufner, *Photoelectron Spectroscopy*, Third ed. (Springer-Verlag, New York, 2003).
- 27 M. P. Seah and W. A. Dench, *Surface and Interface Analysis* **1**, 2-11 (1979).
- 28 B. D. Ratner and D. G. Castner, in *Surface Analysis: The Principle Techniques*, edited by J. C. Vickerman (John C. Wiley & Sons, New York, 1997), p. 43-98.
- 29 D. L. Smith, *Thin-Film Deposition: Principles & Practice* (McGraw Hill, New York, 1995).
- 30 D. Briggs and M. P. Seah, *Practical Surface Analysis*, Vol. 1 (John Wiley & Sons, New York, 1990).
- 31 J. F. Moulder, W. F. Stickle, P. E. Sobol, and K. D. Bomben, *Handbook of X-ray Photoelectron Spectroscopy* (Perkin-Elmer Corporation, Eden Prairie, 1992).
- 32 J. a. Venables, *Surface Science* **300**, 798-817 (1994).
- 33 W. K. Burton, N. Cabrera, and F. C. Frank, *Philosophical Transactions of the Royal Society of London Series a-Mathematical and Physical Sciences* **243**, 299-358 (1951).

- 34 R. W. Grant, J. R. Waldrop, and E. A. Kraut, *Journal of Vacuum Science & Technology* **15**, 1451-1455 (1978).
- 35 K. Hirose, H. Nohira, K. Azuma, and T. Hattori, *Progress in Surface Science* **82**, 3-54 (2007).
- 36 G. B. Rayner, D. Kang, Y. Zhang, and G. Lucovsky, *Journal of Vacuum Science & Technology B* **20**, 1748-1758 (2002).
- 37 R. Puthenkovilakam and J. P. Chang, *Journal of Applied Physics* **96**, 2701-2707 (2004).
- 38 V. A. Gritsenko, A. V. Shaposhnikov, W. M. Kwok, H. Wong, and G. M. Jidomirov, *Thin Solid Films* **437**, 135-139 (2003).
- 39 H. Y. Yu, M. F. Li, B. J. Cho, C. C. Yeo, M. S. Joo, D. L. Kwong, J. S. Pan, C. H. Ang, J. Z. Zheng, and S. Ramanathan, *Applied Physics Letters* **81**, 376-378 (2002).
- 40 P. Panchaipetch, T. Okamoto, H. Nakamura, Y. Uraoka, T. Fuyuki, and S. Horii, *Japanese Journal of Applied Physics* **43**, 7815-7820 (2004).
- 41 H. Y. Yu, M. F. Li, and D. L. Kwong, *Thin Solid Films* **462-63**, 110-113 (2004).
- 42 E. T. Yu, M. C. Phillips, J. O. Mccaldin, and T. C. McGill, *Journal of Vacuum Science & Technology B* **9**, 2233-2237 (1991).
- 43 D. Eich, K. Ortner, U. Groh, Z. H. Chen, C. R. Becker, G. Landwehr, R. Fink, and E. Umbach, *Physica Status Solidi a-Applied Research* **173**, 261-267 (1999).
- 44 A. Bauknecht, U. Blieske, T. Kampschulte, J. Albert, H. Sehnert, M. C. Lux-Steiner, A. Klein, and W. Jaegermann, *Applied Physics Letters* **74**, 1099-1101 (1999).
- 45 G. M. Liu, T. Schulmeyer, J. Brotz, A. Klein, and W. Jaegermann, *Thin Solid Films* **431**, 477-482 (2003).
- 46 A. Marbeuf, D. Ballutaud, R. Triboulet, and Y. Marfaing, *Journal of Crystal Growth* **101**, 608-610 (1990).
- 47 O. Dehaese, X. Wallart, O. Schuler, and F. Mollot, *Journal of Applied Physics* **84**, 2127-2132 (1998).
- 48 T. Kitatani, M. Kondow, T. Kikawa, Y. Yazawa, M. Okai, and K. Uomi, *Japanese Journal of Applied Physics Part 1-Regular Papers Short Notes & Review Papers* **38**, 5003-5006 (1999).

- 49 C. F. Shih, N. C. Chen, P. H. Chang, and K. S. Liu, Japanese Journal of Applied Physics Part 1-Regular Papers Brief Communications & Review Papers **44**, 7892-7895 (2005).
- 50 C. G. Van de Walle and J. Neugebauer, Applied Physics Letters **70**, 2577-2579 (1997).
- 51 J. R. Waldrop and R. W. Grant, Applied Physics Letters **68**, 2879-2881 (1996).
- 52 J. R. Waldrop, E. a. Kraut, C. W. Farley, and R. W. Grant, Journal of Applied Physics **69**, 372-378 (1991).
- 53 C. L. Wu, C. H. Shen, and S. Gwo, Applied Physics Letters **88**, (2006).
- 54 T. S. Lay, M. Hong, J. Kwo, J. P. Mannaerts, W. H. Hung, and D. J. Huang, Solid-State Electronics **45**, 1679-1682 (2001).
- 55 J. J. Chen, B. P. Gila, M. Hlad, A. Gerger, F. Ren, C. R. Abernathy, and S. J. Pearton, Applied Physics Letters **88**, (2006).
- 56 J. J. Chen, B. P. Gila, M. Hlad, A. Gerger, F. Ren, C. R. Abernathy, and S. J. Pearton, Applied Physics Letters **88**, (2006).
- 57 J. J. Chen, M. Hlad, A. P. Gerger, B. P. Gila, F. Ren, C. R. Abernathy, and S. J. Pearton, Journal of Electronic Materials **36**, 368-372 (2007).
- 58 T. E. Cook, C. C. Fulton, W. J. Mecouch, R. F. Davis, G. Lucovsky, and R. J. Nemanich, Journal of Applied Physics **94**, 7155-7158 (2003).
- 59 T. E. Cook, C. C. Fulton, W. J. Mecouch, R. F. Davis, G. Lucovsky, and R. J. Nemanich, Journal of Applied Physics **94**, 3949-3954 (2003).
- 60 T. E. Cook, C. C. Fulton, W. J. Mecouch, K. M. Tracy, R. F. Davis, E. H. Hurt, G. Lucovsky, and R. J. Nemanich, Journal of Applied Physics **93**, 3995-4004 (2003).
- 61 T. Hashizume, S. Ootomo, T. Inagaki, and H. Hasegawa, Journal of Vacuum Science & Technology B **21**, 1828-1838 (2003).
- 62 S. K. Hong, T. Hanada, H. Makino, Y. F. Chen, H. J. Ko, T. Yao, A. Tanaka, H. Sasaki, and S. Sato, Applied Physics Letters **78**, 3349-3351 (2001).
- 63 S. K. Hong, T. Hanada, H. Makino, H. J. Ko, Y. F. Chen, T. Yao, A. Tanaka, H. Sasaki, S. Sato, D. Imai, K. Araki, and M. Shinohara, Journal of Vacuum Science & Technology B **19**, 1429-1433 (2001).

- ⁶⁴ P. F. Zhang, X. L. Liu, R. Q. Zhang, H. B. Fan, H. P. Song, H. Y. Wei, C. M. Jiao, S. Y. Yang, Q. S. Zhu, and Z. G. Wang, *Applied Physics Letters* **92**, - (2008).

3. Materials

This thesis investigates the fundamental behavior of a materials system: oxides (chiefly rocksalts) in contact with gallium nitride. Gallium nitride is a compound semiconductor currently envisioned for use in many next-generation applications requiring high RF power output at elevated temperatures. Research investigating the interface between gallium nitride and oxides results from the need for efficient device isolation, passivation of surface states, and increased functionality through polar oxides.

In this chapter, gallium nitride will be reviewed from two perspectives: the relationship between its properties and the predicted applications, and the use of metal organic chemical vapor deposition as a synthesis route for achieving high-quality material with reproducible polarity. Additionally, the current status of oxide/gallium nitride research will be reviewed, concentrating on Ga- and Si-based dielectrics, and the recent progress in rocksalt/gallium nitride research efforts.

3.1 Gallium Nitride

Gallium nitride (GaN) is a wide band gap semiconductor commercially used for optical applications. GaN belongs to the III-Nitride family of III-V semiconductors, and its band gap falls between that of InN and AlN. Owing primarily to its wide band gap and processability, it is currently under development by many research groups and companies for next-generation semiconductor devices, which are envisioned for high temperature and high

frequency operation. In this section, the properties of GaN will be reviewed in terms of the features that make it technologically attractive. Additionally, the growth of GaN will be discussed from the standpoint of controlling its polarity.

3.1.1 Properties of GaN

The aspects of GaN that make it attractive for future devices boil down to two essential factors: its wide band gap and its polar structure. The band gap of GaN, 3.4 eV, gives it potential for application for devices operating at high frequencies, high power levels, and high temperatures; in short, all of the regimes of future device technology that are largely inaccessible to Si. In Table 3.1, some of the important GaN material parameters are given in comparison to other semiconductors. This table will provide the basis for further discussion of the properties of GaN.

Table 3.1: Summary of the band gap (E_G), hole mobility (μ_n), saturation electron velocity (V_{sat}), critical electric field (E_c), thermal conductivity (λ), and dielectric permittivity (ϵ_r) of GaN, and several other semiconductors. Data taken from refs[1,2].

Material	E_G @ 300 K (eV)	μ_n ($\text{cm}^2/\text{V s}$)	V_{sat} (10^7 cm/s)	E_c (MV/cm)	λ (W/cm K)	ϵ_r
GaN	3.4	900	2.0	3.3	1.3	9
Si	1.1	1350	1.0	0.3	1.3	11.7
GaAs	1.4	8500	2.0	0.4	0.5	12.8
3C-SiC	2.3	900	2.0	1.2	4.5	9.6
6H-SiC	2.9	370	2.0	2.4	4.5	9.7
4H-SiC	3.2	720	2.0	2.0	4.5	10
Diamond	5.6	1900	2.7	5.6	20	5.5
AlN	6.1	1100	1.8	11.7	2.5	8.7

For high frequency operation the saturation drift velocity of electrons must be improved over silicon-based devices. As shown in Table 3.1, the drift velocity of all wide band gap semiconductors, as well as GaAs, is a factor of two higher than that of Si. Compound semiconductors are, in general, composed of light elements with short bond lengths. This minimizes the effect of lattice scattering, allowing the saturation velocity to increase relative to that of Si.¹ While V_{sat} for GaN is similar to that of GaAs, as shown in Figure 3.1, it saturates at a much higher electric field in GaN; advantageous because higher voltage operation allows for increased power output at high frequencies.

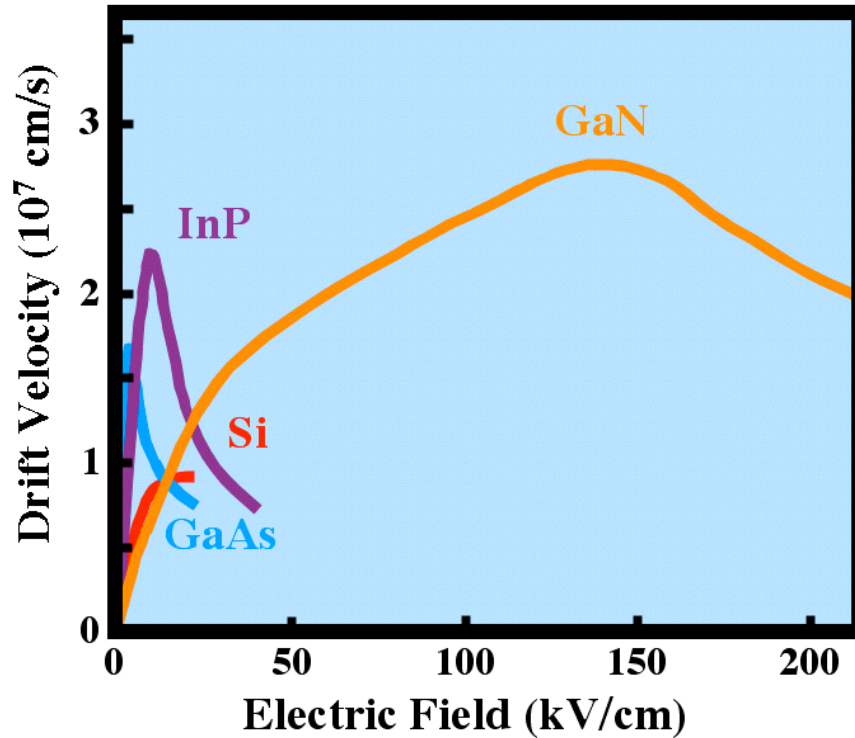


Figure 3.1: The electron drift velocities versus electric field for Si, GaAs, InP, and GaN. Adapted from [1].

For operation at high power levels, the material must be able to withstand large electric fields, so that high voltages may be supported. This is a perennial problem for GaAs-based devices. The wide band gap materials have an inherent advantage in this arena because the large band gap prevents avalanche breakdown until much higher electric fields. Table 1 shows that the critical electric field E_c is approximately one order of magnitude higher for GaN than for Si and GaAs, and is also higher than that of the SiC polymorphs. This allows

GaN to operate at higher voltages, which increases power output. The advantage of the high breakdown field also extends to circuit design, as GaN devices can operate without the need for voltage step-down electronics.^{1,3}

High temperature devices require wide band gaps for several reasons, all centering around control of carrier concentration. Control of carrier concentration in both doped and undoped regions of a device is critical in semiconductor technology, because the conductivity can vary by orders of magnitude as the amount of free carriers changes. At room temperature, the conductivity is controlled by using dopant amounts many orders of magnitude higher than the intrinsic carrier concentration, so that the intrinsic contribution to device behavior is negligible. However, the concentration of intrinsic carriers varies with temperature as

$$n_i = \sqrt{N_C N_V} e^{\frac{-E_G}{2kT}}, \quad [3.1]$$

where n_i is the intrinsic concentration, and N_C and N_V are the effective electron and hole densities of states, respectively, for the semiconductor.⁴ As Equation 3.1 shows, the intrinsic concentration is exponential with both temperature and the band gap. So, for a given semiconductor, the intrinsic concentration depends dramatically on the ambient temperature, but by choosing a semiconductor with a wider band gap, that intrinsic contribution can decrease by orders of magnitude. Figure 3.2 illustrates this effect for Si and GaN; for a given temperature, the intrinsic carrier concentration is seven to eight orders of magnitude lower in GaN. Typical dopant concentrations in semiconductor devices range from 10^{17} to 10^{18} cm⁻³.

At 600 K, the intrinsic carrier concentration in Si increases to within an order of magnitude of these values; whereas for GaN, the value remains negligible at temperatures greater than 900 K.

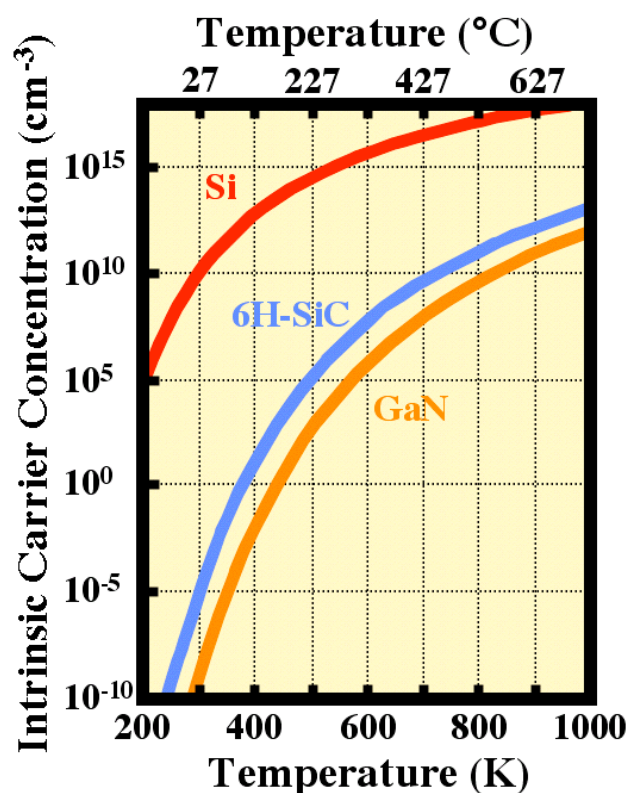


Figure 3.2: A comparison of the temperature dependence of the intrinsic carrier concentration of Si, SiC, and GaN. Note that for a given temperature, the intrinsic concentration for GaN is many orders of magnitude lower than for Si, and remains negligible (compared to typical dopant concentrations) up to temperatures in excess of 800 K. Adapted from[4].

In addition to the conductivity of doped regions, increased temperatures can also drastically influence leakage at p-n junctions. P-n junctions are a fundamental building block

of many semiconductor devices, and their off-state (reverse bias) leakage current is an important metric for baseline power consumption,⁴ and should also be kept insignificant with respect to any signal currents in the device. Under reverse bias, the leakage current can be approximated as

$$I \cong -qAn_i \left(\frac{n_i}{N_D} \sqrt{\frac{D_p}{\tau}} + \frac{W}{2\tau} \right), \quad [3.2]$$

where q is the electron charge, A and W the junction area and depletion width, respectively, N_D the n-type dopant concentration, D_p the hole diffusion constant, and τ the minority carrier lifetime.⁵ The leakage current is proportional to the square of the intrinsic carrier concentration (which is itself exponentially related to temperature), and the temperature dependence of all other terms is comparatively minor. Again, the fundamental advantage of wide band gap materials is clear: with intrinsic carrier concentrations lower by many orders of magnitude, the temperature window of operation is much wider.

Finally, the leakage at rectifying metal-semiconductor contacts is closely tied to temperature. In Chapter One it was seen that the Schottky barrier height Φ_B could be no larger than the semiconductor band gap. In practice, barrier heights rarely approach the band gap, and are typically no more than three quarters of E_G .⁴ Leakage as a result of thermionic emission over the Schottky barrier is thermally activated, and thus is exponentially dependent on temperature for a given Φ_B . Again, the possibility of much larger Schottky barrier heights

with wide band gap semiconductors such as GaN promises to reduce thermionic leakage at high temperatures by several orders of magnitude with respect to Si.

Unlike most III-V semiconductors whose equilibrium phase is zincblende, GaN crystallizes in the hexagonal wurtzite crystal structure. Wurtzite is the highest-symmetry structure that still exhibits a spontaneous polarization (in this case, along the c-axis), and is pyroelectric and piezoelectric. The origin of the dipole that leads to the polarization is shown in Figure 3.3. The consequence of this polarization is the fact that GaN crystals grown along the c-axis will be terminated by polar surfaces perpendicular to the c-axis, which carry a polarization charge that must be compensated. In GaN, the spontaneous polarization is 0.034 C/cm^3 ,⁶ which equates to a charge density on the order of $10^{13} /\text{cm}^2$. This is the magnitude of the charge that must be compensated. As shown in Figure 3.3, the compensating charge is positive in the Ga-polar case, and negative in the N-polar case. The compensation can come from a number of sources: surface Fermi level pinning to cause charge accumulation/depletion (band bending), surface reconstructions, or adsorbed species, but it must fully compensate the polarization.

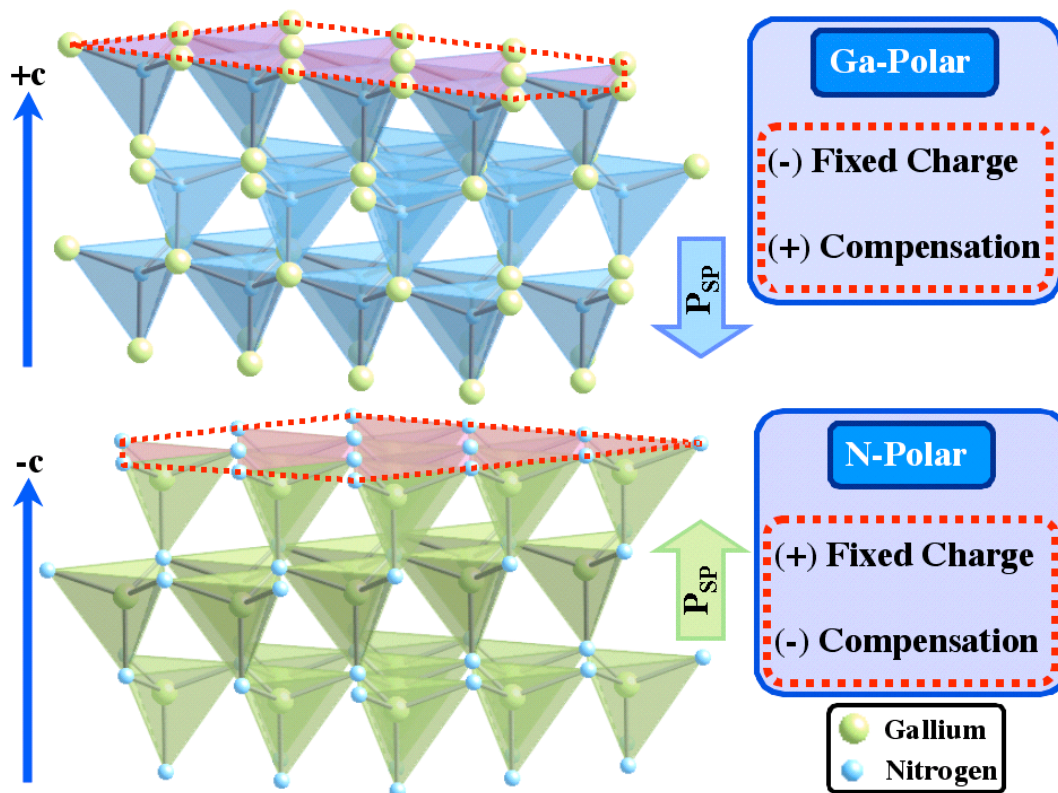


Figure 3.3: The structure of GaN viewed along [110], inclined slightly towards the c axis, using Ga- or N-centered tetrahedral to visualize the polarity. At the top, Ga-polar GaN is visualized as N-centered tetrahedra, with three Ga-N bonds (a Ga “face”) pointed towards the surface. Similarly, the N-polar case is pictured as Ga-centered tetrahedral, with a “face” of N oriented towards the surface. In practice, both polarities are found to be Ga *terminated*; the N-polar orientation is depicted as N-terminated to aid in the visualization of a simple scheme for determining the polarity. The orientation of the spontaneous polarization vector, as well as the signs of the fixed and compensating charges, are also depicted.

The polarization effect can be taken advantage of in several ways. In GaN films, lateral polarity heterostructures (LPHs) have shown some promise for optical and electrical devices. Briefly, the selective growth of Ga- and N- polar regions, which will be discussed in the following section, is accomplished by lithographic patterning of the sapphire wafer

before GaN growth, which allows precise control over the spatial distribution of the film's polarity. The increased surface reactivity of N-polar GaN is well known to cause higher oxygen incorporation during growth.^{7,8} Oxygen acts as a shallow donor, so N-polar GaN is typically found to be unintentionally n-type. Collazo *et al* recently took advantage of this behavior by growing a lateral p-n junction.⁹ The Ga-polar region was p-type via Mg doping, which was compensated in the N-polar regions by virtue of the high oxygen content. The resulting structure showed rectifying and photovoltaic behavior, as well as intense photoemission from the inversion domain boundary (a result of very efficient recombination¹⁰), demonstrating the simultaneous, side-by-side growth of n- and p-type regions of GaN on the same wafer.

Finally, the concept of 2-dimensional electron gases (2DEG) at heterostructure interfaces is well known. The polar wurtzite structure provides an additional degree of freedom in such devices due to the interaction between the polarization vectors at interfaces, as well as the piezoelectric strain induced. As shown in Figure 3.4, in AlGaN/GaN heterostructures, the band profile and strain-induced piezoelectric charges combine to create a 2DEG with a carrier concentration approximately an order of magnitude higher than that of AlGaAs/GaAs heterostructures.^{6,11} The increased carrier density in such structures makes possible higher current loads, enabling increased power output at high frequencies.

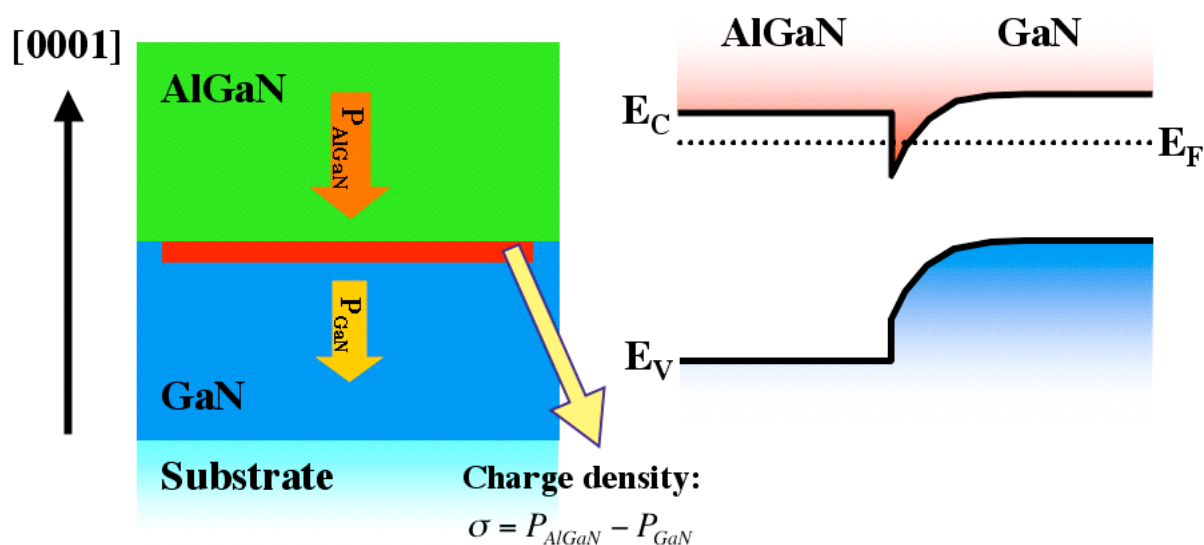


Figure 3.4: Structure forming a 2DEG (in red) at the AlGaN/GaN interface, and schematic band diagram showing the conduction band of GaN bending below the Fermi level at the interface, thus inducing the 2DEG. The discontinuity in polarization increases the 2DEG population by inducing a positive charge at the AlGaN/GaN interface, when AlGaN is grown on Ga-polar GaN.

Because the sign of the induced charge is opposite between the N- and Ga-polar faces of the crystal, the polarity of the films can also be used to control the location of the 2DEG in the device structure.^{6,11} Since the AlGaN has a higher spontaneous polarization than the GaN, the 2DEG will always form at the Ga-polar GaN/AlGaN interface; i.e. at the “tail” of the polarization vector in the GaN. Conversely, a 2DHG (2-dimensional hole gas) can be formed at the N-polar GaN/AlGaN interface. These configurations are illustrated in Figure 3.5.

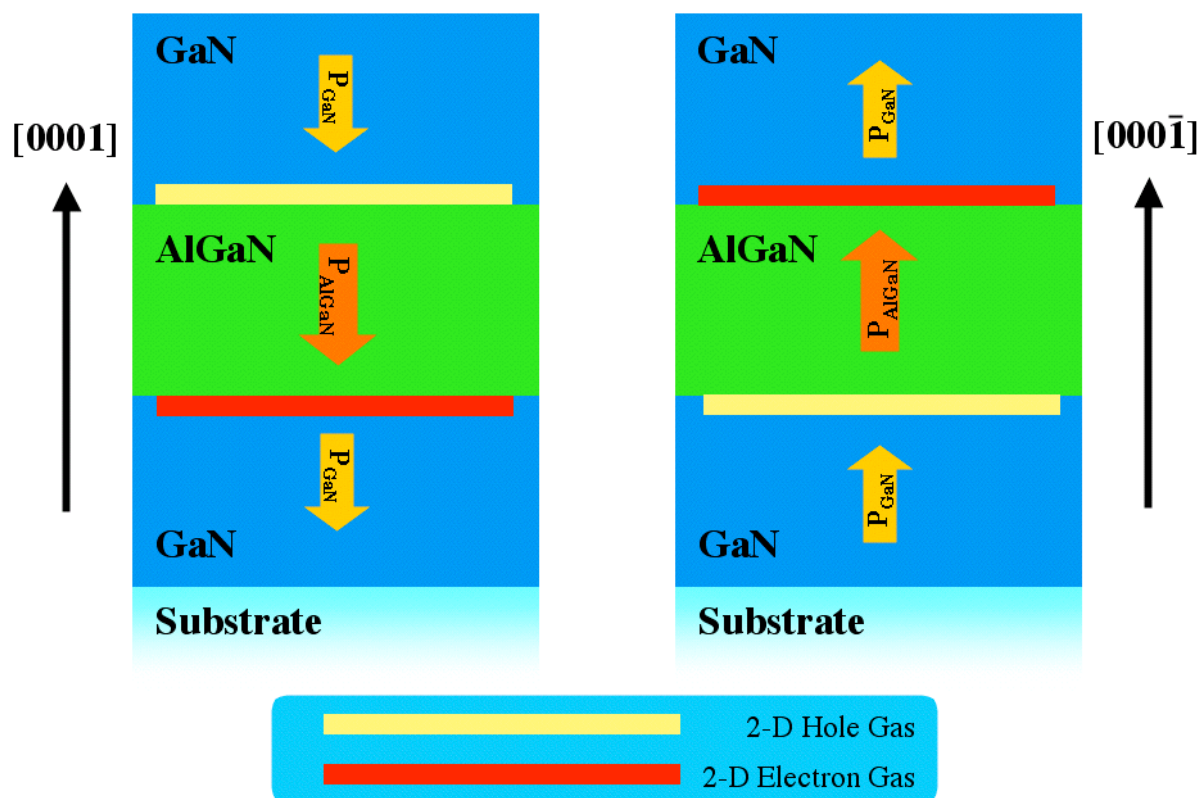


Figure 3.5: The use of the intrinsic polarity of the wurtzite structure to control the location and sign of the carrier gases at AlGaN/GaN interfaces. The larger polarization vector in AlGaN produces an excess of positive charge at the $-c$ face of the AlGaN, leading to a compensating 2DEG. Similarly, an excess of negative charge is formed at the $+c$ face, which is compensated by a 2DHG.

3.1.2. GaN Growth: Controlling GaN Polarity

The GaN films utilized in this thesis were grown using metal organic chemical vapor deposition (MOCVD). Briefly, in MOCVD, the metal (cation) species in the film is supplied by a metal organic precursor, typically dispersed in a carrier gas. The anion species (if applicable) is provided either as an elemental gas or as a precursor molecule. The deposition

is driven by the supersaturation of the film constituents in the gas phase. MOCVD growth is commonly carried out at elevated temperature; this aids the growth of high crystal quality films and facilitates cracking of the gas phase molecules, if necessary. Since the growth of the GaN films used was not carried out as part of this thesis work, but is nonetheless pertinent to the data to be presented, some specificity as to the particular process used will be given here, rather than in the experimental procedure section.

The GaN films are grown on 2-inch nominal c-axis sapphire wafers in a vertical cold-walled CVD reactor. The base pressure of the chamber is approximately 10^{-7} Torr. The substrates are inductively heated using RF coils external to the chamber, which heat a rotating graphite susceptor on which the substrates rest. The typical growth temperature is 1050 °C. Prior to growth, the sapphire wafers are cleaned by heating to 1100 °C under flowing H_2 ambient. After the hydrogen etch, the nucleation layer is prepared. This layer is the heart of GaN polarity control and will be discussed in some detail separately. To initiate growth, the substrate is held at the growth temperature, and the flow of the precursor gases and diluent gas (N_2 or H_2 , or an arbitrary combination thereof) is commenced. Triethyl gallium (TEG) is used as the Ga precursor, while ammonia (NH_3) is the N precursor. The gas flow is throttled to maintain the total pressure of the system at 20 Torr. If doping is desired, additional flows of silane (for Si, n-type doping), or bis(cyclopentadienyl)magnesium (Mg, p-type doping) can be added to the mixture. Additionally, growth of AlN or AlGaN is possible through the use of trimethyl aluminum (TMA). For further details of the growth procedure, see ref[12].

In MOCVD growth of GaN, there are a multitude of variables, which are not necessarily independent. The input flows, partial pressures, total pressure (depending on the choice of diluent gas), temperature, etc. all play a role in defining the complex process space for GaN synthesis. Typical studies of GaN MOCVD attempt to describe the growth in terms of a smaller subset of the variables (for example, varying the V/III ratio), but the complex interactions are either typically not well understood and studies of this nature have given rise to incomplete explanations, or are modeled in a complex fashion which does not encourage the conditions to be compared across systems of different configurations. Recently, the Sitar group at North Carolina State University has advocated the use of the Ga supersaturation as the overriding growth parameter to guide GaN synthesis and facilitate comparisons of processing conditions across systems (provided sufficient knowledge of the systems' behavior).¹³ The supersaturation defines the deviation of the process from thermodynamic equilibrium, and as such, gives the driving force for deposition:

$$\Delta G = RT \ln(\sigma + 1), \quad [3.3]$$

where σ is the supersaturation. The Ga supersaturation is obtained by normalizing the input partial pressure of Ga, P_{Ga} , to the equilibrium vapor pressure of Ga over GaN, P_{Ga}^0 :

$$\sigma = \frac{P_{Ga} - P_{Ga}^0}{P_{Ga}^0}. \quad [3.4]$$

The input partial pressure of Ga is known from the process gas flows and total pressure. The calculation of the supersaturation, then, depends on the determination of the equilibrium vapor pressure of Ga over GaN.

The process conditions for MOCVD growth of GaN have been chosen to ensure that the rate limiting steps for the growth are not the dissociations of the precursor gas molecules. Thus, the chemical reaction occurring at the growth surface can be written as:



from which the equilibrium constant can be obtained:

$$K_{GaN} = \frac{a_{GaN} [P_{H_2}^0]^{3/2}}{P_{Ga}^0 P_{NH_3}^0}. \quad [3.6]$$

Three equations can be established to define the molar conservation parameters; they involve the total reactor pressure P_T , the reduced pressure P_r , and the growth stoichiometry, respectively:

$$P_T = P_{Ga}^0 + P_{NH_3}^0 + P_{H_2}^0 + P_{Inert}, \quad [3.7]$$

$$P_r = P_{Ga}^0 + P_{NH_3}^0 + P_{H_2}^0, \quad [3.8]$$

and

$$P_{Ga} - P_{Ga}^0 = P_{NH_3} - P_{NH_3}^0. \quad [3.9]$$

Finally, by substituting Equations 3.6 and 3.9 into Equation 3.8, a fourth order polynomial is obtained, by which P_{Ga}^0 can be obtained:

$$(P_{Ga}^0)^4 + \left(2A + \frac{8}{K^2}\right)(P_{Ga}^0)^3 + \left(A^2 - 12\frac{B}{K^2}\right)(P_{Ga}^0)^2 + 6\frac{B^2}{K^2}P_{Ga}^0 - \frac{B^3}{K^2} = 0,$$

[3.10]

$$A \equiv P_{NH_3} - P_{Ga} = P_{Ga} \left(\frac{V}{III} - 1 \right),$$

$$B \equiv P_r - 1.$$

Thus, the equilibrium vapor pressure of Ga can be obtained in terms of the input partial pressures and the equilibrium rate constant. The rate constant itself can be calculated as a function of temperature according to ref[14]. Other parameters of interest are the “F ratio,” which describes the fraction of hydrogen gas in terms of the total diluent gas flow (necessary because hydrogen, a common diluent in MOCVD, is also a product of the synthesis reaction), and α , or the fraction of NH_3 molecules dissociated to provide gaseous nitrogen (necessary to account for the slow dissociation of ammonia). For a more detailed discussion of the calculation of the Ga supersaturation, including methods for calculating the reduced pressure without knowledge of the equilibrium values, see refs[13,15]. Figure 3.6 shows the variation of Ga supersaturation with the V/III ratio and the F ratio.

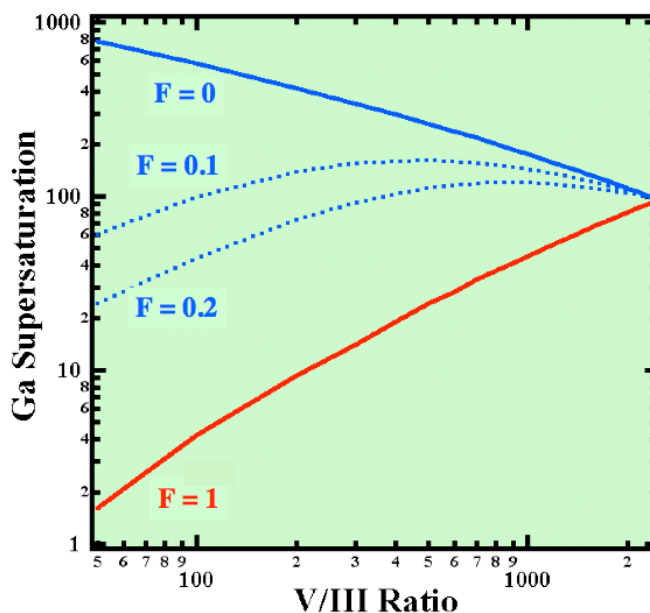


Figure 3.6: Ga supersaturation as a function of V/III ratio and F ratio. If $F = 0$, then the partial pressure of hydrogen in the process is 0 Torr, which is not experimentally obtainable since H_2 is a product of the synthesis reaction. Thus, typical process conditions using N_2 as the sole diluent gas empirically correspond to the $F = 0.2$ curve. The practical range of Ga supersaturation is therefore $\sim 5 - 100$. Plot courtesy of Dr. R. Collazo.

Mita *et al.* have found^{13,15} that the nucleation behavior of the GaN films and surface morphology is related to the Ga supersaturation as expected by BCF (Burton Cabrera Frank) Theory.¹⁶ Additionally, they showed that the supersaturation affects the carrier compensation level by controlling the incorporation of carbon in the growing films, thus correlating the supersaturation with material properties. The original assertion that the supersaturation is a more appropriate metric for comparing film growth parameters is supported by the

demonstration that films grown with apparently differing process variables (V/III ratio and F factor) but the same value of supersaturation have equivalent properties.

The nature of the nucleation layer on which the GaN film is grown ultimately determines the film polarity. For MOCVD, the situation can be summed up as follows: In the GaN process flow briefly outlined previously, the growth of GaN can commence after the H₂ annealing step, or after the growth of the buffer layer. If the growth is begun directly after the H₂ etch, then the GaN film will be Ga-polar as a result. If a low-temperature AlN (LT-AlN) layer is grown as the nucleation layer, the GaN film will also be Ga-polar. However, if, after the sapphire wafer is H₂ etched, it is exposed to a nitridizing ammonia flux at high temperatures (~950 °C), the GaN film will be N-polar.¹⁷ As mentioned previously, both polarities can be grown on the same wafer in a controlled fashion. This is accomplished by subjecting the sapphire wafer to a high temperature nitridation step, followed by the growth of a LT-AlN layer. Photolithographic patterning of the LT-AlN layer then allows simultaneous growth of Ga- and N-polar films.⁹

The orientation of the polarization is determined by the interfacial chemistry that results from each surface treatment. This argument is based on bond strengths, and was first proposed in 2001.¹⁸ For the case of the LT-AlN layer, the first layer to be deposited is Al, as sapphire wafers tend to be oxygen-terminated. The Al-O bond is stronger than the Al-N bond, thus this first monolayer “belongs” to the sapphire, and the first monolayer of the AlN film is the first N monolayer. Because the Al monolayer is strongly bound to the sapphire, the N monolayer will be singly bound to the Al, leaving three unsatisfied bonds pointing

“up” (in the +c direction). Referring back to Figure 3.3, this bond orientation results in an Al-polar AlN film. Once the GaN growth is commenced, the corresponding polarity is then Ga-polar. Similarly, for the case of GaN growth with no nucleation layer, the first monolayer of N deposited “belongs” to the GaN, and singly bonds to the sapphire wafer. The high-temperature nitridation is thought to result in N-polar GaN films, because the exposure to ammonia at high temperature forces the nitrogen into three-coordination with the Al monolayer at the sapphire surface (the nitrogen tetrahedra are then oriented in the opposite sense than in the case of the LT-AlN layer), thus encouraging N-polar GaN films. The interfacial arrangements responsible for the polarity of GaN films are depicted in Figure 3.7.

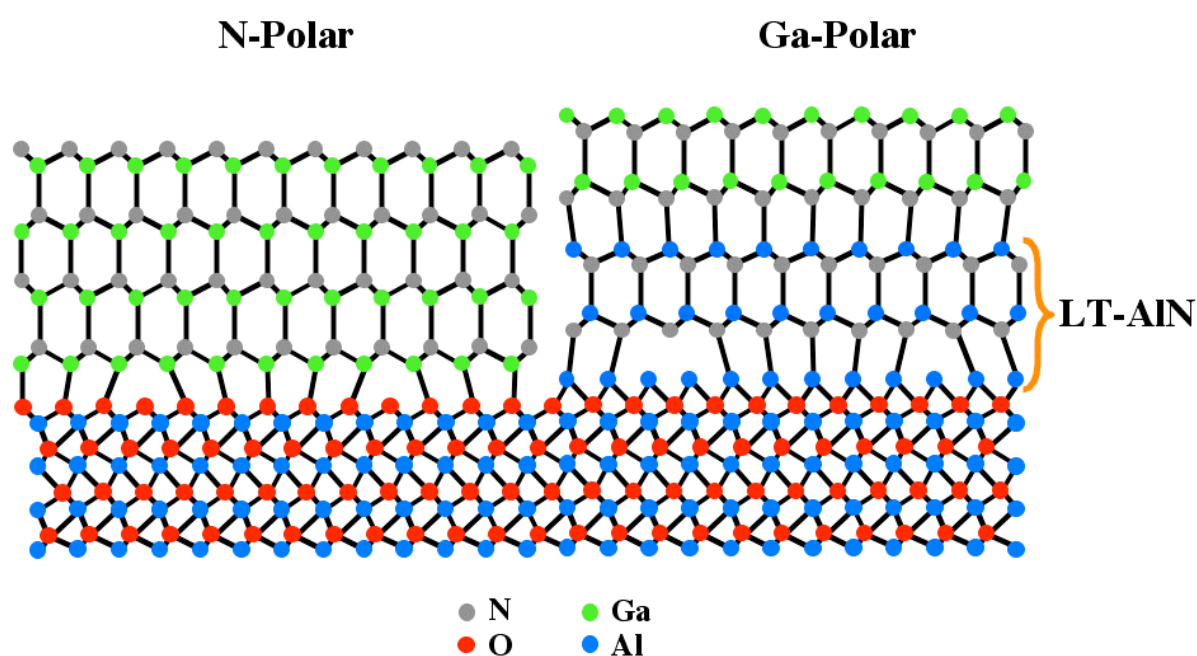


Figure 3.7: Schematic interfacial bonding arrangements for N- and Ga-polar GaN on a sapphire substrate. Adapted from [18].

3.2 Dielectrics on GaN

The success of Si-based semiconductor devices is due in large part to the behavior of silicon's native oxide, SiO_2 , and the precision with which the Si/ SiO_2 interface can be engineered. In order for GaN-based microelectronics to achieve similar success, an analogous oxide/GaN system must be developed. The largest body of research into oxide/GaN interfaces has been concerned with the use of oxides as gates in metal-oxide-semiconductor field effect transistors (MOSFETs) and as surface passivation layers in high electron mobility transistors (HEMTs). This section will briefly summarize some of the research efforts and outcomes in oxide/GaN research.

One of the earliest investigations into device quality oxide/compound semiconductor interfaces was the use of $\text{Ga}_2\text{O}_3(\text{Gd}_2\text{O}_3)$ films on GaAs. The interest in this material system grew out of the example of the SiO_2/Si interface. In that case, the native oxide displays excellent chemical stability in contact with the semiconductor, and the interface has a low density of trap sites. SiO_2 is thermally grown on Si, but this process is challenging in the case of GaAs, because there is competition between oxidation of the Ga and the As, leading to a chemically inhomogeneous interface of low quality.¹⁹ Investigations of the native Ga_2O_3 on GaAs thus focused on e-beam evaporation from garnet $\text{Gd}_3\text{Ga}_5\text{O}_{12}$ single crystals. The garnet sublimes incongruently, so if the e-beam power is controlled closely, the resulting thin film is $\text{Ga}_2\text{O}_3(\text{Gd}_2\text{O}_3)$, with a low concentration of Gd_2O_3 .²⁰⁻²² This technique has been extended with reasonable success to GaN. For example, refs[19,23,24] demonstrate amorphous-

Ga₂O₃(Gd₂O₃)/GaN interfaces with low surface roughness (3 Å as measured by x-ray reflectivity) and a low density of interface traps ($2 \times 10^{10} - 10^{11} \text{ cm}^{-2}$). Ren *et al* and Chang *et al* show that the leakage current through a MOS structure is several orders of magnitude lower than for Schottky gates, and Ren *et al* and Johnson *et al* demonstrate saturating drain current behavior in MOSFET structures.

The use of Si-based dielectrics on GaN has also garnered a high degree of attention. Amorphous SiO₂ has been investigated because of its large band gap; the wide band gap of GaN disqualifies many oxides for use in gate structures because band offsets are expected to be insufficient. However, the band gap of SiO₂ approaches 9 eV, so generous band offsets are to be expected. Also, amorphous Si₃N₄ films have seen broad use in HEMT structures as an effective surface passivation layer. Sawada *et al* showed that metal gates on GaN provide inhomogeneous Schottky barrier heights, attributed to surface crystal defects, but SiO₂ gates were shown to have defect densities of $\sim 2 \times 10^{11} \text{ cm}^{-2}$ in the as-deposited state, which was improved to $< 1 \times 10^{11} \text{ cm}^{-2}$ after a 500 °C H₂ anneal.²⁵ Later, Niiyama *et al* reported a similar result following a 1000 °C N₂ anneal, which they showed decreased the density of interface states near the band edges of GaN, as well as at a defect-related discrete level near the conduction band edge.²⁶ They attribute the change in state density to an improvement in the SiO₂ quality, as observed by a decrease in the etch rate under a buffered HF solution.

Amorphous Si₃N₄ dielectric layers have become a standard part of HEMT processing in order to passivate surface states at the AlGaN free surface. These surface states are too slow to empty at the frequencies of interest, which leads to current collapse due the “virtual

gate effect,” preventing effective modulation of the channel by the gate. Si_3N_4 has been shown to effectively passivate these states. Several investigators note small-signal improvements in output power of $\sim 10\%$ with large-signal performance often increasing by as much as 100%, with similar large improvements in breakdown fields.²⁷⁻²⁹ Lu *et al* specifically cite an increase in the 2DEG density of HEMTS along with lower gate leakage and off-state drain current, again suggesting the efficacy of these layers.³⁰ Despite its wider band gap, SiO_2 is shown to be less effective at preventing leakage and passivating surface sites as shown by Javorka *et al*, who note that compared to Si_3N_4 , SiO_2 slightly degrades RF performance of HEMTs.³¹ Desmaris *et al* reinforce this conclusion, by showing in 2008 that smoothly varying the composition of a silicon oxynitride reveals improved performance as the oxygen content of the passivating layer decreases.³²

The rocksalt oxides, particularly MgO and CaO, are also under recent scrutiny for applications in GaN electronics. While MgO has been investigated by several groups for use as a gate oxide in GaN MOSFETs or as a HEMT passivating layer,³³⁻³⁶ the rocksalt oxides have also been envisioned as epitaxial barrier layers in devices combining III-Nitrides and functional oxides such as ferroelectrics and multiferroics. Such devices would exploit the polarization discontinuity at the oxide/GaN interface, much as it is at AlGaN/GaN interfaces, with the important difference that in functional oxides such as lead zirconate titanate or bismuth ferrite, the polarization can be switched and modulated through a temperature change, applied electric field, induced strain, or a combination of the three. In these structures, the functionality of the oxides provides an additional “handle” for controlling the

2DEG.³⁷ Most of these oxides have band gaps similar to that of GaN, so most researchers expect large leakage currents through these structures, due to small band offsets. For this reason, the rocksalt oxides are of interest to act as buffer layers in such devices, as their band gaps are in the range of 7 – 8 eV.³⁸ The research in this area is in its infancy, and much of the work to be presented in this thesis is concerned with basic questions surrounding these proposed devices.

Irokawa *et al* demonstrated epitaxial MgO films on p-type GaN for use as gate oxides in a MOSFET structure.³⁶ Their early results do not show saturating drain current behavior, but the MgO dielectric displays low gate leakage suggesting the expected large band offsets. Later, Chen *et al* measured the band offsets using XPS, finding $\Delta E_v = 1.1$ eV, corresponding to a conduction band offset of 3.3 eV.³⁹ The same group has also investigated MgCaO alloys for lattice matching efforts to GaN. They found that lattice matched alloys had better crystal quality than either of the unary components, and were more effective at passivating surface states in HEMT structures.³³ Later, the band offsets of such alloys in contact with GaN were measured. For this system, a valence band offset of 0.7 eV, and a conduction band offset of 3.4 eV was found.⁴⁰

The Electronic Oxides Group at North Carolina State University has published a significant body of research concerning the details of molecular beam epitaxy (MBE) of rocksalt oxides on GaN surfaces. In 2006, Craft *et al* reported the adsorption-controlled growth mechanism for MgO films on GaN, in which the volatility of the Mg metal flux prevents deposition at elevated substrate temperatures until an oxidizing flux is introduced.⁴¹

Later, Losego *et al* reported epitaxial CaO growth on GaN, but in this case the lower vapor pressure of the Ca metal species precluded a similar growth scheme. Nonetheless, high-quality films were reported, with x-ray rocking curve widths less than 0.25° . Additionally, the atmospheric stability of these films was addressed; bulk conversion of the CaO film to the hydroxide phase Ca(OH)_2 was observed after several hours of air exposure, by x-ray diffraction. This effect could be eliminated through the use of a 5 nm MgO capping layer.⁴² A study of the metastable YbO phase was also undertaken by MBE, with stabilization of this phase possible by careful flux control to force the Yb cations into the 2+ state. Solid solutions of YbCaO were possible but do not aid in lattice matching efforts to GaN, as both oxides have larger lattice constants. YbMgO alloys would theoretically be of interest for lattice matching, but the great differences in growth behavior and process space make successful growth of such films unlikely.⁴³ For a thorough description of the rocksalt oxide/GaN growth behavior research at North Carolina State University, see ref[44].

REFERENCES

- ¹ H. Okumura, Japanese Journal Of Applied Physics Part 1-Regular Papers Brief Communications & Review Papers **45**, 7565-7586 (2006).
- ² J. Millan, IET Circuits Devices & Systems **1**, 372-379 (2007).
- ³ Y. Wu and P. Parikh, Compound Semiconductor **12**, 21 (2006).
- ⁴ P. G. Neudeck, R. S. Okojie, and L. Y. Chen, Proceedings Of The IEEE **90**, 1065-1076 (2002).
- ⁵ S. M. Sze, *Physics of Semiconductor Devices* (John Wiley & Sons, New York, 1981).
- ⁶ O. Ambacher, J. Smart, J. R. Shealy, N. G. Weimann, K. Chu, M. Murphy, W. J. Schaff, L. F. Eastman, R. Dimitrov, L. Wittmer, M. Stutzmann, W. Rieger, and J. Hilsenbeck, Journal Of Applied Physics **85**, 3222-3233 (1999).
- ⁷ M. Sumiya and S. Fuke, MRS Internet Journal Of Nitride Semiconductor Research **9** (2004).
- ⁸ T. K. Zywietz, J. Neugebauer, and M. Scheffler, Applied Physics Letters **74**, 1695-1697 (1999).
- ⁹ R. Collazo, S. Mita, A. Rice, R. F. Dalmau, and Z. Sitar, Applied Physics Letters **91**, 212103 (2007).
- ¹⁰ P. J. Schuck, M. D. Mason, R. D. Grober, O. Ambacher, A. P. Lima, C. Miskys, R. Dimitrov, and M. Stutzmann, Applied Physics Letters **79**, 952-954 (2001).
- ¹¹ R. Dimitrov, M. Murphy, J. Smart, W. Schaff, J. R. Shealy, L. F. Eastman, O. Ambacher, and M. Stutzmann, Journal Of Applied Physics **87**, 3375-3380 (2000).
- ¹² R. Collazo, S. Mita, A. Aleksov, R. Schlessler, and Z. Sitar, Journal of Crystal Growth **287**, 586-590 (2006).
- ¹³ S. Mita, R. Collazo, A. Rice, R. F. Dalmau, and Z. Sitar, Journal Of Applied Physics **104**, 013521 (2008).
- ¹⁴ A. Koukitu and Y. Kumagai, Journal of Physics-Condensed Matter **13**, 6907-6934 (2001).

- 15 S. Mita, Thesis, North Carolina State University, 2007.
- 16 W. K. Burton, N. Cabrera, and F. C. Frank, *Philosophical Transactions of the Royal Society of London Series a-Mathematical and Physical Sciences* **243**, 299-358 (1951).
- 17 F. Liu, R. Collazo, S. Mita, Z. Sitar, G. Duscher, and S. J. Pennycook, *Applied Physics Letters* **91** (2007).
- 18 M. Stutzmann, O. Ambacher, M. Eickhoff, U. Karrer, A. L. Pimenta, R. Neuberger, J. Schalwig, R. Dimitrov, P. J. Schuck, and R. D. Grober, *Physica Status Solidi B-Basic Research* **228**, 505-512 (2001).
- 19 M. A. L. Johnson, D. W. Barlage, and D. Braddock, *Materials Research Society Symposium Proceedings* **829**, B.7.7.1 (2005).
- 20 M. Hong, J. P. Mannaerts, J. E. Bower, J. Kwo, M. Passlack, W. Y. Hwang, and L. W. Tu, *Journal Of Crystal Growth* **175**, 422-427 (1997).
- 21 M. Hong, M. Passlack, J. P. Mannaerts, J. Kwo, S. N. G. Chu, N. Moriya, S. Y. Hou, and V. J. Fratello, *Journal Of Vacuum Science & Technology B* **14**, 2297-2300 (1996).
- 22 F. Ren, M. Hong, J. M. Kuo, W. S. Hobson, J. R. Lothian, H. S. Tsai, J. Lin, J. P. Mannaerts, J. Kwo, S. N. G. Chu, Y. K. Chen, and A. Y. Cho, *Gallium Arsenide Integrated Circuit Symposium*, 18-21 (1997).
- 23 Y. C. Chang, Y. J. Lee, Y. N. Chiu, T. D. Lin, S. Y. Wu, H. C. Chiu, J. Kwo, Y. H. Wang, and M. Hong, *Journal Of Crystal Growth* **301**, 390-393 (2007).
- 24 F. Ren, M. Hong, S. N. G. Chu, M. A. Marcus, M. J. Schurman, A. Baca, S. J. Pearton, and C. R. Abernathy, *Applied Physics Letters* **73**, 3893-3895 (1998).
- 25 T. Sawada, Y. Ito, K. Imai, K. Suzuki, H. Tomozawa, and S. Sakai, *Applied Surface Science* **159**, 449-455 (2000).
- 26 Y. Niiyama, T. Shinagawa, S. Ootomo, H. Kambayashi, T. Nomura, and S. Yoshida, *Physica Status Solidi A-Applications And Materials Science* **204**, 2032-2036 (2007).
- 27 B. M. Green, K. K. Chu, E. M. Chumbes, J. A. Smart, J. R. Shealy, and L. F. Eastman, *IEEE Electron Device Letters* **21**, 268-270 (2000).
- 28 S. Keller, Y. F. Wu, G. Parish, N. Q. Ziang, J. J. Xu, B. P. Keller, S. P. DenBaars, and U. K. Mishra, *IEEE Transactions On Electron Devices* **48**, 552-559 (2001).

- 29 J.-S. Lee, A. Vescan, A. Wieszt, R. Dietrich, H. Leier, and Y.-S. Kwon, *Electronics Letters* **37**, 130-132 (2001).
- 30 W. Lu, V. Kumar, R. Schwindt, E. Piner, and I. Adesida, *Solid-State Electronics* **46**, 1441-1444 (2002).
- 31 P. Javorka, J. Bernat, A. Fox, M. Marso, H. Luth, and P. Kordos, *Electronics Letters* **39**, 1155-1157 (2003).
- 32 V. Desmaris, J. Y. Shiu, N. Rorsman, H. Zirath, and E. Y. Chang, *Solid-State Electronics* **52**, 632-636 (2008).
- 33 B. P. Gila, M. Hlad, A. H. Onstine, R. Frazier, G. T. Thaler, A. Herrero, E. Lambers, C. R. Abernathy, S. J. Pearton, T. Anderson, S. Jang, F. Ren, N. Moser, R. C. Fitch, and M. Freund, *Applied Physics Letters* **87** (2005).
- 34 B. P. Gila, G. T. Thaler, A. H. Onstine, M. Hlad, A. Gerger, A. Herrero, K. K. Allums, D. Stodilka, S. Jang, B. Kang, T. Anderson, C. R. Abernathy, F. Ren, and S. J. Pearton, *Solid-State Electronics* **50**, 1016-1023 (2006).
- 35 J. K. Gillespie, R. C. Fitch, J. Sewell, R. Dettmer, G. D. Via, A. Crespo, T. J. Jenkins, B. Luo, R. Mehandru, J. Kim, F. Ren, B. P. Gila, A. H. Onstine, C. R. Abernathy, and S. J. Pearton, *Ieee Electron Device Letters* **23**, 505-507 (2002).
- 36 Y. Irokawa, Y. Nakano, M. Ishiko, T. Kachi, J. Kim, F. Ren, B. P. Gila, A. H. Onstine, C. R. Abernathy, S. J. Pearton, C. C. Pan, G. T. Chen, and J. I. Chyi, *Applied Physics Letters* **84**, 2919-2921 (2004).
- 37 M. Singh, Y. R. Wu, and J. Singh, *Solid-State Electronics* **47**, 2155-2159 (2003).
- 38 R. C. Whited, C. J. Flaten, and W. C. Walker, *Solid State Communications* **13**, 1903-1905 (1973).
- 39 J. J. Chen, B. P. Gila, M. Hlad, A. Gerger, F. Ren, C. R. Abernathy, and S. J. Pearton, *Applied Physics Letters* **88**, - (2006).
- 40 J. J. Chen, M. Hlad, A. P. Gerger, B. P. Gila, F. Ren, C. R. Abernathy, and S. J. Pearton, *Journal of Electronic Materials* **36**, 368-372 (2007).
- 41 H. S. Craft, J. F. Ihlefeld, M. D. Losego, R. Collazo, Z. Sitar, and J. P. Maria, *Applied Physics Letters* **88**, 212906 (2006).
- 42 M. D. Losego, S. Mita, R. Collazo, Z. Sitar, and J. P. Maria, *Journal of Vacuum Science & Technology B* **25**, 1029-1032 (2007).

- ⁴³ M. D. Losego, S. Mita, R. Collazo, Z. Sitar, and J. P. Maria, *Journal of Crystal Growth* **310**, 51-56 (2008).
- ⁴⁴ M. D. Losego, Thesis, North Carolina State University, 2008.

4. Experimental Procedure

This thesis is partially composed of the work presented by three peer-reviewed manuscripts. While each chapter contains certain experimental details necessary to each investigation, the purpose of this chapter is to provide additional information regarding the experimental work. The chapter is divided into three sections: the first describes the equipment and the conditions used, the second briefly describes the generalized procedure for preparing the GaN substrates, and the third gives additional detail regarding the experimental specifics.

4.1 Experimental Equipment

The film synthesis and spectroscopic characterization were carried out in a series of ultra-high vacuum (UHV) chambers connected via a UHV transfer line. A schematic of the complete system is shown in Figure 4.1. The transfer line base pressure is 1×10^{-9} Torr, and the sample pucks are transported on a rolling transfer fork magnetically coupled to an external manipulator.

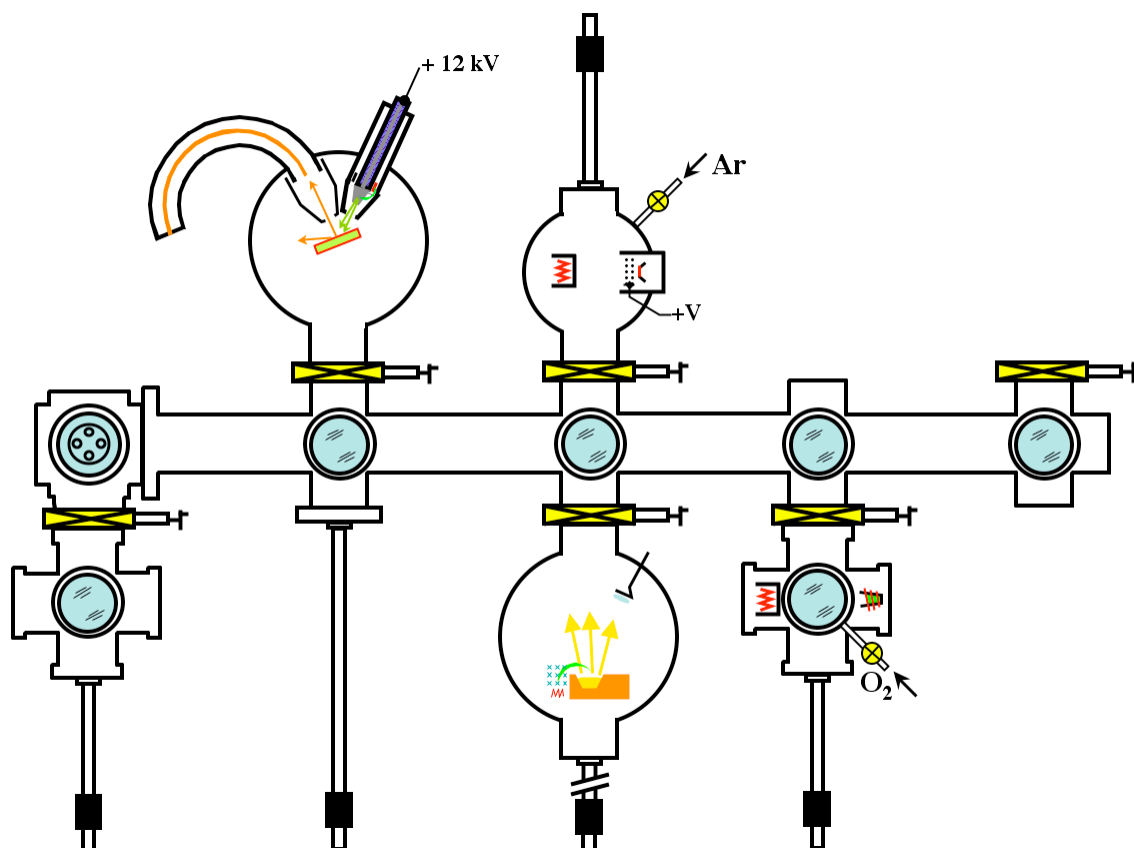


Figure 4.1: Schematic diagram of the Sitar surface analysis cluster. The system consists of an ion-pumped UHV transfer line linking four UHV chambers and a load lock. From left to right: load lock for sample introduction (bottom), surface analysis chamber for XPS experiments (top), e-beam metal deposition (bottom) and UHV anneal and ion beam sputter (top), and single-cell oxide MBE (bottom).

4.1.1 Surface Analysis Chamber: XPS

All spectroscopic experiments were conducted in a chamber specifically designed for XPS. The chamber is ion-pumped to a base pressure of $<1 \times 10^{-10}$ Torr. The system utilizes VG equipment consisting of a water-cooled, dual-anode (Al, Mg) x-ray source and a

clamshell-type concentric hemispherical analyzer. The radiation source is not monochromated, yielding x-ray energies of 1253.6 eV and 1486.6 eV (Mg, Al), with nominal radiation linewidths of 0.7 and 0.85 eV, respectively (see Table 2.1). The source irradiates a large area (several cm²) of the sample puck; the collection area is defined by the size of the spectrometer entrance slit, an “image” of which is projected onto the sample by the spectrometer electrostatic lens. For this research, the collection area is approximately 1 cm by 2 cm.

The spectrometer is a concentric hemispherical analyzer with a 10 cm radius. For survey scans, the pass energy was set to 50 eV to improve the signal-to-noise ratio. For detailed scans of core levels and valence regions, the pass energy was set to 20 eV to provide acceptable energy resolution while maintaining a sufficient signal-to-noise ratio for reasonable collection times. Using Equation 2.5, then, the base resolution of the spectrometer when operating at 20 eV pass energy can be estimated as 1.8 eV, or a minimum observable FWHM of photoelectron lines of 0.9 eV. The total experimental resolution, then, is equal to the square root of the sum of the squares of the three contributing components: the spectrometer resolution, the x-ray linewidth, and the natural linewidth of the photoelectron line of interest.

$$\Delta E_T = \sqrt{\Delta E_S + \Delta E_X + \Delta E_L} \quad [4.1]$$

In practice, the natural linewidth of most photoelectron lines is much smaller than that of the x-ray source and the spectrometer resolution, so the resolution is chiefly limited by the

instrumental terms. For an analyzer operating at a pass energy of 20 eV and a source utilizing Al K α radiation, the instrumental resolution for this work is then 1.2 eV; using Mg K α radiation the resolution is 1.1 eV.

4.1.2 Molecular Beam Epitaxy: Film Growth

For this work, the Sitar transfer line was upfitted with a small MBE chamber to allow *in situ* growth of rocksalt oxide films. This capability facilitates the execution of band alignment measurements and growth mode experiments, both of which are ideally performed without breaking vacuum to preserve the as-grown film surface morphology and chemistry. The bulk of the chamber consists of a six-way 6" conflat cross. To the bottom flange, a 4 1/2" conflat tee and nipple were added to provide mounting ports for one standard effusion cell and a turbomolecular pump. To the side flange, a 2 3/4" 6-way cross was attached to provide space for a shutter to block the metal flux at the substrate, an ion gauge, and the leak valve through which the oxygen flux was supplied. The top flange of the 6" cross is occupied by a linear manipulator, to which the substrate heater is attached. The substrate heater is constructed of two stainless steel posts to support the heater and carry electrical current, fixed to a BN cup, which contains the heating element, a spiral-wound Ta wire. The base pressure of this chamber is approximately 1×10^{-9} Torr, and the substrate temperature was measured by an IR pyrometer aimed at the side of the Mo sample puck.

Typical growth conditions for MgO films on GaN were a substrate temperature of 250 °C, an effusion cell temperature of 400 °C, and a molecular oxygen overpressure of $1 \times$

10^{-6} Torr. Using these conditions, the relative fluxes of the growth species can be estimated. At 400 °C, the equilibrium vapor pressure of Mg is 2×10^{-3} Torr.¹ This corresponds to an atomic flux of

$$J \left[\frac{\text{atoms}}{\text{cm}^2 \cdot \text{s}} \right] = 3.51 \times 10^{22} \frac{P}{\sqrt{MT}}, \quad [4.2]$$

where P is the vapor pressure in Torr, M is the molecular weight of the species of interest in grams, and T is the absolute temperature.¹ For Mg, this corresponds to a flux of 8.3×10^{17} atoms \cdot cm⁻² \cdot s⁻¹, at the mouth of the effusion cell. The “throw” of the MBE (the effusion cell to substrate distance) is 22 cm. The flux of Mg at the substrate, then, is given by

$$J_0 = \frac{J}{\pi r^2}, \quad [4.3]$$

where r is the throw.¹ This results in an impinging flux of 5.4×10^{15} atoms \cdot cm⁻² \cdot s⁻¹, or approximately 0.5 monolayers per second. The oxygen flux can be estimated according to Equation 4.2 as 3.6×10^{14} molecules \cdot cm⁻² \cdot s⁻¹, or 7.2×10^{14} atoms \cdot cm⁻² \cdot s⁻¹. Thus the relative fluxes of metal species and oxygen atoms are nearly matched, with a slight excess of oxygen. The observed growth rate of MgO films on GaN as measured by step profilometry is 2.5 nm/min. Taking the impinging metal flux of ~0.5 monolayers per second as the limiting factor, the “ideal” growth rate of a (111)-oriented MgO film would be approximately 3.6 nm/min. However, the volatility of Mg metal in this growth environment is well known,^{2,3} so the overall growth rate is somewhat lower than what is estimated by the fluxes.

For the case of CaO growth on GaN substrates, growth conditions consist of an effusion cell temperature of 510 °C, a substrate temperature of 500 °C, with an oxygen overpressure of 1×10^{-6} Torr. The relative fluxes can be estimated using Equations 4.2 and 4.3 in a fashion analogous to the case of MgO growth. At 510 °C, the equilibrium vapor pressure of Ca metal is $\sim 5 \times 10^{-4}$ Torr. This corresponds to a Ca flux at the substrate of $\sim 1 \times 10^{14}$ atoms \cdot cm $^{-2}$ \cdot s $^{-1}$, or ~ 0.1 monolayers per second. The oxygen flux is identical to the case of MgO growth. The growth rate as measured by step profilometry was found to be ~ 0.8 nm/min, which corresponds exactly to the rate estimated from the metal flux. In this case, the agreement is not surprising, given the negligible Ca reevaporation observed during MBE growth experiments.^{3,4}

4.1.3 Annealing Chamber: Surface Preparation

Typical XPS and growth experiments were preceded by a brief (~ 1 hour) offgassing anneal at 400 °C in a separate chamber to remove excess surface contamination from GaN surfaces. This chamber consists of a small heater of similar design as that described for the MBE growth chamber, an ion gun for surface cleaning, and a gas manifold to supply Ar to the ion gun. The chamber is pumped by a turbomolecular pump to a base pressure of $\sim 3 \times 10^{-9}$ Torr. The offgassing anneal was effective in reducing adventitious contamination (O and C) to sub-monolayer levels.

For GaN surface stoichiometry measurements, the as-measured stoichiometry is heavily influenced by surface contamination, because the photoelectron lines of interest (Ga

2p and N 1s) have a wide separation in binding energy. This large binding energy difference makes the Ga 2p line significantly more surface sensitive, as it resides at a much higher energy (~1120 eV) than the N 1s line (~400 eV). Thus, the Ga 2p line is more rapidly attenuated by the presence of any surface contamination. For precise measurements of the surface stoichiometry, then, the ion gun was often employed in this research in an effort to remove all remaining contaminants. The ion gun was operated at a beam voltage of 2.0 kV, and an electron emission current of 30 mA.

4.1.4 Electron Beam Evaporator: Metal Deposition

For some experiments in this work, Au deposition following spectroscopic investigations was employed in an effort to verify the charging state of the sample. For this purpose, the e-beam evaporator attached to the Sitar transfer line could be utilized. This system consists of an Evap CV-6 e-beam source and hearth manufactured by MDC and operated at a beam voltage of 7 kV and filament current of 220 mA for Au deposition. The thickness of the deposited film could be measured *in situ* by a quartz crystal deposition monitor. The final thickness of Au films utilized in this study was typically 20 nm.

4.1.5 Additional Equipment

X-ray diffraction carried out as part of this work was performed on a Bruker D-5000 diffractometer equipped with an area detector. The diffractometer utilizes a four-circle goniometer allowing scans to be performed using the 2Θ , ω , X , and ϕ diffraction circles. The

area detector allows simultaneous data collection along the 2Θ and X axes. The Cu anode x-ray source operates at 40 kV and 30 mA. The x-rays are typically collimated to a 0.8 mm diameter beam, providing a resolution of $\sim 0.2^\circ$ in the ω diffraction circle. At the usual substrate-to-detector distance of 15 cm, the area detector collects a range of $\sim 30^\circ$ in 2Θ and X.

Film thickness was characterized *ex situ* by a Dektak step profilometer. For deposition rate measurements, thick films (> 100 nm) were required to obtain reliable measurements. Care was taken in growth experiments to ensure reproducibility of the deposition rate for much thinner films.

Substrate and film topography and roughness was examined using atomic force microscopy. This work utilized a Nanosurf EasyScan 2 AFM operating in dynamic force mode (tapping mode). The AFM uses AppNano ACLA tips with a tip radius of < 10 nm, operating at a resonant frequency between 145 and 230 kHz. A collection rate of 512 pixels per line was used for imaging areas ranging from $1 \mu\text{m} \times 1 \mu\text{m}$, to $8 \mu\text{m} \times 8 \mu\text{m}$.

4.2 Substrate Preparation

The primary substrate utilized in this research is Ga-polar GaN grown via MOCVD by the WideBandGaps Group at North Carolina State University under the instruction of Dr. Zlatko Sitar.⁵ For most experiments, the 3"-diameter substrates were cleaved into quarters for growth and spectroscopic experiments. GaN films were cleaned prior to introduction into the

vacuum system using an HCl/HF etch procedure. The films were placed in a 1:1 H₂O:HCl solution for one minute followed by a deionized water rinse, then into a 50:1 H₂O:HF solution for one minute, and rinsed in water, and dried using compressed nitrogen. This etch procedure is derived from the recipe presented in [6].

The Sitar transfer line utilizes 1.5” Mo pucks for sample holders. Typically, the substrates were fixed to the pucks using Ag paste to encourage good thermal contact, and a Mo clip was used to provide electrical contact to the GaN film. This strategy was effective in mitigating sample charging during XPS experiments to within 1 eV, whereas samples not grounded using a clip often resulted in XPS spectra exhibiting charging of up to 20 eV, due to the insulating sapphire substrates.

4.3 Experimental Details

The data presented in the body of this thesis consists of three types of spectroscopic experiments: growth mode measurements, band offset measurements, and surface reactivity measurements. While each chapter separately discusses the general procedure of each experiment, the purpose of this section is to provide some specificity regarding the details of each investigation.

4.3.1 Growth Mode Measurements

The generalities of the theory underpinning XPS determinations of thin film growth modes were presented in Section 2.3.2. For this thesis, the growth modes of the rocksalt

oxides, MgO and CaO, on GaN substrates were investigated, using the attenuation in intensity of the Ga 2p photoelectron line as the film thickness increased. As shown in Equations 2.7-9, the IMFP of the escaping photoelectrons of interest must be known; it can be calculated from Equation 2.2b, reproduced here as Equation 4.4:

$$\lambda = 2170KE^{-2} + 0.72\sqrt{a \cdot KE}, \quad [4.4]$$

where KE is the kinetic energy of the photoelectrons, and a is the monolayer thickness, in nm. The binding energy of the Ga 2p photoelectron line is ~1117 eV. Thus, according to Equation 2.1, the kinetic energy of Ga 2p photoelectrons is ~366 eV, when using Al $K\alpha$ radiation and a spectrometer work function of 3.94 eV. The monolayer thickness can be estimated by considering the rocksalt structure and taking into account the (111) orientation of the rocksalt films. The length of the body diagonal of a cubic unit cell is given by $c\sqrt{3}$, if c is the lattice constant. Along the (111) direction in rocksalt, there are six alternating layers of anions and cations per unit cell, thus the monolayer thickness can be approximated as $c\sqrt{3}/6$. For MgO ($c = 0.421$ nm), then, the monolayer thickness a is 0.121 nm, and for CaO ($c = 0.481$ nm), a is 0.139 nm. Finally, the IMFP for Ga 2p photoelectrons escaping through an MgO film can be estimated to be 4.8 monolayers, or 0.58 nm. For CaO films, the IMFP is 5.2 monolayers, or 0.72 nm.

4.3.2 Band Offset Measurements

The band offset measurements are well described in the ensuing chapters. One issue that benefits from elaboration, however, is that of charge correction and its relationship to the possibility of varying band discontinuities of films prior to coalescence. In general, charge correction in XPS is carried about by referencing the data to the C 1s photoelectron line originating from adventitious carbon contamination that is found on most samples. In the growth of MgO films, the evolution of the Mg KLL Auger series makes this difficult, as the series has several low-intensity features that reside in the range of the C 1s features (~285 eV). The use of Mg Ka radiation is precluded because the Mg KLL features would shift away from the carbon line, but would then obscure features critical to the band alignment measurement: the shallow core levels Mg 2p and Ga 3d. In the absence of a useful carbon line for charge referencing, the deposition of thin gold films can be used to establish a charging state by examining the Au 4f_{7/2} line, but this precludes any further MgO deposition, a necessary step for the band offset measurement. Thus, it is impossible to know with precision the charging state of the MgO films during the measurement.

While the precise charging state of the oxide films cannot be known, the impact of this problem on the band alignment measurement is secondary. This can be illustrated by considering Equation 2.10, the equation for calculating the valence band offset from XPS measurements (reproduced here as Equation 4.5):

$$\Delta E_V = (E_{CL} - E_{VBM})^{\text{Substrate}} - (E_{CL} - E_{VBM})^{\text{Film}} - \Delta E_B. \quad [4.5]$$

As shown, each term is the difference in binding energy between two features from the same measurement step. In XPS, the assumption of static charging (i.e. that the degree of charging does not vary across the energy scale) is generally taken to be valid. Thus, since each term is simply the energy difference between two features, it is not necessary for those features to be on an absolute (charge-corrected) energy scale. While the measurement of band discontinuities by XPS is not therefore affected by charge referencing, it is important to note that the evaluation of interface band bending (which depends on the comparison of core levels on an absolute scale) is ruled out without adequate charge correction.

In the case of MgO growth on GaN, slow coalescence behavior was observed, as will be discussed in Chapter 5. The second step of XPS measurements (core level measurements on a structure consisting of an electron transparent film on the substrate) is carried out at thicknesses at which the MgO is not fully coalesced. Thus, the possibility of varying band lineup as a function of film coverage presented itself. Typically, such a possibility could be investigated by tracking the chemical shift of the substrate core levels. This is not straightforward if the charging state is not precisely known. In this situation, the Auger parameter is a useful tool for evaluating chemical states. The Auger parameter is simply the distance (in binding energy) between a core level and a particular Auger feature, which changes systematically as chemical states change. In this investigation, the Auger parameter was used, as the difference in binding energy between the Ga 3d photoelectron line and the $L_2M_{45}M_{45}$ Auger transition, to evaluate chemical shifts in the GaN substrate as MgO coalescence proceeded.

REFERENCES

- ¹ D. L. Smith, *Thin-Film Deposition: Principles & Practice* (McGraw Hill, New York, 1995).
- ² H. S. Craft, J. F. Ihlefeld, M. D. Losego, R. Collazo, Z. Sitar, and J. P. Maria, *Applied Physics Letters* **88**, 212906 (2006).
- ³ M. D. Losego, Thesis, North Carolina State University, 2008.
- ⁴ M. D. Losego, S. Mita, R. Collazo, Z. Sitar, and J. P. Maria, *Journal of Vacuum Science & Technology B* **25**, 1029-1032 (2007).
- ⁵ R. Collazo, S. Mita, A. Aleksov, R. Schlessner, and Z. Sitar, *Journal of Crystal Growth* **287**, 586-590 (2006).
- ⁶ S. W. King, J. P. Barnak, M. D. Bremser, K. M. Tracy, C. Ronning, R. F. Davis, and R. J. Nemanich, *Journal of Applied Physics* **84**, 5248-5260 (1998).

5. Band offsets and growth mode of MBE-grown MgO (111) on GaN (0002) by X-ray photoelectron spectroscopy

H.S. Craft, R. Collazo, M.D. Losego, S. Mita, Z. Sitar, and J.-P. Maria

Published in Journal of Applied Physics: **102**, 074104 (2007).

Band offsets and growth mode of MBE-grown MgO (111) on GaN (0002) by X-ray photoelectron spectroscopy

H.S. Craft, R. Collazo, M.D. Losego, S. Mita, Z. Sitar, and J.-P. Maria

Department of Materials Science and Engineering, Raleigh, NC 27603

Abstract

MgO is a proposed dielectric for use as a tunneling barrier in devices integrating GaN and ferroelectric oxides. In this study, we present data regarding the growth mode and band offsets of MgO grown epitaxially on GaN (0002) surfaces using molecular beam epitaxy. Using in-situ x-ray photoelectron spectroscopy (XPS) and molecular beam epitaxy (MBE), we determine, from sequential growth experiments, that the growth of MgO proceeds via the Volmer-Weber (3-dimensional) mode and full coalescence of the film does not occur until approximately 12 nm of MgO have been deposited. The observation of a 3-D growth mode is in agreement with previously published data. For the valence band offset, we find a value of 1.2 ± 0.2 eV, which corresponds to a 3.2 eV conduction band offset. XPS measurements suggest a chemically abrupt interface and no effect on band lineup due to the slow coalescence behavior.

Introduction

GaN-based semiconductor devices are of interest for high-power, high-frequency operation at elevated temperatures. As in the case with silicon, significant effort has been expended to find suitable oxides to use as passive and active dielectrics. Among such structures, the use of ferroelectric gates in III-nitride heterostructures has attracted attention¹⁻⁴ for nonvolatile memory applications as well as the possibility of exploiting the interaction between a ferroelectric's switchable polarization and the heterostructure 2-D electron gas. There are several difficulties associated with such structures; one is the likelihood of insufficient band offsets between GaN and ferroelectrics. This situation would lead to unacceptable tunneling currents through a thin oxide and overall diminished device performance. Recently, Tian *et al* demonstrated integration of BiFeO₃ with GaN using a TiO₂ buffer layer.⁵ MgO is another candidate for use as a buffer layer in such devices to inhibit chemical reactions and mitigate tunneling current, as it has a wide bandgap (7.8 eV), acceptable lattice matching to GaN (0002), and thermal stability in contact with GaN.⁶ This interface, however, is not well studied in terms of growth behavior and band lineup. One previous measurement reports a valence band offset of 1.1 eV,⁷ and Robertson and Falabretti predict a value of 2.0 eV.⁸ Here we present a study using x-ray photoelectron spectroscopy (XPS) of the growth mode of MgO on GaN (0002) and experimentally measured band offsets.

Experimental Procedure

MgO films were grown on Ga-polar, n-type GaN (0002) substrates grown by metalorganic chemical vapor deposition on sapphire.⁹ The MgO was grown via MBE as previously described.⁶ The base pressure of the growth chamber was 2.0×10^{-8} torr. The GaN substrates were Si-doped to provide carrier concentrations ranging from 2.0×10^{18} cm^{-3} to 5.6×10^{18} cm^{-3} as determined by Hall measurements. Specific deposition conditions consist of a substrate temperature of 250 °C as measured using an infrared pyrometer aimed at the side of a molybdenum sample holder to which the substrates were mechanically clamped, a growth pressure of 1×10^{-6} torr molecular oxygen, and an effusion cell temperature of 400 °C. The growth rate, measured using step profilometry, was 1.5 nm/min. Samples were transferred under UHV conditions (base pressure of 1×10^{-9} torr in the transfer line) to the surface analysis chamber, in which all spectra were measured. Prior to any measurement or film growth, the substrate was subjected to an offgassing anneal at 400 °C in a chamber with a base pressure of 1×10^{-9} torr. Measurement of XPS spectra was carried out using a dual anode source and a VG concentric hemispherical analyzer, operating in the constant pass energy mode. Unless otherwise noted, measurements were carried out using Al K α radiation (1486.6 eV), and a pass energy of 20 eV. The base pressure of the surface analysis chamber was $<1.0 \times 10^{-10}$ torr.

Measurement of band offsets using XPS was performed according to the procedure described by Waldrop and Grant for AlGa N /Ga N heterostructures.¹⁰ The band offset of MgO on Ga N is measured by assessing data sequentially from the substrate Ga N , a thin (<10 nm,

so as to be transparent to escaping photoelectrons) film of MgO on GaN, and finally a thick ($\gg 10$ nm) film of MgO on GaN. A more detailed discussion is given in Section III. The positions of photoelectric lines were established using Igor Pro analysis software and Voigt peak shapes with the same peak width. Valence band maxima were determined using the linear intercept technique, in which linear fits are applied to the leading edge of the valence band, and to the flat background signal. Adventitious hydrocarbons allowed for charge correction of the bare GaN surface prior to MgO deposition. For this work, we take the position of the C 1s photoelectric line to be 284.6 eV. For subsequent measurement stages, the use of adventitious carbon is not straightforward, due to the overlap of the C 1s peak with low intensity features related to the Mg KLL Auger series, whose primary features begin at 301 eV. This overlap introduces difficulties in data interpretation, but does not affect band offset calculations, as will be discussed below. Here, for the purposes of charge referencing, we assume the charging state of a thin (< 10 nm) MgO film to be approximately equal to that of a bare GaN surface. Charge assessment for the final measurement was performed by *in-situ* e-beam evaporation of a 5 nm Au film onto the sample, from which the position of the Au $4f_{7/2}$ peak could be measured and referenced to 84.0 eV.

Results and Discussion

Characterization of MgO Growth Mode

As suggested previously by reflection high-energy electron diffraction (RHEED) and atomic force microscopy (AFM), the growth of MgO on GaN (0002) surfaces is three-dimensional in nature.⁶ This suggests possible complications for measuring band offsets, as the standard method for determining band offsets via XPS assumes 2-D growth, or full coverage of the substrate by the film at thicknesses greater than one monolayer. Specifically, the presence of a 3-D growth mode implies that in the thickness regime necessary for band offset measurements (<10 nm), the substrate GaN signal in an XPS measurement may be detected in more than one bonding environment (i.e., GaN bonded to MgO, and the GaN free surface), thus introducing an additional subtlety into the interpretation. Potentially, this may affect the band lineup as a function of film thickness. Before proceeding with band offset measurements, we first explore this behavior.

By tracking the attenuation of the substrate signal from a given photoelectric peak, the growth of an overlayer can be traced *in-situ*. In this study, successive 1 nm layers of MgO were grown on a GaN (0002) substrate, and the integrated intensity of the Ga 2p_{3/2} peak was recorded as a function of the film thickness. This data can be compared to theoretical predictions of intensity attenuation for the three relevant growth modes: Frank-van der Merwe (2-D growth), Volmer-Weber (3-D growth), and Stranski-Krastanov (3-D growth on an initial 2-D overlayer of the film). Following the treatment of Sitar *et al*,¹¹ the original

intensity I_o from the substrate film interface is attenuated, in 2-D growth, to the intensity I_s at the film surface:

$$\frac{I_s}{I_o} = e^{-\frac{t}{\lambda}}, \quad [5.1]$$

Where t is the film thickness and l is the escape depth of the electrons of interest, which we take here as 0.65 nm as calculated from the inelastic mean free path.¹² For Volmer-Weber (3-D) growth, the relation is of the form:

$$\frac{I_s}{I_o} = (1 - \Theta) + \Theta e^{-\frac{t}{\lambda}} \quad [5.2]$$

Here, Q is the extent of film coverage over the substrate. The attenuation in this case is effectively linear. Finally, for the case of Stranski-Krastanov growth, the attenuation follows:

$$\frac{I_s}{I_o} = (1 - \Theta) e^{-\frac{a}{\lambda}} + \Theta e^{-\frac{t}{\lambda}} \quad [5.3]$$

Where a is one monolayer thickness. The substrate peak decreases in intensity exponentially as the first 2-D coverage layer is formed, after which the attenuation is again linear as coverage increases.

Figure 1 shows the results of this analysis, plotted with the integrated intensity of the Ga 2p peak (normalized to the initial substrate intensity), as a function of MgO thickness. The data, roughly following the Volmer-Weber prediction, indicates 3-D growth, as expected from the previously mentioned RHEED and AFM data. Assuming the predicted Ga 2p peak intensity represents a coalesced film, this data suggests that the 3-D MgO islands do not fully coalesce until the film thickness is above ~12 nm. This behavior provides a large window of

possible thicknesses over which to investigate the band offsets as a function of film coverage, but also provides an important guideline when considering device structures that require continuous insulating layers.

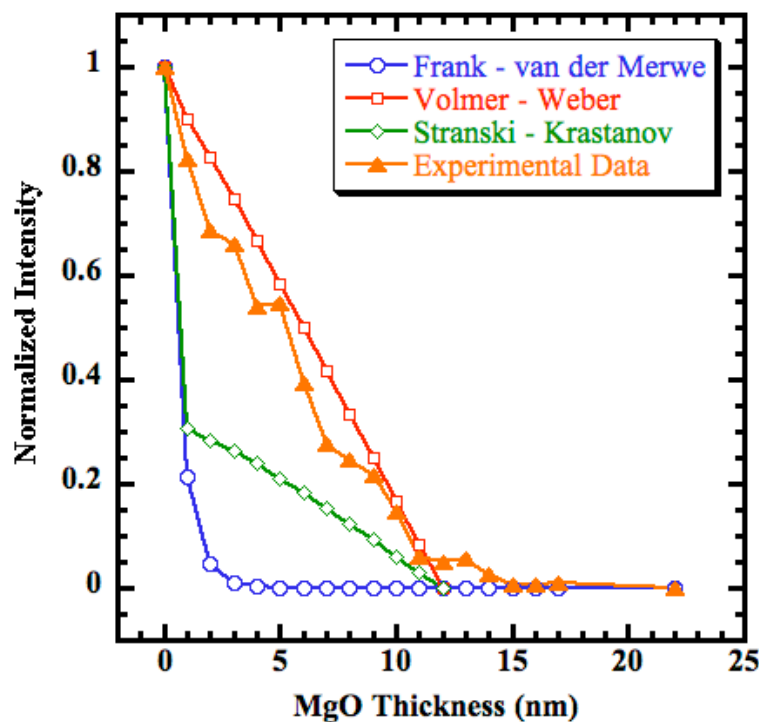


Figure 5.1: Comparison of integrated intensity of Ga 2p photoelectric peak with theoretical predictions as MgO thickness increases

Band Offset Measurements

The determination of the valence band offset in the MgO/GaN system involves the precise determination and comparison of relevant core levels and valence band maxima of the materials in question, both separately and in combination. In this case, the use of the Ga

3d core level in GaN, and the Mg 2p peak in MgO, is appropriate to the measurement.

Therefore, the band offset may be determined through the relation

$$\Delta E_v = \left(\text{Ga}_{3d} - \text{GaN}_{\text{VBM}} \right)_{\text{GaN}} - \left(\text{Ga}_{3d} - \text{Mg}_{2p} \right)_{\text{MgO/GaN}} - \left(\text{Mg}_{2p} - \text{MgO}_{\text{VBM}} \right)_{\text{MgO}} \quad [5.4]$$

When the equation is presented in this manner, it worthwhile to recognize that since each of the three principle terms is dependent only on the energy difference between two features, it is not necessary to measure the precise charging state at each step, unless exact information regarding band bending is also desired. Here we assume that the charging state of the GaN substrate is equal to that of the MgO overlayer.

Having established the coalescence behavior of MgO on GaN and determined a relevant range of thicknesses over which variation in band lineup is possible, we now present three measurements of the valence band offset in this system. In order to assess the issue of thickness and coalescence behavior, we chose thicknesses of 4, 7, and 10 nm MgO as the intermediate measurement steps. Selected data from the 7 nm sample is shown in Figure 2: the measurements of the Ga 3d core level and GaN valence band are from the bare substrate signal, and the Mg 2p core level and MgO valence band are from the final step in the measurement - approximately 40 nm MgO. Both core level peaks consistently feature a primary peak (from which the binding energies were determined) and a low intensity secondary peak located 0.8 – 0.9 eV higher in binding energy. In the case of the Mg 2p feature, the secondary peak is typically attributed to Mg-OH bonding, which is consistent with our observation that this feature grows in intensity relative to the primary peak upon

atmospheric exposure. The secondary feature of the Ga 3d peak is often attributed to Ga-O bonding in the open literature, however we note that subsequent to offgassing, survey scans (not shown) of the GaN substrate using Al Ka radiation do not show any indication of the O KLL Auger series, and scans using Mg Ka radiation reveal no features in the expected region of the O 1s photoelectric line. Given the invariant nature of the separation and intensity ratio of these peaks subsequent to processing steps and surface treatments, we take this peak shape as simply the shape of this photoelectric line in GaN; any further analysis of the origin of this feature is beyond the scope of the work presented here.

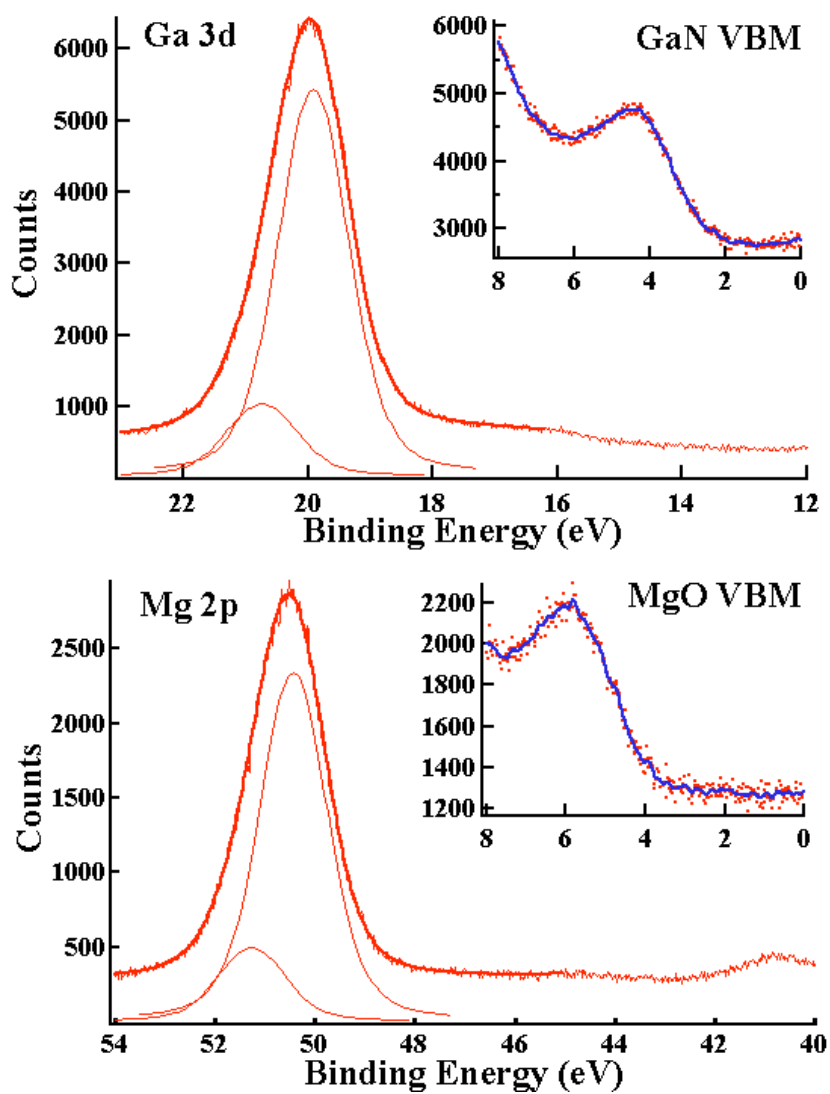


Figure 5.2: Representative XPS data showing Ga 3d and Mg 2p core levels, and the corresponding valence band regions (insets)

The results of the three measurements are summarized in Table I, which gives the values of the three terms of Equation 4, as well as the average value for the three measurements of each feature of interest. We note that the binding energy of the Ga 3d peak

as MgO coverage varies is consistent to ± 0.14 eV, and furthermore that the variation from sample to sample was not systematic. A systematic trend would be expected in the case of an MgO thickness effect, and would be manifest as a chemical shift of the GaN-related photoelectric lines. In the absence of an absolute charging reference, the relative peak positions can be used to assess chemical shifts. The position of the Ga 3d peak with respect to the N 1s peak is consistent to within 0.08 eV.* Therefore, in this case, the variation in binding energy is due to the uncertainty in the charging state during the “thin MgO” step, and does not suggest a chemical shift. This invariance indicates that the slow coalescence behavior of MgO on GaN does not affect band lineup.

* Note: The corrected discussion of this procedure is presented in Chapter Four, as the determination of the Ga 3d – Ga L₂M₄₅M₄₅ Auger parameter.

Table 5.1: Summary of XPS data used for valence band offset calculations. All values given are in eV.

	Bare GaN		40 nm MgO		Thin MgO		DE_v
	$Ga_{3d} - GaN_{VBM}$		$Mg_{2p} - MgO_{VBM}$		$Ga_{3d} - Mg_{2p}$		
4 nm	17.6		46.8		-30.60		1.4
7 nm	17.6		47.0		-30.53		1.1
10 nm	17.6		46.5		-30.09		1.2
	Ga 3d	GaN VBM	Mg 2p	MgO VBM	Ga 3d	Mg 2p	DE_v
Average	20.11	2.5	50.29	3.5	19.78	50.1	1.2
±	0.08	0.1	0.66	0.4	0.14	0.17	0.14

Since we find no evidence, within experimental error, for a coverage effect in band lineup measurements, a valence band offset value of 1.2 eV is presented as the average of the three aforementioned measurements. Using a bandgap of 7.8 eV for MgO and 3.4 eV for GaN, this yields a conduction band offset of 3.2 eV. These values are sufficient for MgO to act as a tunneling barrier on GaN. As shown in Table 1, the spread in the measurements shown is principally due to a significant dispersion in the measured position of the Mg 2p

peak relative to other features of interest, primarily in the measurements on 40 nm MgO. This leads to a maximum error of 0.4 eV in the measurement. The more commonly reported standard deviation of the measurements is 0.14 eV, which is smaller than the maximum error of the curve fitting, which is 0.2 eV due to the poor resolution and signal to noise ratio in the valence band region. Our valence band offset value of 1.2 ± 0.2 eV compares with a previously measured value of 1.1 eV,⁷ and a calculated figure of 2.0 eV,⁸ The calculated figure, determined using the charge neutrality level technique, is based on the difference in average electronegativity between GaN and MgO, and does not consider interfacial bonding configurations and polarity effects. In Figure 3, a simplified band diagram of this interface is presented. Again referring to Table 1, the band bending can be deduced. However, since the charging state of the spectra taken of the intermediate thickness step is not explicitly known, and can be expected to be of the same order of magnitude as the band bending, a quantitative determination of the band bending is not appropriate. We note only that there appears to be slight upward bending in the GaN, and slight downward bending in the MgO.

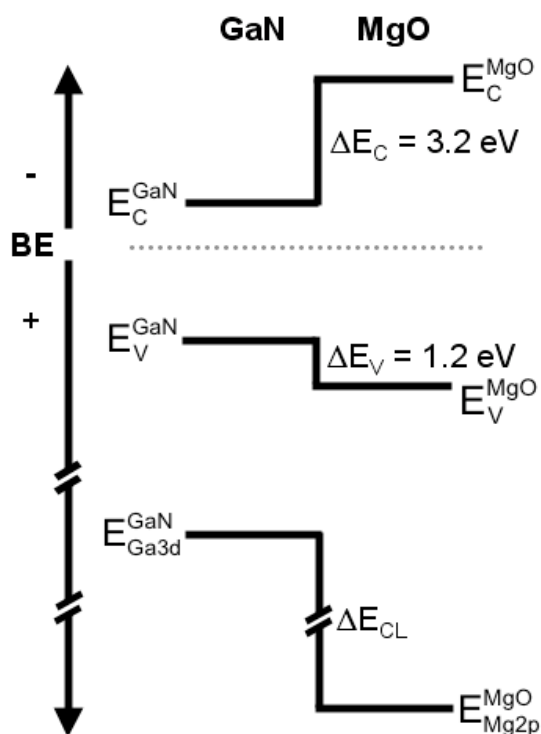


Figure 5.3: Simplified band diagram of MgO/GaN interface

Conclusion

We present a study of the growth behavior and band lineup up of MgO (111) on GaN (0002) by XPS. In agreement with previously published findings, the growth of MgO on GaN proceeds in the Volmer-Weber (3-D) mode. XPS data suggests that the film does not fully coalesce on the substrate until approximately 12 nm of MgO have been deposited on GaN. According to our findings, this behavior does not influence the band offsets, which we find to be $1.2 \pm 0.2 \text{ eV}$ for the valence band, and $3.2 \pm 0.2 \text{ eV}$ for the conduction band. These

values are sufficient to act as tunneling barriers in devices; however, the coalescence behavior should be taken into account in these structures.

Acknowledgements

H.S.C, M.D.L., and J.P.M. gratefully acknowledge the support of the Office of Naval Research under the Epitaxial Multifunctional Materials and Applications MURI (2004-0779).

M.D.L is supported by a National Science Foundation Graduate Research Fellowship.

REFERENCES

- ¹ S. K. Dey, W. Cao, S. Bhaskar, and J. Li, *Journal of Materials Research* **21**, 1526-1531 (2006).
- ² I. Stolichnov, L. Malin, P. Muralt, and N. Setter, *Applied Physics Letters* **88**, (2006).
- ³ A. Gruverman, W. Cao, S. Bhaskar, and S. K. Dey, *Applied Physics Letters* **84**, 5153-5155 (2004).
- ⁴ H. T. Xu, N. K. Pervez, P. J. Hansen, L. K. Shen, S. Keller, U. K. Mishra, and R. A. York, *IEEE Electron Device Letters* **25**, 49-51 (2004).
- ⁵ W. Tian, V. Vaithyanathan, D. G. Schlom, Q. Zhan, S. Y. Yang, Y. H. Chu, and R. Ramesh, *Applied Physics Letters* **90** (2007).
- ⁶ H. S. Craft, J. F. Ihlefeld, M. D. Losego, R. Collazo, Z. Sitar, and J. P. Maria, *Applied Physics Letters* **88**, 212906 (2006).
- ⁷ J. J. Chen, B. P. Gila, M. Hlad, A. Gerger, F. Ren, C. R. Abernathy, and S. J. Pearton, *Applied Physics Letters* **88**, (2006).
- ⁸ J. Robertson and B. Falabretti, *Journal of Applied Physics* **100**, (2006).
- ⁹ R. Collazo, S. Mita, A. Aleksov, R. Schlessler, and Z. Sitar, *Journal of Crystal Growth* **287**, 586-590 (2006).
- ¹⁰ J. R. Waldrop and R. W. Grant, *Applied Physics Letters* **68**, 2879-2881 (1996).
- ¹¹ Z. Sitar, L. L. Smith, and R. F. Davis, *Journal of Crystal Growth* **141**, 11-21 (1994).
- ¹² M. P. Seah and W. A. Dench, *Surface and Interface Analysis* **1**, 2-11 (1979).

6. Spectroscopic analysis of the epitaxial CaO (111) - GaN (0002) interface

H.S. Craft, R. Collazo, M.D. Losego, S. Mita, Z. Sitar, and J-P. Maria

Published in Applied Physics Letters: **92**, 082907 (2008).

Spectroscopic analysis of the epitaxial CaO (111) - GaN (0002) interface

H.S. Craft, R. Collazo, M.D. Losego, S. Mita, Z. Sitar, and J-P. Maria

Department of Materials Science and Engineering, North Carolina State University, Raleigh,
NC 27603

Abstract

We report an XPS (x-ray photoelectron spectroscopy) study of the CaO/GaN interface. Epitaxial films of CaO (111) were grown on GaN (0002) and analyzed *in-situ* using XPS. We observe Stranski-Krastanov growth, in which CaO coalesces rapidly, then converts to a 3-dimensional mode. Data suggests coalescence within the first nm of film growth, indicating growth behavior different from published reports of the analogous MgO-GaN system. We find 1.0 ± 0.2 eV for the valence band offset, and a 2.5 ± 0.2 eV conduction band offset. The results are discussed in terms of their utility in oxide - nitride electronic devices.

Introduction

The integration of GaN with passive and active oxides is of interest for designing high-frequency, high-power devices. In the case of “active” oxides, we refer to crystalline oxides with a permanent and reorientable dielectric polarization that can be coupled to the polar c-axis of GaN. In 2003 it was proposed¹ that integration of such structures could provide a polarization discontinuity at the GaN/Ferroelectric interface that induces a large charge density in the GaN, and furthermore, that the charge could be modulated by taking advantage of the reorientable polarization of a ferroelectric and its susceptibility to changes in temperature and mechanical strain. These devices remain in the very early stages of development, and interest in the technology remains high. An anticipated challenge with such structures is the similar band gaps of GaN and most ferroelectric perovskites, leading to small band offsets and large tunneling currents. As such, the use of epitaxial wide-band gap buffer layers as tunneling barriers has attracted attention. The rocksalt oxides are candidates for such an application. Epitaxial growth of MgO,² CaO,³ as well as $\text{Ca}_x\text{Mg}_{1-x}\text{O}$,⁴ on GaN have been previously reported. In the case of the $\text{Ca}_x\text{Mg}_{1-x}\text{O}$ alloy, the authors report a valence band offset of 0.65 ± 0.1 eV. In addition, the present authors recently reported on the band alignment and growth mode of MgO on GaN.⁵ Here we present an analogous interfacial study of the CaO/GaN system.

CaO films were grown on Ga-polar, n-type GaN (0002) templates grown on sapphire by hydrogenless metalorganic chemical vapor deposition on sapphire.^{6,7} The GaN was Si-doped to an n-type carrier concentration of 1.2×10^{18} /cm³. Prior to growth, the GaN surface

was cleaned by a 1:1 H₂O:HCl etch, followed by a 99:1 H₂O:HF etch. Once loaded into vacuum, the substrates were outgassed at approximately 400°C for 1 hour. The CaO films were grown epitaxially as described by Losego *et al.*³ Specific growth conditions for this work consisted of a growth temperature of 500 °C as measured by an infrared pyrometer, an effusion cell temperature of 510 °C, from which metallic Ca (Alfa Aesar, 99.9% purity) was evaporated into an molecular oxygen background pressure of 1x10⁻⁶ Torr, supplied through a variable leak valve. The growth chamber base pressure was 1.0x10⁻⁹ Torr. The growth rate, as measured by step profilometry, was 0.8 nm/min. Immediately after growth, the samples were transferred under UHV conditions (~1x10⁻⁹ Torr) to the surface analysis chamber, where they were stored for the duration of the experiments, under a base pressure of <1.0x10⁻¹⁰ Torr.

The XPS experiments were performed as previously described.^{5,7,8} All experiments utilized Al K α radiation (1486.6 eV), with the spectrometer operating at a pass energy of 20 eV. The positions of photoelectric lines were established using the Igor Pro analysis package, and Voigt peak shapes with an equal peak width constraint. Valence band maxima were determined by the linear intercept technique, in which fits are applied to the leading edge of the valence band, and to the background signal in the band gap region. Adventitious hydrocarbons allowed for charge correction of the bare GaN surface prior to CaO deposition. For this work, we take the position of the C 1s photoelectron line to be 284.6 eV. During the growth mode experiments, 0.5 nm layers of CaO were grown consecutively over the GaN substrate, and the decay in the intensity of the Ga 2p photoelectron line was recorded. Band

offset measurements can be performed concomitantly to these experiments, in the manner outlined by Waldrop and Grant for AlGaIn/GaN heterostructures.⁹ For this work, we take the Ga 3d and Ca 3p photoelectron lines as the core levels relevant to the measurement, so the expression for the valence band offset becomes

$$\Delta E_V = (E_{\text{Ga3d}} - E_{\text{VBM}})^{\text{BareGaN}} - (E_{\text{Ca3p}} - E_{\text{VBM}})^{\text{CaO}} - (E_{\text{Ga3d}} - E_{\text{Ca3p}})^{\text{CaO/GaN}}, \quad [6.1]$$

where the first term refers to measurements taken from the GaN substrate, the second term to measurements taken from thick (approximately 40 nm, so as to be opaque to photoelectrons originating from within the GaN substrate) CaO, and the final term refers to measurements on a thin (< 10 nm) film of CaO on GaN. During the CaO growth, the charging state was assumed to be equal to that of the GaN substrate. Charge assessment for the final measurement step was performed by *in-situ* e-beam evaporation of a 5 nm Au film onto the sample, from which the position of the Au 4f_{7/2} peak could be measured and referenced to 84.0 eV.

Results and Discussion

In Figure 1, we show the decay in the integrated intensity of the Ga 2p photoelectron line (normalized to the original intensity) as CaO growth proceeds. For clarity, the data is plotted only against the prediction of the case of two-dimensional (Frank – van der Merwe) growth, in which the intensity I_s at the sample surface decays exponentially from the original intensity I_0 :

$$\frac{I_s}{I_o} = e^{-t/\lambda}. \quad [6.2]$$

Here, t is the film thickness (nm), and λ is the photoelectron mean free path (nm). This data is distinctly different from the previously published XPS investigation of MgO growth on GaN, in which a slowly coalescing, three-dimensional film morphology is obvious, and full coalescence does not occur until the thickness increases beyond 10 nm.⁵

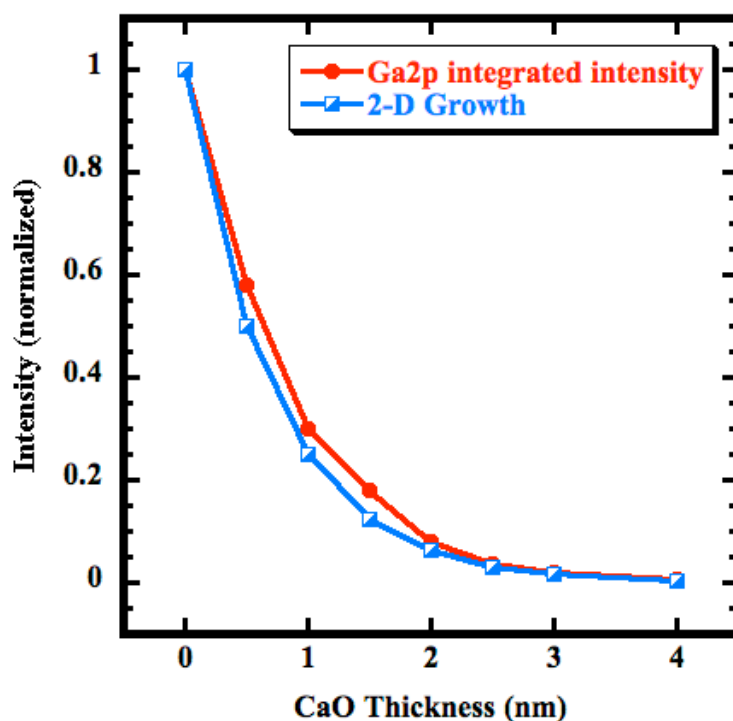


Figure 6.1: Comparison of Ga 2p integrated intensity as CaO thickness increases with prediction for two-dimensional film growth.

The present data suggests 2-D growth of CaO on GaN, and RHEED data collected at the very early stages of growth corroborates this interpretation. However, RHEED data unambiguously shows roughening and a transition to three dimensional (Volmer – Weber)

growth at higher thicknesses.³ In comparison, an initial phase of 2-D growth is difficult to identify for the MgO-GaN system. A Stranski-Krastanov growth mode for CaO on GaN is proposed in which an initial 2-D, (111) oriented film nucleates, followed by rapidly-coalescing 3-D islands. The morphology change is driven by the overall free energy reduction associated with (100) faceting which eliminates the accumulation of the electrostatic potential associated with the polar nature of {111} rocksalt surfaces. Theoretical predictions suggest that the (001) surface has a ~5X lower energy density compared to (111).^{10,11}

Given the constraints of our experiment, in which a quartz crystal rate monitor (for precise deposition at very small thicknesses) was not available, a clear distinction between the two growth modes is difficult. Within the limits afforded by the data density in Figure 1, we can speculate that the CaO coalesces within the first nanometer of growth, after which the attenuation of the substrate signal is exponential, as would be expected for a nonporous overlayer. This implies that the minimum thickness for an electrically continuous CaO buffer layer is significantly less than the thickness required for an MgO layer. In principle, an effective buffer layer between a polar oxide and GaN could be established, using CaO, using a film on the order of 2 nm. We illustrate the difference in MgO and CaO behavior, schematically, in Figure 2, to point out the possible advantage from the standpoint of device design of thin CaO buffer layers with respect to MgO buffer layers. A more rapidly coalescing CaO film, in which the film nuclei coarsen as they increase in thickness (in contrast to the behavior seen with MgO films), suggests also that CaO films may have

decreased roughness as compared to MgO films. Given the propensity of CaO to rapidly hydroxylate through the bulk of the film upon atmospheric exposure,³ we were unable to address this possibility experimentally.

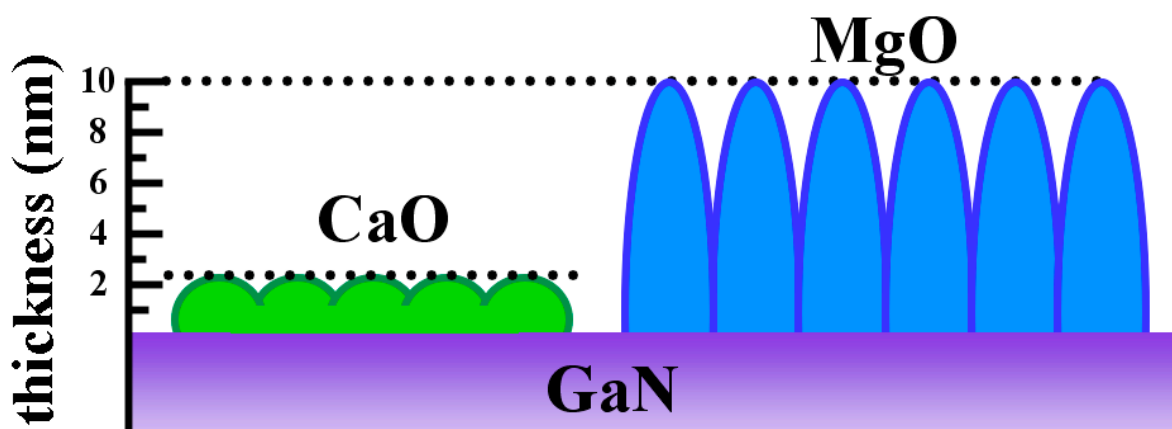


Figure 6.2: Schematic illustration of the relative coalescence behaviors of CaO and MgO on GaN (0002).

Since we observe rapid coalescence of CaO on GaN, the band offset measurement is straightforward (i.e., there is no concern for varying band alignment as coalescence proceeds). Thus, with the collection of valence band spectra of GaN (at the beginning of the growth mode experiment) and CaO (after a thick (40 nm) film had been grown), a series of band offset measurements was performed in parallel to the growth mode experiment. In this experiment, the value of the third term in Equation 1 was continually reevaluated as the CaO film grew in thickness. Representative data from the core level and valence band measurements is shown in Figure 3. No meaningful variation in peak width, shape, or

position was noted in the core level spectra shown in Figure 3 as the growth of CaO continued.

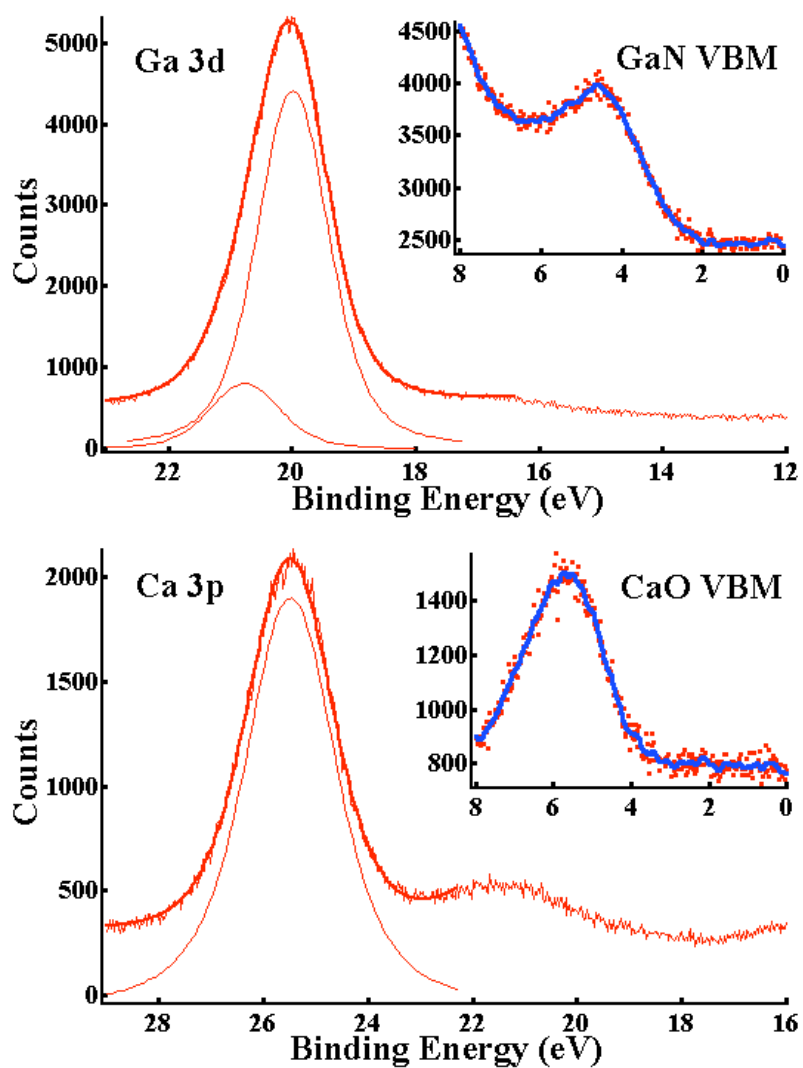


Figure 6.3: Sample spectra showing Ga 3d and Ca 3p core levels as well as valence band spectra from bare GaN and 40 nm CaO, respectively.

The measurements are summarized in Figure 4, which shows a simplified band diagram of the CaO/GaN interface, as well as relevant energy values for the spectral features

at each measurement stage. As shown in Figure 4, we calculate the valence band offset for CaO on GaN to be 1.0 eV, with a maximum error of ± 0.2 eV, which we obtain from the error in the curve fitting of the valence band regions. Using a value for the CaO band gap of 6.9 eV,¹² and 3.4 eV for GaN, we can therefore calculate a conduction band offset of 2.5 ± 0.2 eV. We also note that there appears to be slight upward band bending in the GaN as a result of the CaO film, however our uncertainty in charging assessment precludes a quantitative analysis.

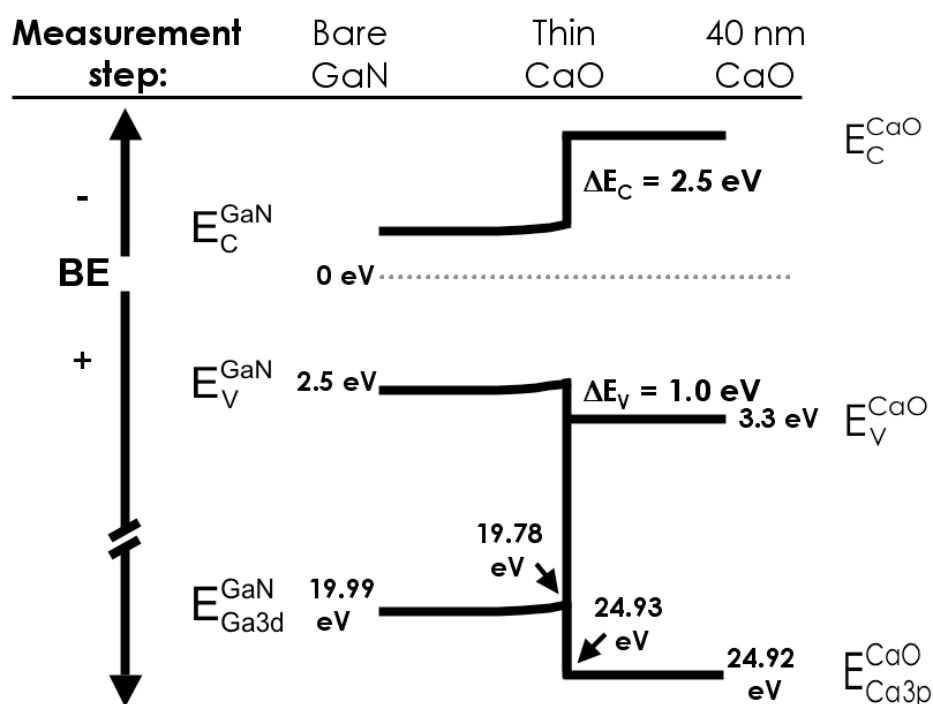


Figure 6.4: Simplified band diagram of the CaO/GaN interface.

Conclusion

In conclusion, data regarding the growth mode and band offset of CaO films grown via MBE on Ga-polar GaN are presented. The growth of CaO on GaN proceeds through a three-dimensional mode, and the substrate peak attenuation suggests coalescence of these films within the first nanometer of growth. This is in direct contrast to the case of MgO on GaN, in which full coalescence occurs after a thickness of 10 nm. As a result, CaO may be more promising in terms of the electrical behavior of very thin films on GaN. The band offsets of CaO on GaN are 1.0 ± 0.2 eV at the valence band, and 2.5 ± 0.2 eV at the conduction band. These values further suggest the suitability of CaO as a buffer layer or passivation layer in III-V devices. However, questions remain regarding the phase stability of CaO against water uptake and hydroxylation. Further study in this area will be necessary to assess the extent of this issue.

Acknowledgements

H.S.C, M.D.L., and J-P.M. gratefully acknowledge the support of the Office of Naval Research under the Epitaxial Multifunctional Materials and Applications MURI (2004-0779) sponsored by Dr. Colin Wood and managed by Professor Alan Doolittle.

REFERENCES

- ¹ M. Singh, Y. R. Wu, and J. Singh, *Solid-State Electronics* **47**, 2155-2159 (2003).
- ² H. S. Craft, J. F. Ihlefeld, M. D. Losego, R. Collazo, Z. Sitar, and J. P. Maria, *Applied Physics Letters* **88**, 212906 (2006).
- ³ M. D. Losego, S. Mita, R. Collazo, Z. Sitar, and J. P. Maria, *Journal of Vacuum Science & Technology B* **25**, 1029-1032 (2007).
- ⁴ J. J. Chen, M. Hlad, A. P. Gerger, B. P. Gila, F. Ren, C. R. Abernathy, and S. J. Pearton, *Journal of Electronic Materials* **36**, 368-372 (2007).
- ⁵ H. S. Craft, R. Collazo, M. D. Losego, S. Mita, Z. Sitar, and J. P. Maria, *Journal of Applied Physics* **102**, 074104 (2007).
- ⁶ R. Collazo, S. Mita, A. Aleksov, R. Schlessner, and Z. Sitar, *Journal of Crystal Growth* **287**, 586-590 (2006).
- ⁷ R. Collazo, S. Mita, A. Rice, R. F. Dalmau, and Z. Sitar, *Applied Physics Letters* **91**, 212103 (2007).
- ⁸ Z. Sitar, L. L. Smith, and R. F. Davis, *Journal of Crystal Growth* **141**, 11-21 (1994).
- ⁹ J. R. Waldrop and R. W. Grant, *Applied Physics Letters* **68**, 2879-2881 (1996).
- ¹⁰ P. L. Gutshall and G. E. Gross, *Journal of Applied Physics* **36**, 2459 (1965).
- ¹¹ C. Noguera, *Journal of Physics-Condensed Matter* **12**, R367-R410 (2000).
- ¹² D. P. Norton, *Materials Science & Engineering R-Reports* **43**, 139-247 (2004).

7. Surface water reactivity of polycrystalline MgO and CaO films investigated using x-ray photoelectron spectroscopy

H.S. Craft, R. Collazo, M.D. Losego, Z. Sitar, and J-P. Maria

Published in Journal of Vacuum Science and Technology A: 26(6) 1507 (2008).

Surface water reactivity of polycrystalline MgO and CaO films investigated using x-ray photoelectron spectroscopy

H.S. Craft^(a), R. Collazo, M.D. Losego, Z. Sitar, and J-P. Maria

Department of Materials Science and Engineering, North Carolina State University, Raleigh NC 27606

Abstract

We report a study comparing the surface reactivities of the alkaline earth oxides MgO and CaO with respect to water vapor under ultra-high and high vacuum conditions. Using x-ray photoelectron spectroscopy and a series of *in-vacuo* exposures spanning $\sim 10^{-10}$ Torr vacuum, to 10^{-6} Torr flowing oxygen, the extent of surface hydroxylation was investigated by monitoring the O 1s photoelectron line. After the most aggressive exposures, the MgO surface reacted to form a maximum hydroxyl coverage of ~ 1.3 ML, while the CaO surface reached a maximum coverage of ~ 3.0 ML. Both surface hydroxides could be removed by *in vacuo* thermal anneals; exposure to 250 °C and 500 °C were required for MgO and CaO respectively. These results are framed in terms of the suitability of these oxides in complex oxide-compound semiconductor heteroepitaxial multifunctional devices and with respect to understanding the development of surface morphology in epitaxial 111-oriented CaO and MgO thin films.

Introduction

The rocksalt oxides MgO and CaO are currently under study as buffer layers in devices integrating compound semiconductors (i.e. GaN and SiC) with functional oxides (i.e. perovskite ferroelectrics). In such devices, the polarization discontinuity between the semiconductor and the polar oxide induces a large charge density at the interface, which can be modulated through the oxide's ferroelectric, piezoelectric, or pyroelectric effect. The purpose of the rocksalt buffer layers in the proposed device structures is to mitigate tunneling current losses, as GaN has a similar bandgap (3.4 eV) to most ferroelectric perovskites of interest (3-3.5 eV). Recently, our group has measured the band offsets and growth behavior of epitaxial films of MgO (111)¹ and CaO (111)² on GaN, and found them to be good candidates for use as tunneling barriers in such structures. A remaining issue is the reactivity of such compounds with atmospheric exposure, a known problem in alkaline earth oxides. Exposure to environments other than vacuum are invariably required for subsequent preparation of complex oxides, and potentially required during transfers between non-clustered deposition tools. Quantitatively understanding the behavior of these surfaces is a required step in identifying interface regulated properties and developing guidelines for device preparation.

Because of its use in catalytic applications, the reactivity of MgO with atmospheric gases has been extensively studied. For example, synchrotron x-ray photoelectron spectroscopy (XPS) studies of single crystal MgO (100) surfaces show a time-independent reaction with water at low exposure pressures ($< 3 \times 10^{-5}$ Torr) that occurs at surface defect

sites, followed by a reaction at increased pressures ($> 10^{-4}$ Torr) involving terrace sites.³ Further study by the same group of defective (100) surfaces found defect-enhanced reactivity at all exposure pressures down to $\sim 10^{-10}$ Torr,⁴ which agrees with earlier work investigating MgO smoke cubes⁵ and Auger electron spectroscopy of MgO single crystals.⁶ All reports identified a highly defect-dependent surface reactivity.

The surface of CaO is comparatively poorly studied, but is known to be highly reactive with water. In a study of bulk CaO powder at 300 K using water overpressures of approximately 10 Torr, complete hydroxylation of the CaO was observed.⁷ In synchrotron XPS studies of CaO (100) surfaces, reactions were observed with water at pressures as low as 5×10^{-11} Torr, and bulk hydroxylation was seen as the pressure was increased to 3×10^{-4} Torr.⁸ In this letter, we present a comparative study of the reactivity of these two oxides with water under high and ultra-high vacuum conditions, in order to evaluate their suitability in the processing of GaN/ferroelectric devices. Although the films proposed in such structures would be by necessity epitaxial, this study has utilized polycrystalline films to arrive at a conservative assessment of surface reactivity and to eliminate all influence of surface charging.

Experimental Procedure

Polycrystalline films of MgO and CaO were grown via molecular beam deposition directly on the Mo sample holder designed to transfer wafers in the surface analysis system – using this configuration, there is no contribution from surface charging. MgO films were grown at room temperature, while CaO films were grown at 400 °C to avoid excessive

hydroxylation during growth. The base pressure of the growth chamber was $2\text{-}3 \times 10^{-9}$ Torr. Metal flux was provided by effusion cells operating at temperatures of 400 °C (Mg) and 520 °C (Ca) to evaporate metallic source material (Alfa Aesar, 99.9% purity). During growth, the oxidizing flux (molecular oxygen) was supplied through a leak valve to a pressure of 1.0×10^{-6} Torr.

Following growth, the films were transferred, *in vacuo*, to additional chambers for surface analysis or further processing. The base pressure of the transfer line is 1.0×10^{-9} Torr. In order to assess the reactivity of MgO and CaO with residual water vapor, four experiments were performed in the following sequence of increasing exposure to water vapor. First, immediately following growth, the sample was transferred into the surface analysis chamber to assess the as-deposited surface condition. Second, the film was held for 12 hours in the analysis chamber (base pressure: $< 10^{-10}$ Torr). Third, the film was held in the growth chamber for three hours. Finally, the film was exposed to molecular oxygen containing approximately 0.1% water. This exposure was conducted at a total oxygen/water pressure of 1.0×10^{-6} Torr for one hour. Although it is tempting to assign each of these treatments a specific dosage in terms of Langmuir or molecular impingement, due to experimental limitations, we can only make basic assumptions regarding these quantities. Therefore, each treatment is only regarded as a total pressure/time exposure, and not a specific measure of water molecule impingement. After each treatment, the films were transferred back into the surface analysis chamber for evaluation.

XPS analysis was performed using a dual-anode x-ray source and a hemispherical analyzer (VG). All scans were taken using a constant pass energy of 20 eV, unless otherwise noted, and Al K α radiation (1486.6 eV). Since this study focuses only on spectra of the O 1s photoelectron line, and collecting C 1s spectrum is difficult due to spectral overlap in the case of MgO, no effort was made to quantify charging in this study. Thus, binding energy measurements in this study cannot be construed as being placed on an absolute energy scale. However, relative peak separations are still accurate and useful. Peak fitting for quantitative analysis was performed using the Igor Pro analysis suite. Peaks were fit using Voigt functions, constraining peaks within discrete spectra to the same width.

Results and Discussion

Figure 1 shows survey scans of MgO (a) and CaO (b) films grown on Mo sample holders. We include this data to show that, within the sensitivity limits afforded by XPS (> 0.1 at. %), our films are free of surface contamination, as no foreign features are observed. Thus, surface reactivity observed can be assumed to be indicative of the reactivity of pure materials.

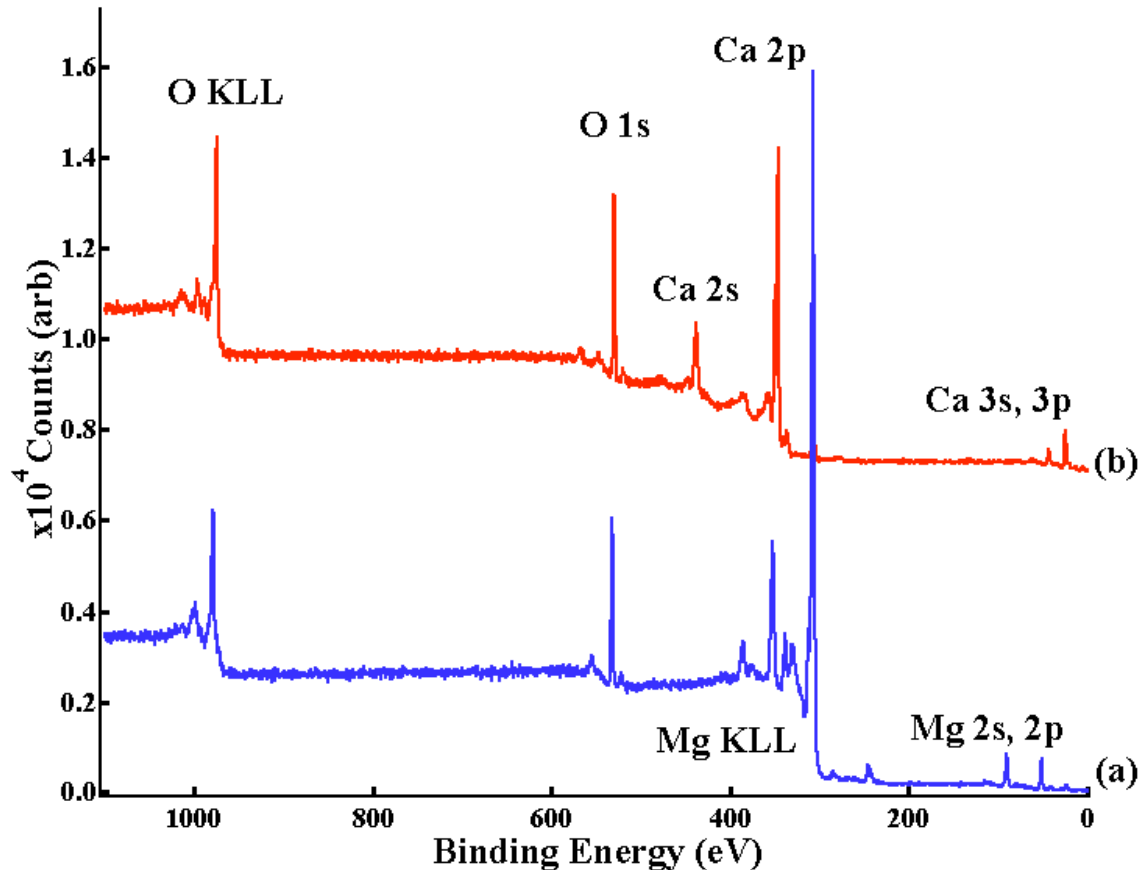


Figure 7.1: XPS survey scans of (a) MgO and (b) CaO polycrystalline films used in this study.

In Figure 2, we show a series of O 1s spectra from the MgO film. In the as-deposited film, the only feature observed is that of the Mg-O bond, indicating a phase-pure surface. As the exposure increases, a small shoulder located 2.0 eV higher in binding energy is observed. This feature, and its separation from the primary metal-oxygen feature, is consistent with the formation of surface hydroxyls,³ or a substoichiometric phase of $\text{Mg}(\text{OH})_2$ formed through dissociative adsorption of water molecules. This feature does not exist prior to the 2.0×10^{-9}

Torr, three-hour treatment, suggesting that the driving force for the hydroxylation reaction is insufficient in this pressure range, or that the reaction is kinetically limited to amounts undetectable by XPS. A final exposure of 1.0×10^{-6} Torr O_2/H_2O for leads to no further hydroxylation.

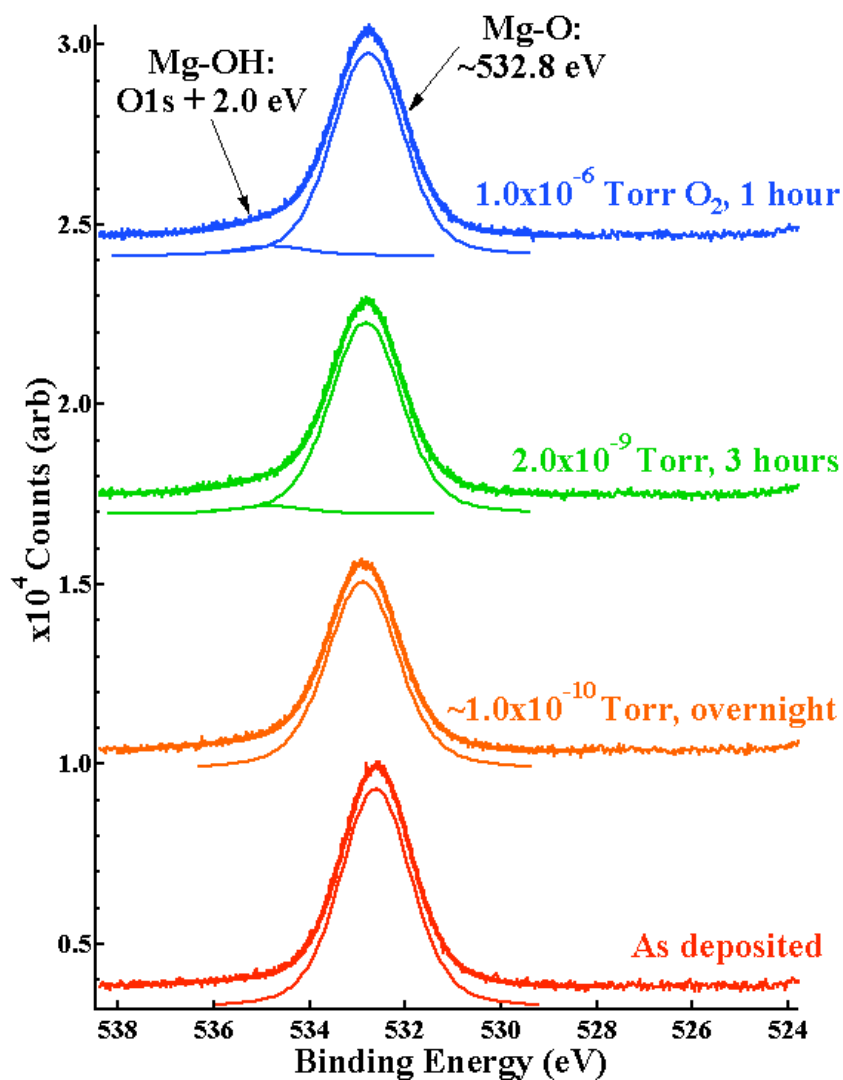


Figure 7.2: O 1s photoelectron spectra of MgO film following various exposures.

By comparing the intensity of the Mg-O O 1s line in the as-deposited state to its final intensity after all treatments, and assuming that the overlayer of Mg(OH)_x formed results in exponential decay of that signal (i.e. the overlayer is dense), the monolayer coverage of hydroxide can be estimated, by applying the signal attenuation model⁹ for dense overlayers:

$$\frac{I_s}{I_o} = e^{-t/\lambda}, \quad [7.1]$$

where I_s/I_o represents the ratio of the attenuated O 1s intensity to the original intensity, t is the overlayer thickness, and λ the inelastic mean free path. We estimate a coverage of ~1.3 ML in the case of the 2.0×10^{-9} Torr, one hour exposure, and 1.1 ML for the final treatment. This data is in good agreement with previous work, using temperature programmed desorption, on single-crystal MgO samples⁶, and also agrees with the finding³ that the reaction is insensitive to exposure time below 10^{-4} Torr. However, in further study, the authors of [ref 3] found that defective MgO surfaces (such as those one might expect for polycrystalline films) have enhanced reactivity with water through dissociative chemisorption at defect sites, and were unable to prevent hydroxylation even at pressures $< 10^{-10}$ Torr.⁴ No such enhanced reactivity was observed in this study, however the referenced work utilized synchrotron radiation, enabling increased surface sensitivity. This may explain the difference in our findings, as the present instrumentation is not sensitive to the 0.3 ML coverage observed by synchrotron analysis.

The results of a similar set of experiments carried out for polycrystalline CaO films are shown in Figure 3. In the as-deposited state, the O 1s photoelectron peak shows a small shoulder 2.8 eV higher in binding energy, and of about 2% of the intensity of the main Ca-O

peak. In subsequent exposures, we observe the evolution of two new features: a peak at 2.2 eV higher binding energy than the Ca-O peak, corresponding to adsorbed -OH groups (similarly to the case of MgO), and a second feature 3.1 eV higher in binding energy, corresponding to molecularly adsorbed water molecules. The chemical shifts observed here agree well with those seen in a previous study of single-crystal CaO surfaces⁸.

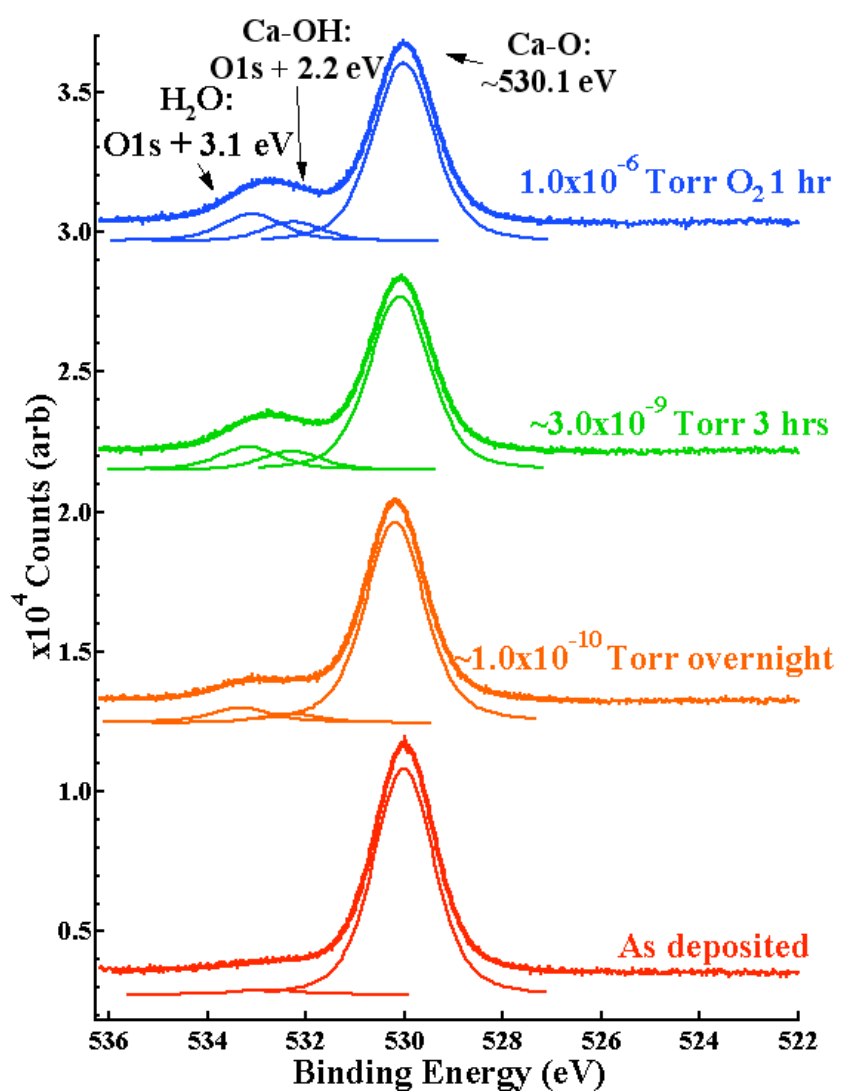


Figure 7.3: O 1s photoelectron spectra of CaO film following various exposures.

CaO exhibits significantly increased reactivity with water vapor with respect to MgO. Following overnight UHV storage, a significant shoulder corresponding to –OH groups and physisorbed water is present. We estimate the hydroxyl coverage in this case to be approximately 1.2 ML, while the intensity due to molecularly adsorbed water corresponds to approximately twice that value. In subsequent treatments the hydroxyl coverage increased, and appeared to saturate, to 3.0 ML following three-hour storage in the growth chamber, and 2.4 ML following the flowing O₂/H₂O treatment. In previous data⁸ investigating high quality single-crystal CaO (100) faceted surfaces, similar total exposures produce surface saturation at a lower value of approximately 0.8 ML. The increased reactivity we observe is understood given the comparatively defective nature of the polycrystalline surface investigated.

After the four systematic exposures, the CaO(OH)_x film was annealed under vacuum at 500 °C for one hour. The pressure during this anneal was approximately 1x10⁻⁷ Torr. In Figure 4, we show a scan of the O 1s peak following this anneal, as well as a scan of the same film in the as-deposited state for comparison. The relative peak intensities and separations in the post-anneal scan are identical to those of the as-deposited film, indicating recovery of the surface. This result is expected given the thermodynamic instability of hydroxylated phases at elevated temperatures.

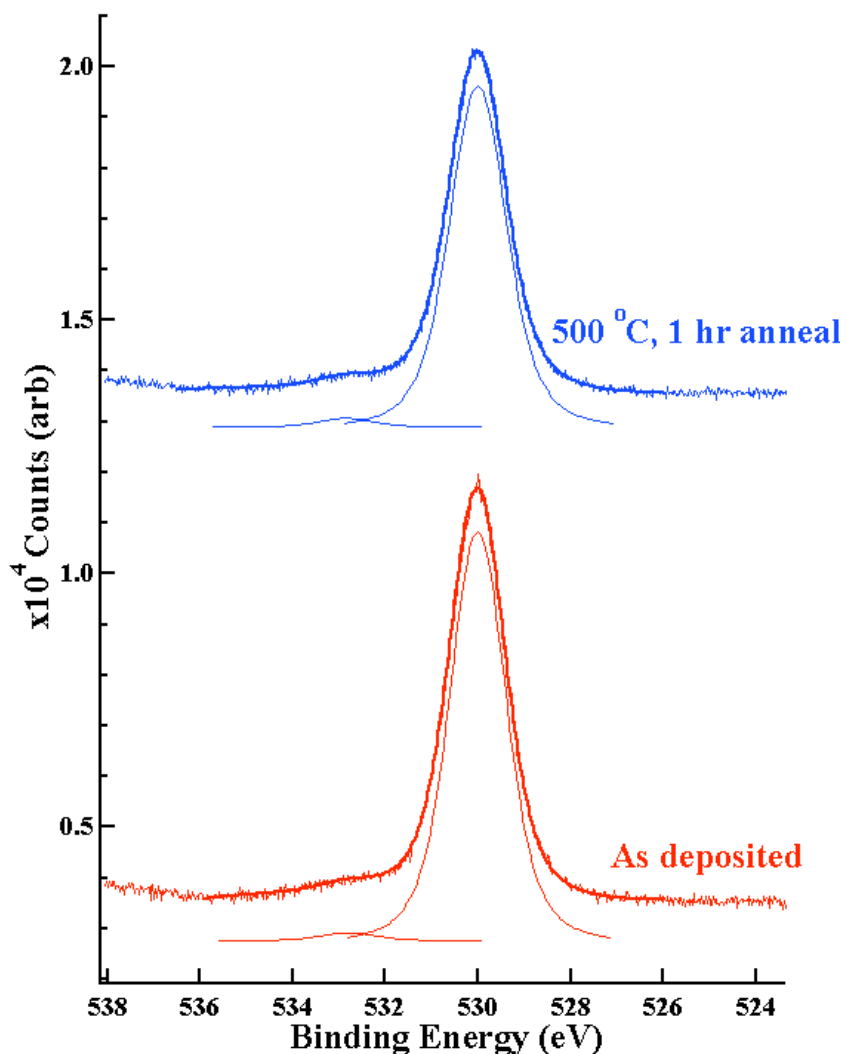


Figure 7.4: O 1s spectra comparing CaO surface following 500 °C recovery anneal to as-deposited surface.

As shown in Figure 5, the driving force for the reaction of CaO with H₂O to form Ca(OH)₂ becomes smaller at elevated temperatures, and the hydroxide phase decomposes (in air) at approximately 500 °C. This data was calculated from ref[10]. Thus, even with an impure oxygen source such as that used in the present study, the deposition of phase-pure

CaO is possible at elevated temperatures; this has been experimentally verified by Losego *et al*¹¹, and can be maintained as such using *in vacuo* anneals as necessary. We observe similar behavior in the case of MgO films; in this case, lower temperatures (~ 250 °C) being necessary for surface recovery through hydroxide decomposition.

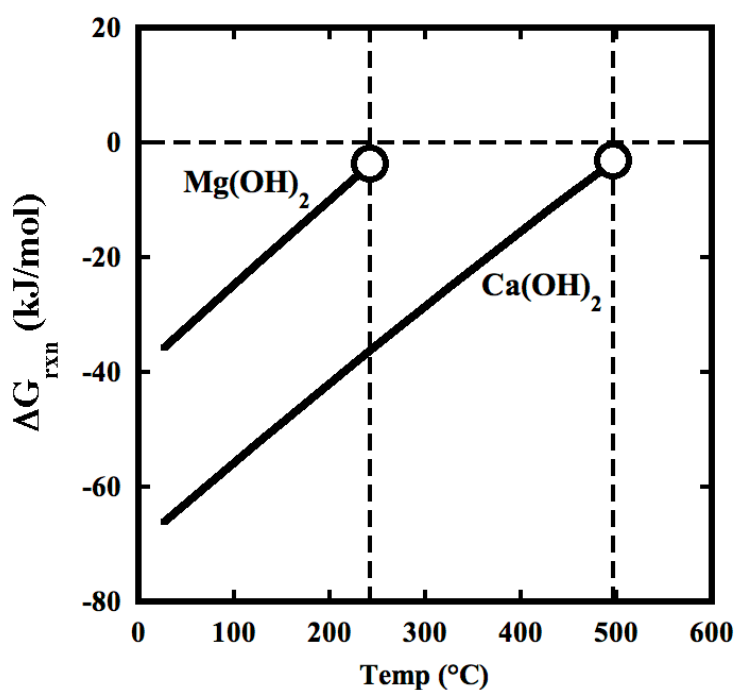


Figure 7.5: Free energies for the bulk reactions of CaO and MgO with water to form hydroxide phases. The open circles denote the decomposition temperature of the hydroxide compound. Calculated from [10].

These data present the opportunity to explain the morphology differences that are observed between epitaxial MgO and CaO films on GaN. Our group recently showed through XPS attenuation data that CaO films coalesce on GaN nearly 10 times faster than MgO². Using the data presented here, we hypothesize that the much higher reactivity of CaO produces a film surface during growth in equilibrium with adsorbed water. The {111} face of

rocksalt oxides is polar, and thus unstable without reconstructions or adsorbates to compensate the polarization charge. It has been shown both theoretically^{12,13} and experimentally¹⁴ that a hydroxyl-terminated {111} surface is more stable than the bulk-terminated {100} surface. The adsorbed hydroxide compensates the polarity of the {111} rocksalt surface and prevents the formation of facets that roughen the surface to minimize free energy. We propose this compensation as a possible mechanism for the improved growth characteristics of CaO on GaN. In the absence of faceting, CaO films may coalesce more rapidly.

Conclusion

In conclusion, we have presented a comparative study of the reactivities of the rocksalt oxides MgO and CaO with water under ultra-high and high vacuum conditions. For exposures up to 10^{-6} Torr/1 hour, the surface of polycrystalline MgO forms a hydroxide coverage of approximately 1 ML, and is unreactive at lower exposures. The surface of CaO is, in contrast, significantly more reactive; reaction could not be prevented at any level of exposure, and was accompanied by the presence of adsorbed water. However, we show that this increased reactivity is manageable, provided that elevated temperatures are available under vacuum. These data also provide a means to understand the development of morphology in ultra thin rocksalt films via the solid phase – vapor phase interactions during growth. The fact that these surface reactions are shown to be controllable using equipment commonly available in thin film processing, coupled with the known band offsets and growth

behavior on GaN, suggest that these rocksalt oxides remain viable candidates as buffer layers in GaN multifunctional devices.

Acknowledgements

H.S.C, M.D.L., and J-P.M. are supported by the Office of Naval Research, under the Epitaxial Multifunctional Materials and Applications MURI program (2004-0779), monitored by Dr. Colin Wood and managed by Professor Alan Doolittle.

REFERENCES

- ¹ H. S. Craft, R. Collazo, M. D. Losego, S. Mita, Z. Sitar, and J. P. Maria, *Journal of Applied Physics* **102**, 074104 (2007).
- ² H. S. Craft, R. Collazo, M. D. Losego, S. Mita, Z. Sitar, and J. P. Maria, *Applied Physics Letters* **92**, 082907 (2008).
- ³ P. Liu, T. Kendelewicz, G. E. Gordon, and G. A. Parks, *Surface Science* **413**, 287-314 (1998).
- ⁴ P. Liu, T. Kendelewicz, and G. E. Brown, *Surface Science* **413**, 315-332 (1998).
- ⁵ C. F. Jones, R. A. Reeve, R. Rigg, R. L. Segall, R. S. C. Smart, and P. S. Turner, *Journal of the Chemical Society, Faraday Transactions* **80**, 2609-2617 (1984).
- ⁶ M. J. Stirniman, C. Huang, R. S. Smith, S. A. Joyce, and B. D. Kay, *Journal of Chemical Physics* **105**, 1295-1298 (1996).
- ⁷ B. Fubini, V. Bolis, M. Bailes, and F. S. Stone, *Solid State Ionics* **32-3**, 258-272 (1989).
- ⁸ P. Liu, T. Kendelewicz, G. E. Brown, G. A. Parks, and P. Pianetta, *Surface Science* **416**, 326-340 (1998).
- ⁹ Z. Sitar, L. L. Smith, and R. F. Davis, *Journal of Crystal Growth* **141**, 11-21 (1994).
- ¹⁰ I. Barin, *Thermochemical Data of Pure Substances*, Vol. 1 (VCH Publishers, New York, 1989).
- ¹¹ M. D. Losego, S. Mita, R. Collazo, Z. Sitar, and J. P. Maria, *Journal of Vacuum Science & Technology B* **25**, 1029-1032 (2007).
- ¹² A. Pojani, F. Finocchi, J. Goniakowski, and C. Noguera, *Surface Science* **387**, 354-370 (1997).
- ¹³ A. Wander, I. J. Bush, and N. M. Harrison, *Physical Review B* **68**, 233405 (2003).
- ¹⁴ R. Hacquart and J. Jupille, *Chemical Physics Letters* **439**, 91-94 (2007).

8. GaN Surfaces

Several observations were made regarding the qualities of GaN surfaces utilized for the experiments during the course of this thesis. Though in some cases, the findings represent isolated experiments that could not be investigated fully, these observations are reported in this chapter, as they provide pathways defining opportunities for future work. They concern measurements of the GaN surface stoichiometry, effects of wet chemistry, and relative cleanliness of n-type and p-type GaN surfaces.

8.1 Surface Stoichiometry

The measured stoichiometry of the GaN surface as determined by XPS has been the subject of light interest in the open literature for approximately the past decade. Typical XPS measurements, like those performed for this thesis, consist comparing the integrated intensities of the Ga $2p_{3/2}$ and N 1s photoelectron lines, using the appropriate atomic sensitivity factors (3.341 for Ga and 0.477 for N).¹ Typical Ga:N ratios for MOCVD-grown GaN films range from 1.3:1² up to 4:1.³ The Ga-rich nature of the surfaces is generally attributed to surface oxidation, which leads to a surface Ga_xO_y phase, suppressing the N 1s signal.^{2,4-6} However, corroborating data from the O 1s photoelectron line rarely supports this supposition (if it is even presented), and the chemical shift between oxide and nitride bonding in Ga features is too small to be observable by most XPS systems.

Additionally, even with the nearly universal observations of highly Ga-rich GaN surfaces (only one recent letter reports a slightly N-rich surface⁷), there is little speculation

regarding the nature of the Ga excess, no agreement regarding procedures for obtaining stoichiometric surfaces, or any evidence suggesting that such a surface is necessarily desirable or undesirable over an as-grown GaN surface. Though a comprehensive study would be beyond the scope of this thesis, some observations regarding the measurements of GaN surface stoichiometry performed during the course of this work are presented in this section.

Figure 8.1 depicts a typical measurement of the Ga:N ratio. The sample is prepared and loaded as described in Chapter 4. After offgassing, the Ga $2p_{3/2}$ and N 1s peaks are investigated in the surface analysis chamber, using Mg $K\alpha$ radiation to shift the Ga LMM Auger series away from the N 1s line at ~ 400 eV. O 1s peak intensities for n-type and insulating GaN samples are typically indicative of sub-monolayer quantities of adsorbed oxygen, approaching the detection limit of XPS. Thus, the characteristic Ga-rich stoichiometry is not consistent with a gallium oxide surface phase.

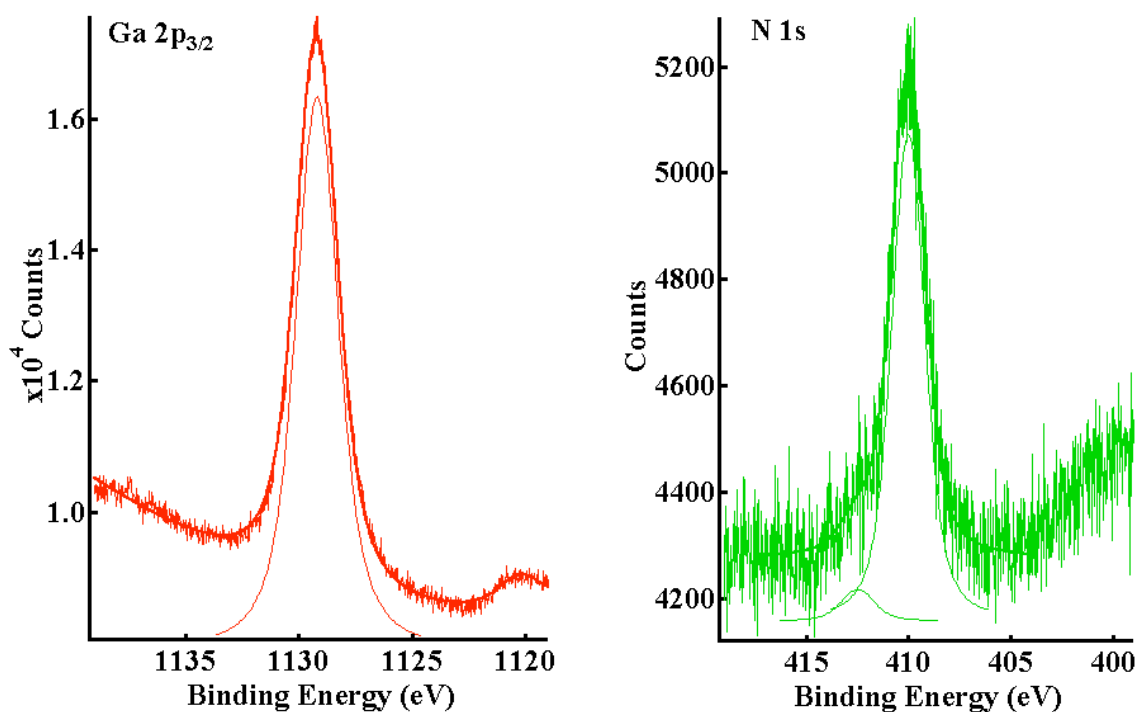


Figure 8.1: Representative data showing the Ga 2p_{3/2} and N 1s photoelectron line from an undoped GaN sample. Note that the energy scale for these plots is not charge corrected. The shoulder on the N 1s plot is due to residual N-O bonding.

As shown in Figure 8.1, the areas of the Ga 2p_{3/2} and N 1s peaks are determined, then normalized using the atomic sensitivity factors. The Ga:N ratio (of the form x:1) can be determined by the relation

$$\text{Ga} : \text{N} = \frac{I_{\text{Ga}} F_{\text{N}}}{I_{\text{N}} F_{\text{Ga}}}. \quad [8.1]$$

The stoichiometry measured from the data in Figure 8.1 is Ga_{1.6}N, a value typical to the GaN studied here.

Two common methods for addressing Ga-rich surfaces are anneals under NH_3 atmospheres,^{3,4} and nitrogen ion-beam sputter/annealing cycles.^{4,6} Both procedures should be performed *in-vacuo*. In this work, vacuum annealing and argon ion-beam sputtering was investigated. In all cases, room temperature sputtering resulted in an increase in the Ga:N ratio. For example, for the sample measured in Figure 8.1, a ten-minute treatment of Ar sputtering led to a final Ga:N ratio of 2.6:1, for a surface stoichiometry of $\text{Ga}_{2.6}\text{N}$. The increase in the apparent Ga content of the surface is understood as result of a surface contamination effect. Electrons producing the Ga $2p_{3/2}$ photoelectron line have a kinetic energy of ~ 130 eV when excited using Mg $K\alpha$ radiation, compared to ~ 830 eV for the N 1s photoelectrons. This wide disparity in kinetic energies leads to a significant difference in inelastic mean free path and sampling depths, with the Ga $2p_{3/2}$ photoelectron line being more surface sensitive. Ar sputtering is known to remove trace amounts of adventitious contamination (O, C) such as that observed on GaN surfaces in this work, and the result is a comparative gain in intensity of the more surface sensitive photoelectron line.

A similar effect was observed after a ten-minute Ar sputtering treatment with the sample held at 600°C . In this case, the beginning stoichiometry (after room-temperature sputtering) was $\text{Ga}_{2.5}\text{N}$. Following high-temperature sputtering, the surface stoichiometry increased to $\text{Ga}_{2.9}\text{N}$. The increase in the Ga content is likely due to an observed increase in the GaN surface oxidation, as shown in Figure 8.2. Although the formation of a surface oxide phase was not quantified due to the very low signal to noise ratio of the O 1s peak in the

~monolayer coverage regime, the formation of small amounts of surface oxide is consistent with a decrease in the observed nitrogen content of the surface.

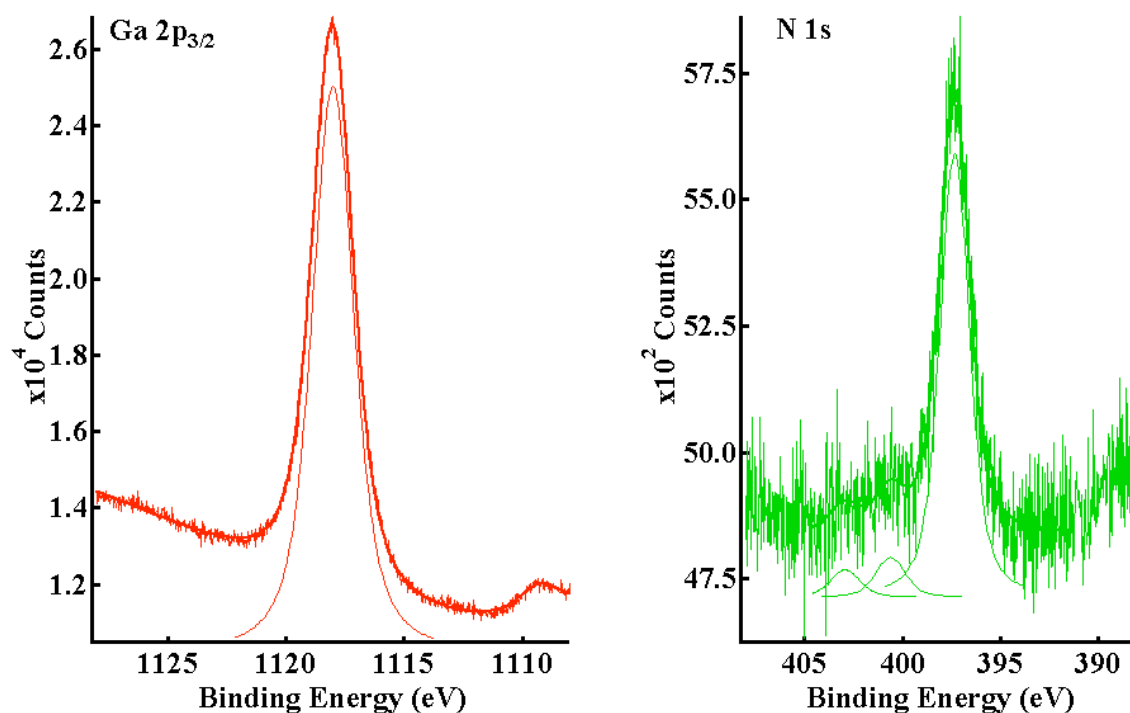


Figure 8.2: Ga 2p_{3/2} and N 1s photoelectron lines taken from GaN exposed to Ar ion beam sputtering for ten minutes at 600 °C.

Previous literature reports of GaN annealed in nitrogen or ammonia atmospheres showed a reduction of the Ga:N ratio of n-type GaN samples to near unity. Vacuum annealing performed as part of this study had no effect on the stoichiometry of n-type surfaces. However, a decrease in the Ga:N ratio of p-type GaN was observed as a function of annealing temperature, as shown in Figure 8.3.

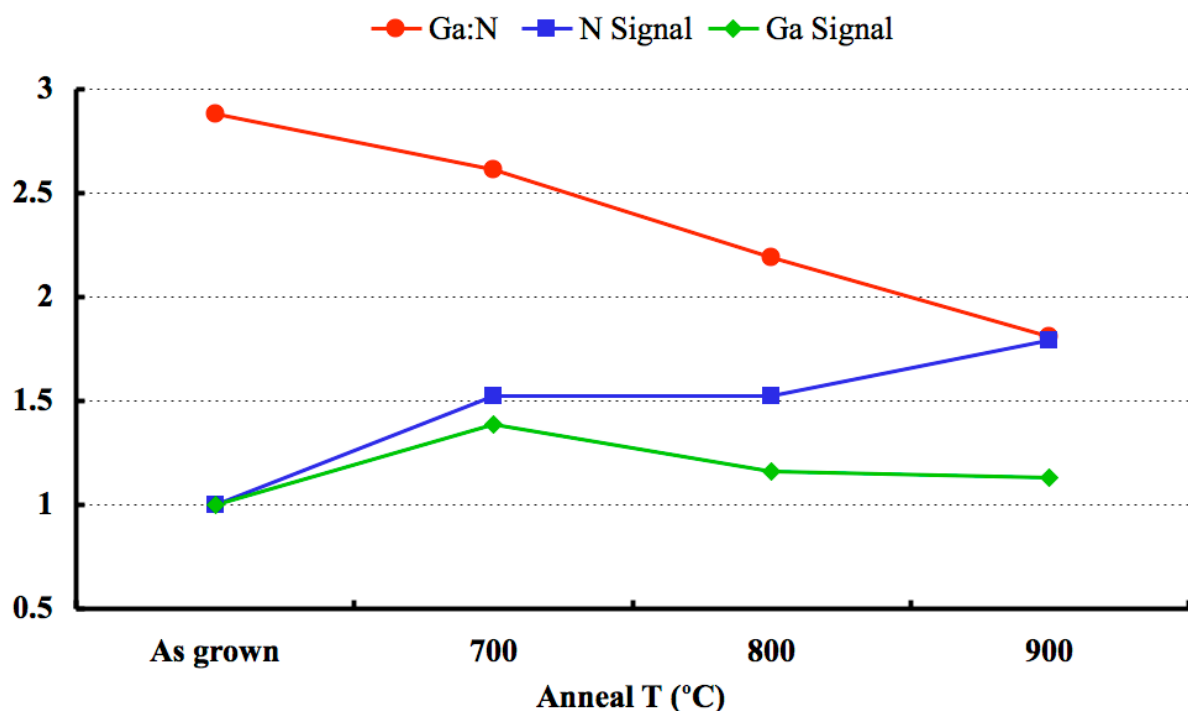


Figure 8.3: Evolution of surface stoichiometry of p-type GaN following one-hour vacuum anneals at 700, 800, and 900 °C. The final stoichiometry is $\text{Ga}_{1.8}\text{N}$.

In contrast to the high-temperature sputtering experiment presented in Figure 8.2, the annealing of the GaN surfaces at high temperatures did not appear to bring about significant surface oxidation, as shown by Figure 8.4 (again, quantitative assessment of the oxygen coverage was difficult for this experiment). Presumably, the absence of ion-beam induced surface damage in the annealing experiments made the oxidation of the GaN surface less kinetically favorable. While some increase in the O KLL Auger series intensity is discernible, this would lead to an increase in the Ga:N ratio, rather than the observed decrease.

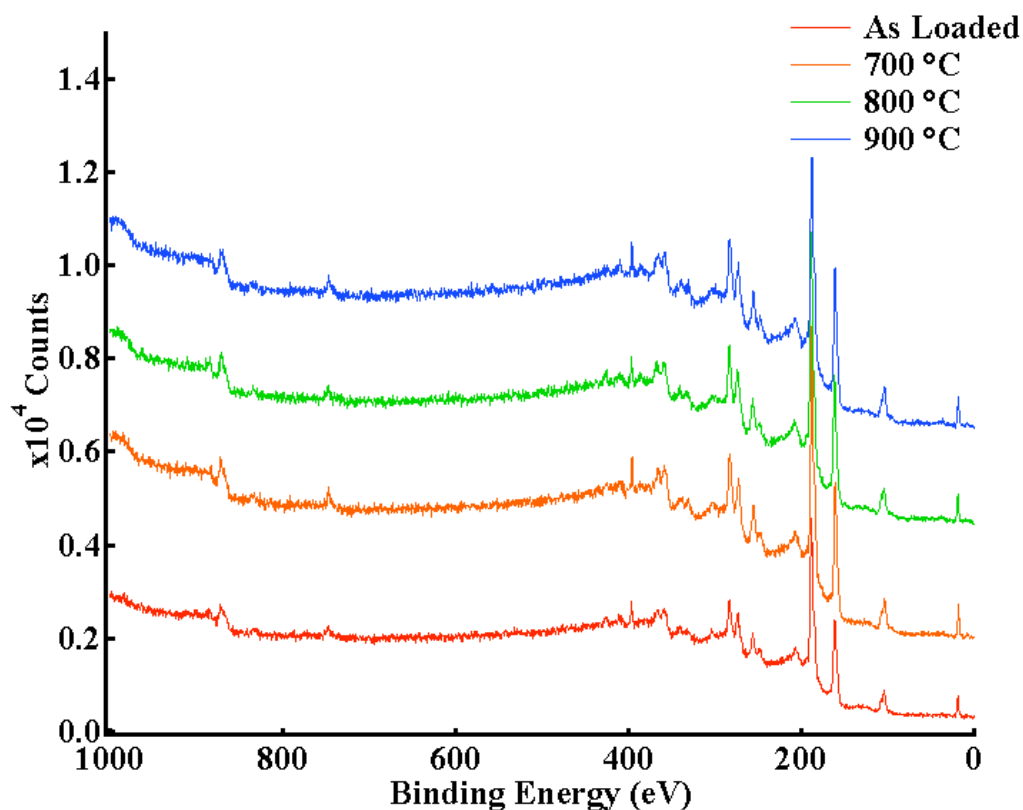


Figure 8.4: Survey scans taken using Mg K α radiation of GaN surfaces subsequent to each annealing stage. Note the O KLL Auger series at ~ 770 eV.

Through the course of the GaN surface stoichiometry investigation, a large number of measurements were performed on a wide array of substrates. Early attempts to correlate the range of Ga:N ratios suggested that the Ga supersaturation during GaN growth (see Chapter 3) establishes the final stoichiometry of the surface. However, as shown in Figure 8.5, after having investigated the range of available supersaturations in the Sitar MOCVD, no affect on the Ga:N ratio is discernible. Furthermore, several measurements were taken using wafers made at the “standard” GaN growth condition of a Ga supersaturation equal to 44. The

observed Ga:N ratios span the range traversed by all samples measured, further eliminating the possibility of a supersaturation trend. One might speculate that the observed surface stoichiometry is a result the specifics of how the GaN growth is completed: at a growth temperature of ~ 1050 °C, the GaN is thermodynamically unstable, and must be held under an ammonia atmosphere to prevent full decomposition. Therefore, small variations in the manner in which the growth is ended and the sample cooled may have large impacts on the final stoichiometry of the surface region accessible by XPS.

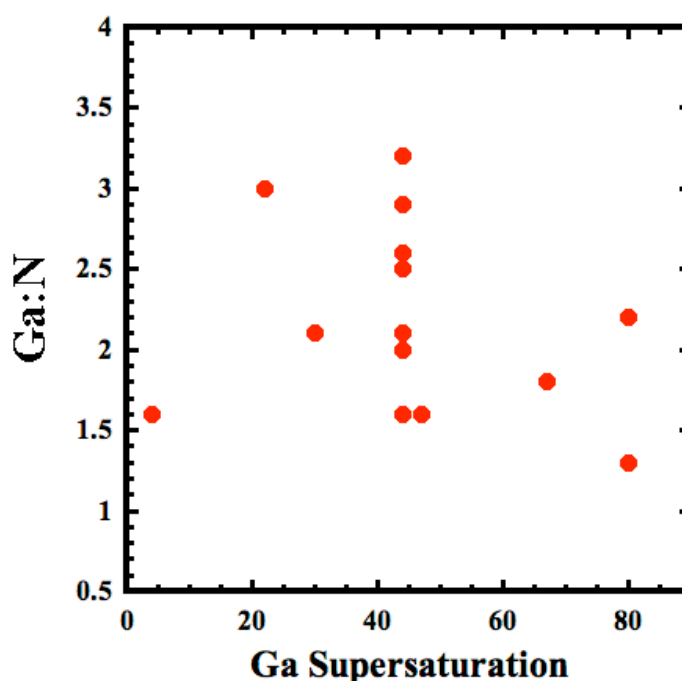


Figure 8.5: Ga:N ratio vs. Ga supersaturation for several GaN films. Measurements of multiple areas on the same wafer are omitted from this plot. Note that the range of stoichiometries observed at a Ga supersaturation of 44 spans the range observed by all samples.

Further evidence for this effect can be observed by considering the Ga:N ratio as a function of GaN growth time (or the amount of time that the Ga source, triethyl gallium, is flowing). As shown in Figure 8.6, the Ga:N ratio increases with the length of the deposition. The film corresponding to the data point at 120 minutes was grown in an attempt to verify the trend. The data falls below a linear trend, and may indicate a saturating effect with time, or some degree of experimental scatter. Still, the dependency of the Ga:N ratio with time enables a possible explanation for the excess Ga: the presence of residual Ga in the reactor after the growth is terminated provides a source of Ga, which is still sufficiently volatile at high temperatures, before the reactor cools. The residual Ga is observed subsequent to each deposition run, though its nature has not been characterized.

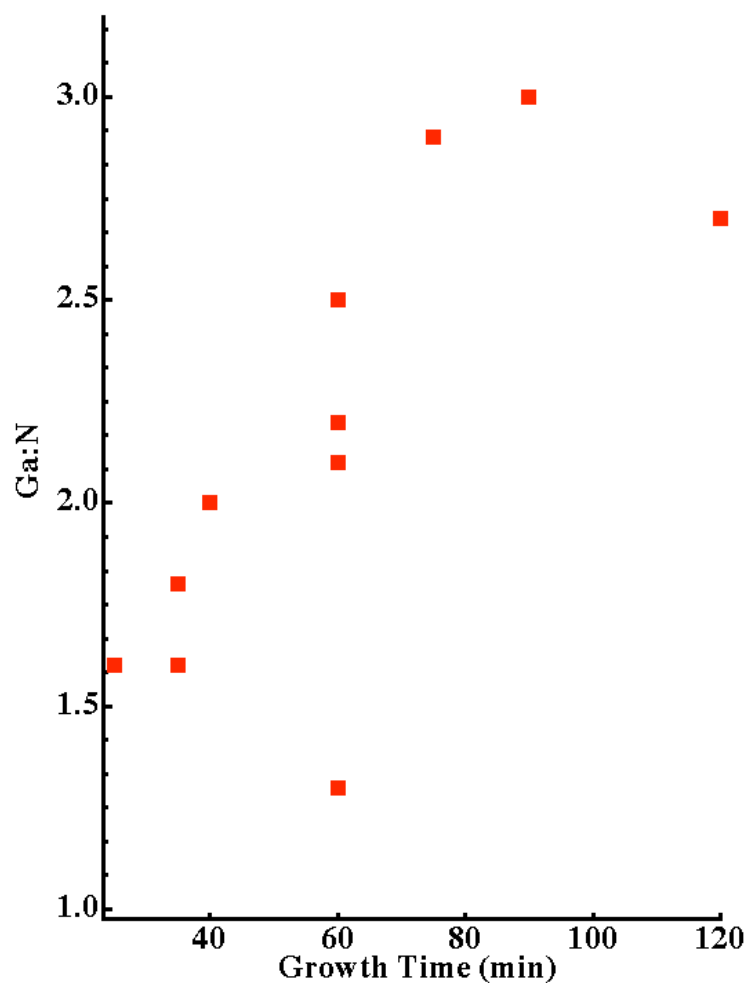


Figure 8.6: Ga:N ratio as a function of growth time.

Though the growth time dependency presents a “universal” explanation for the excess Ga measured on GaN substrates, it should be stressed that the observation does not speak to the nature of the excess Ga. The excess Ga cannot be determined by the spectrometer used for this work; the resolution is insufficient to resolve the small chemical shifts inherent to Ga. Further work should focus on this determination, as well as the possibility for utilizing the

MOCVD reactor to anneal GaN films at high temperatures, under flowing NH_3 , to attempt to drive the Ga:N ratio closer to unity.

8.2 GaN Chemical Treatments

The use of wet chemistry to prepare GaN surfaces for electronic device fabrication has been an area of some debate. Although not the first to do so, the brief review by King *et al.* in 1998 discusses many different chemistries for GaN and AlN cleaning and their evaluation by XPS and Auger electron spectroscopy (AES).⁸ The authors investigated various mixtures of HCl, HF, NH_4F , HNO_3 , H_2SO_4 , H_3PO_4 , H_2O_2 , NH_4OH , NaOH, KOH, and RCA clean mixtures SC1 and SC2 (1:1:5 $\text{NH}_3\text{OH}:\text{H}_2\text{O}_2:\text{H}_2\text{O}$ and 1:1:5 HCl: $\text{H}_2\text{O}_2:\text{H}_2\text{O}$, respectively, at 85 °C). HCl and HF were found to be the most effective etchants for removing C contamination, while HCl, HF, and NH_4OH were most effective at removing surface oxides. Based on this work, a 1:1 HCl: H_2O etch followed by a 1:99 HF: H_2O etch has become the standard GaN wet chemical treatment for most researchers, including the work performed in this thesis, as well as previous oxide-GaN investigations performed at NC State.⁹

However, recent work by M.D. Losego suggests that the standard HCl/HF GaN pretreatment is not the optimal preparation for GaN surfaces, if the metric for evaluating the treatment is the electrical quality of an epitaxial oxide grown on the GaN.⁹ In his work, Losego showed that the leakage current through a GaN/CaO/MgO structure is dominated by Frenkel-Poole defect-assisted tunneling if the GaN is exposed to the HCl/HF etch. Through evaluating several other wet chemistries, Losego showed that a treatment consisting of a 1:1

HCl:H₂O etch followed by a buffered HF etch (1:6 HF:NH₄F) led to a reduction in leakage current with a concomitant change in the leakage mechanism, from Frenkel-Poole to field emission by the Fowler-Nordheim mechanism. This change in the mechanism implies an improvement in the interface quality of the CaO/GaN structure, presumably brought about by some change in the GaN surface by the modified etching procedure.

In Figure 8.7, a series of XPS scans is shown in which the O 1s photoelectron line is investigated for the three surface treatments of interest: no treatment (as-received GaN), the standard HCl-HF treatment, and the HCl-HF:NH₄F treatment responsible for reducing the oxide leakage current. These data show the contamination level of the GaN surface prior to, and subsequent to, the surface treatments. While the signal to noise ratio is limited, the oxide coverages can be estimated roughly. In the as-received case, the coverage is approximately 0.9 monolayers, and the surface layer consists of a ~28:72 mixture of oxide:hydroxide surface species or adsorbates. For both etches, the oxide coverage decreases to about 0.5 monolayers, with the HCl-HF etch leaving behind a similar mixture of oxide/hydroxide species as the as-received surface. The surface layer after the HCl-buffered HF etch consisted of an approximate composition of 22:78 oxide:hydroxide. From these observations, the two etches can be concluded to be similar from the standpoint of surface cleanliness (a similar analysis for the C contamination yields analogous results, with slightly smaller monolayer coverages).

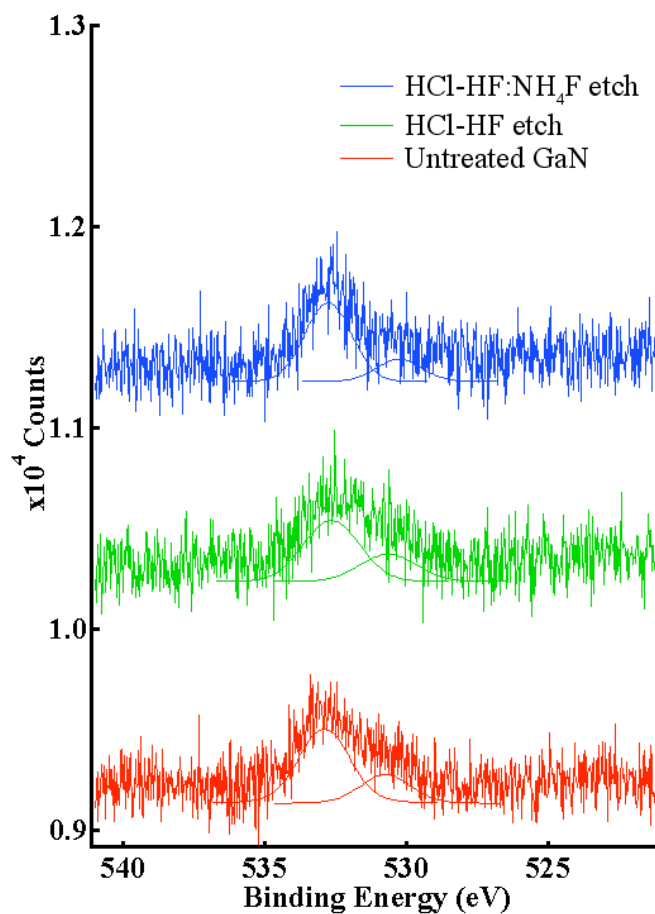


Figure 8.7: O 1s photoelectron spectra of untreated GaN, the standard HCl-HF etch, and the HCl-buffered HF etch. The peak at lower binding energy corresponds to a metal oxide, while the peak at higher binding energies corresponds to a hydroxide phase.

In addition to observing no significant chemical change as a result of the modified etching procedure, no quantitative topographical change was observed by atomic force microscopy, as shown in Figure 8.8.

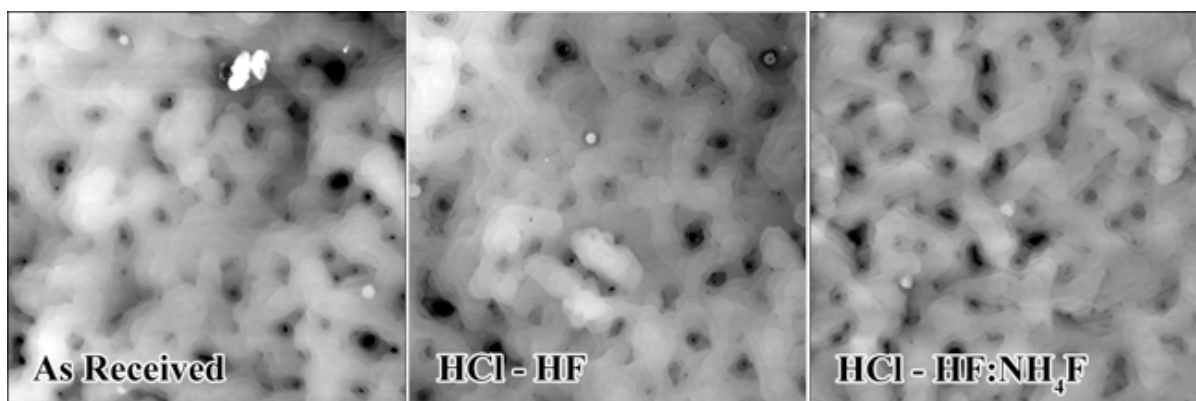


Figure 8.8: Atomic force microscopy images of GaN surfaces after the denoted chemical treatments. Each image is $5\ \mu\text{m} \times 5\ \mu\text{m}$, and the vertical scales span 11 nm. The RMS roughness of the three surfaces varies from 1.5 nm for the as-received surface, to 1.2 nm for the surface exposed to the buffered etch.

Having observed no substantive chemical or topographical difference on the GaN surface between the two etches of interest, it may be hypothesized that the change in leakage current behavior results from a reduction in surface states, which act as sites to initiate defect-assisted tunneling into the oxide films. By XPS, such a reduction in surface states would be observed in the valence band region. In Figure 8.9, the valence band regions of GaN having been etched by the standard HCl-HF process and the HCl-buffered HF etch are shown. While chemical identification of valence band features in XPS is difficult without extensive studies, it can be noted that while the two valence band maxima have similar values in binding energy, the uncertainty in the HCl-HF etched valence band maximum is increased due to a general broadening of the data in the region of the band edge. Increasing the resolution of the experiment by decreasing the pass energy to 10 eV (from the typical 20 eV), showed that the broadening of the band edge is not due to instrumental factors. The

band edge of the GaN etched in the buffered solution has a qualitatively sharper transition. This difference may be due to a reduction in surface states as a result of the buffered etch, which is consistent with the leakage current data of Losego. Unfortunately however, the surface sensitivity of XPS in this binding energy region is poor, and XPS is not sensitive to a population of surface states $< 10^{13} \text{ cm}^{-2}$. The use of UPS to investigate this phenomenon would be more appropriate, so that greater resolution and surface sensitivity may be utilized.

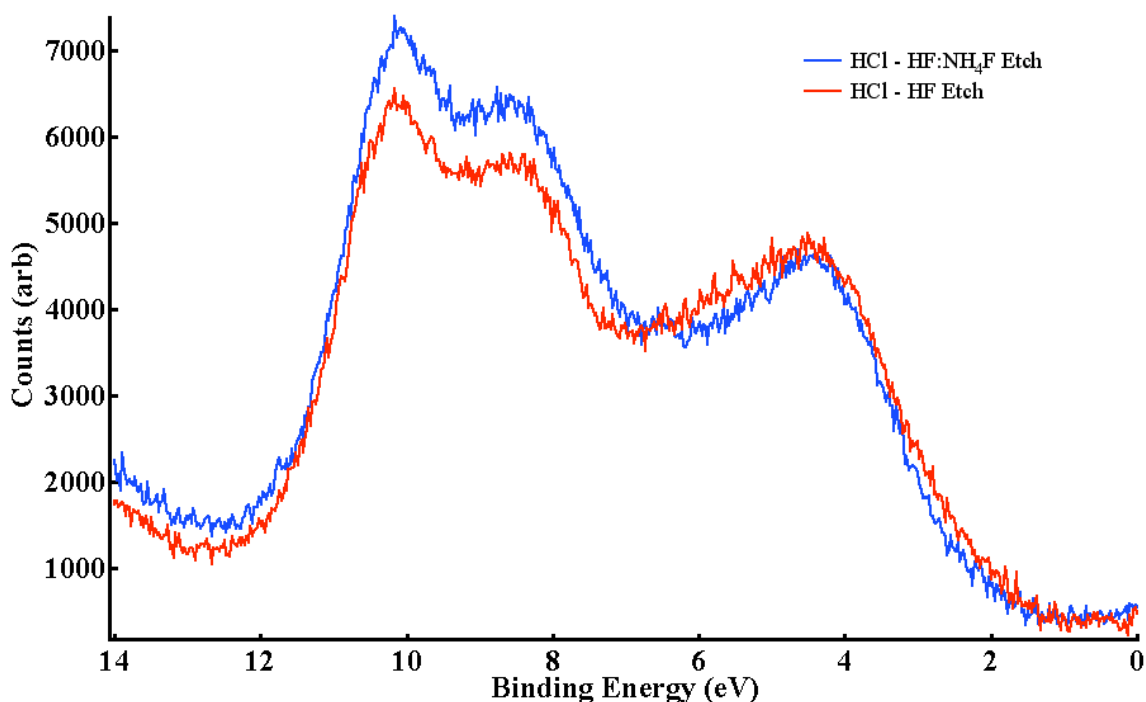


Figure 8.9: Valence band spectra of the GaN surface after the HCl-HF etch (red), and the HCl-HF:NH₄F etch (blue).

As a final note on GaN wet chemical treatments, the previous work by Losego investigating GaN surface preparation also included treatments reversing the order of the HCl-HF etch, so that the final treatment was an exposure to concentrated HCl.⁹ This

treatment carried with it a surprising effect: the nearly complete cessation of MgO growth over GaN surfaces by MBE. Losego showed that this treatment could be used to lithographically MgO films. XPS investigations of this treatment showed that the use of concentrated HCl left a residual contamination of Cl on the GaN surface, of approximately one monolayer, as shown in Figure 8.10. No chemical shifts of the Ga core levels were observed.

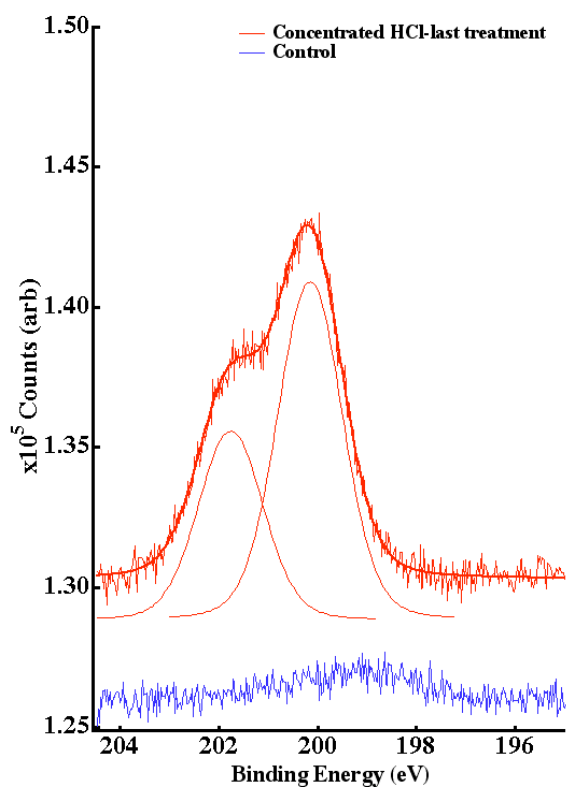


Figure 8.10: XPS scans of Cl 2p core level photoelectron lines of GaN surfaces exposed to an HCl-last treatment and the standard HCl-HF treatment.

In the previous work by Losego, the deposition of MgO on surfaces treated with the HCl-last etch could not be completely ruled out through XRD or EDS characterization. In

this study, XPS allows the question to be addressed definitively. A GaN substrate was treated with the HCl-last etch and exposed to MgO growth conditions that should result in a ~20 nm MgO film under normal etching procedures ($\sim 5 \times 10^{13}$ Mg/cm²·s flux, 3×10^{-6} Torr O₂, and a substrate temperature of 475 °C for 35 minutes). To estimate the thickness of the MgO film, the intensities of the Mg 2p and Ga 2p_{3/2} photoelectron lines were determined. The coalescence data presented in Chapter 5 provides an MgO thickness-dependent database against which the present data can be compared. It shows that the thickness of the deposited film was ~10 nm. This assessment, while only semiquantitative, shows that the HCl-last treatment decreased the deposition rate by approximately a factor of two. This effect is not currently understood, but can be globally considered as a decrease in the Mg sticking coefficient. Presumably, thicker films may be grown in this manner and fully characterized; the deposition rate dependence of the MgO crystal quality observed by Losego implies that these films may be of higher quality than those grown using the standard wet chemistry.

8.3 Surface oxidation differences arising from GaN doping

Through the course of various investigations, a difference was noted in the relative cleanliness of untreated GaN surfaces depending on the doping type. Si-doped GaN (n-type) and insulating GaN exhibited monolayer and submonolayer coverages of oxygen and carbon, as discussed previously. In contrast, Mg doped, p-type GaN consistently had 1-2 nm of surface oxide, as measured by XPS. Additionally, the oxide was of a different chemical composition as that typically seen on GaN surfaces, as described in the previous section. Figure 8.11 shows O 1s core level scans of p-type GaN and n-type GaN for comparison. The

p-type GaN surface is capped by ~ 1 nm of Ga_2O_3 , in contrast to the case of n-type and undoped samples, in which submonolayer quantities of oxide and hydroxide contamination were found.

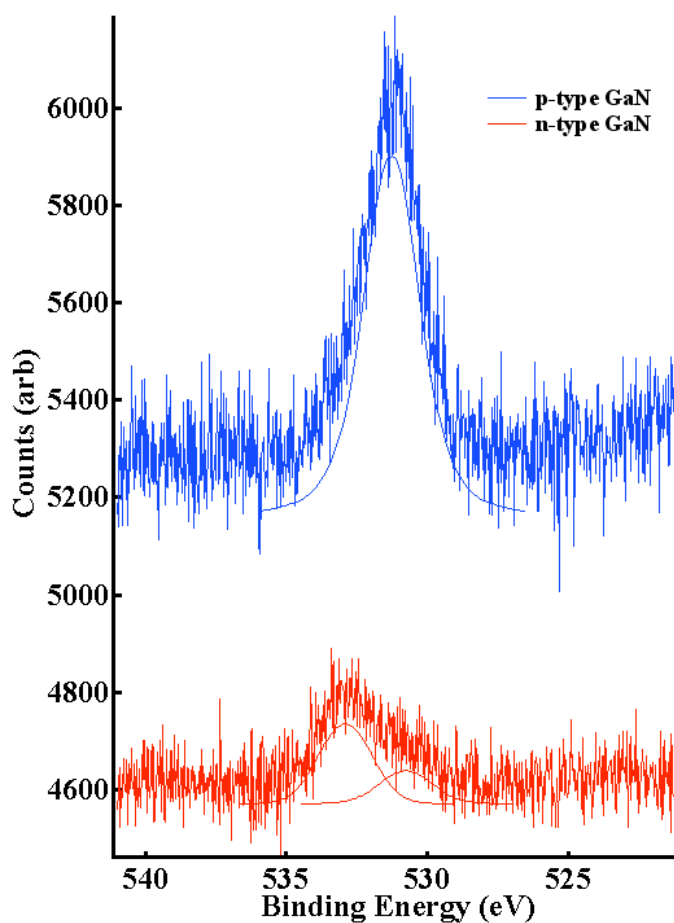


Figure 8.11: O 1s core levels comparing the surface oxygen contamination for p- and n-type GaN surfaces.

Though little or no comment on this issue is found in the open literature, it was determined that the additional surface oxidation of p-type GaN surfaces is due to the dopant activation anneal necessary in the processing of Mg-doped GaN films. In the processing

scheme for the GaN used in this study, the activation anneal is performed at 900 °C under a flowing N₂ ambient. While it has not been measured, presumably the partial pressure of O₂ in these conditions is not sufficiently low to prevent GaN oxidation. The temperature of 900 °C also represents the threshold temperature at which previous researchers observed significant oxidation of GaN in air.¹⁰ In Figure 8.12, the survey scans using Al K α radiation of four GaN films are shown: activated p-type GaN, n-type GaN, unactivated p-type GaN, and n-type GaN that had been subjected to the same annealing conditions after growth as an activate pGaN film. Note the relative intensities of the O KLL Auger series at ~ 970 eV; the two annealed samples are comparable, as are the two unannealed samples.

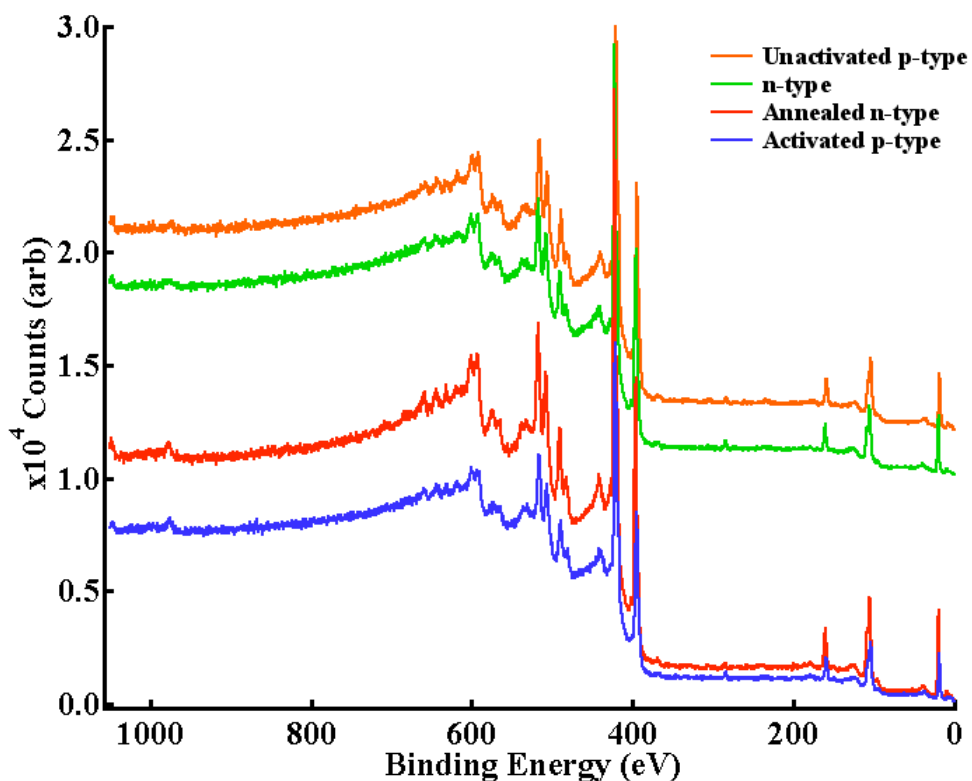


Figure 8.12: Survey scans using Al $K\alpha$ radiation illustrating the relative contamination differences arising from the p-type dopant activation anneal.

Additionally, Figure 8.13 shows the O 1s core level of an unactivated p-type GaN sample; it displays similar features ($\sim 37:63$ oxide:OH bonding) and relative intensity compared to the Ga $2p_{3/2}$ photoelectron line as a typical n-type or insulating GaN sample (see Figures 8.6 and 8.9), further demonstrating that the increased oxidation is due to the dopant activation anneal. Additionally, King *et al* suggest⁸ that the p-type GaN surface may be more prone to oxidation than n-type GaN, as the valence band lies at a higher energy, in close alignment with the energy of OH⁻ ions in aqueous solution.

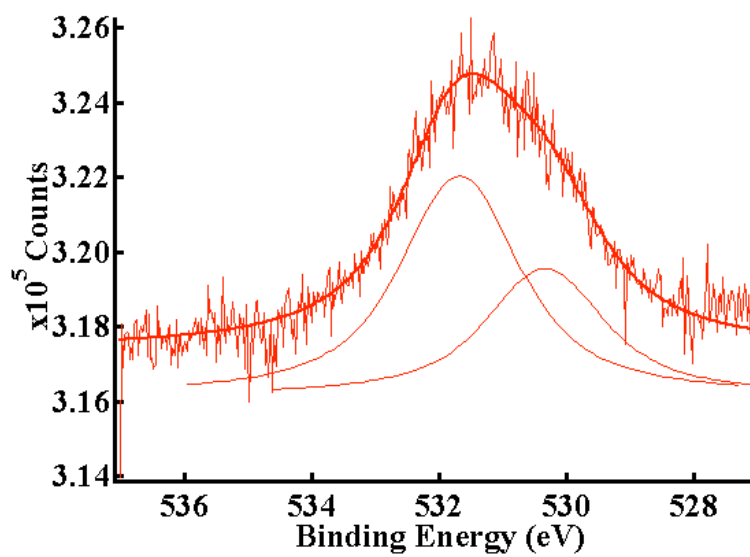


Figure 8.13: O 1s core level scan of an unactivated p-type GaN surface.

REFERENCES

- ¹ J. F. Moulder, W. F. Stickle, P. E. Sobol, and K. D. Bomben, *Handbook of X-ray Photoelectron Spectroscopy* (Perkin-Elmer Corporation, Eden Prairie, 1992).
- ² K. M. Tracy, W. J. Mecouch, R. F. Davis, and R. J. Nemanich, *Journal of Applied Physics* **94**, 3163-3172 (2003).
- ³ S. M. Widstrand, K. O. Magnusson, L. S. O. Johansson, E. Moons, M. Gurnett, H. W. Yeom, H. Miki, and M. Oshima, *Mrs Internet Journal of Nitride Semiconductor Research* **9**, (2004).
- ⁴ R. A. Oliver, C. Norenberg, M. G. Martin, A. Crossley, M. R. Castell, and G. A. D. Briggs, *Applied Surface Science* **214**, 1-10 (2003).
- ⁵ S. M. Widstrand, K. O. Magnusson, M. I. Larsson, L. S. O. Johansson, J. B. Gustafsson, E. Moons, H. W. Yeom, H. Miki, and M. Oshima, *Surface Science* **572**, 409-417 (2004).
- ⁶ C. I. Wu, A. Kahn, N. Taskar, D. Dorman, and D. Gallagher, *Journal of Applied Physics* **83**, 4249-4252 (1998).
- ⁷ Z. L. Fang, J. Y. Kang, and W. Z. Shen, *Nanotechnology* **20** (2009).
- ⁸ S. W. King, J. P. Barnak, M. D. Bremser, K. M. Tracy, C. Ronning, R. F. Davis, and R. J. Nemanich, *Journal of Applied Physics* **84**, 5248-5260 (1998).
- ⁹ M. D. Losego, Thesis, North Carolina State University, 2008.
- ¹⁰ S. D. Wolter, B. P. Luther, D. L. Waltemyer, C. Onneby, S. E. Mohny, and R. J. Molnar, *Applied Physics Letters* **70**, 2156-2158 (1997).

9. Conclusions and Future Work

In this thesis, the characteristics of several technologically and scientifically interesting oxide/GaN interfaces have been investigated, primarily spectroscopically. Additionally, several chemical and electronic aspects of oxide and GaN surfaces have been investigated individually. In this chapter, a set of conclusions are drawn, and suggestions for future work are made.

9.1 Conclusions

Rocksalt oxide/GaN interfaces were investigated using XPS by exploring two phenomena: the growth mode of thin films prepared via MBE, and the evolution of valence band offsets. Data collection and interpretation enable the following conclusions:

- By tracking the attenuation of the Ga $2p_{3/2}$ photoelectron line as the thickness of the rocksalt oxide film increased, the growth mode could be deduced. In the case of MgO on GaN, a three-dimensional (Volmer-Weber) growth mode was confirmed.
- The rate of attenuation pointed out that the MgO islands grow slowly over the GaN, not coalescing fully until ~ 12 nm of film growth.
- The data establishes a lower limit for MgO thickness in order to maintain a coherent buffer layer in GaN/ferroelectric structures, or a sound passivation layer in HEMT devices.

- By tracking the Ga 3d/Ga LMM Auger parameter as a function of film thickness, the possibility of a varying band lineup with film coalescence was eliminated.
- MgO/GaN band alignment was determined over the course of three different measurements to further rule out a thickness effect. The valence band offset was found to be 1.2 ± 0.2 eV, leading to a conduction band offset of 3.2 ± 0.2 eV. Such values are generally considered to be sufficient for mitigation of leakage current at elevated temperatures.
- Smooth MgO films are identified to be promising candidates for buffer layers in complex oxide-GaN devices.
- CaO was investigated in an analogous manner as MgO. The Ga $2p_{3/2}$ attenuation data suggests a Stranski-Krastanov growth mode. This data stands in distinct contrast to the case of MgO growth on GaN. The difference is likely a result of the decreased vapor pressure of Ca relative to Mg, leading to an increased interaction with the GaN substrate, and the increased reactivity of CaO with water under vacuum. The higher reactivity, and resulting adsorbed water and hydroxyl termination, reduces the driving force for surface faceting.
- The valence band offset between GaN and CaO is found to be 1.0 ± 0.2 eV, leading to a conduction band offset of 2.5 ± 0.2 eV. Again, these values are acceptable for limiting Schottky emission at high temperatures.
- The improved coalescence behavior and the sufficiently large band offsets suggest that CaO may be a more suitable buffer layer for GaN devices than MgO.

- The propensity of MgO and CaO to scavenge water from vacuum environments relevant to typical thin film processes was investigated by XPS using the O 1s photoelectron line after several *in-vacuo* exposures. The polycrystalline MgO films exhibited higher stability than the CaO films. MgO hydroxide coverage appeared to saturate at approximately 1 monolayer, not changing significantly after a 3 hour UHV exposure and a 1 hour exposure to a flowing H₂O/O₂ mixture. CaO hydroxide coverage also appeared to saturate, at 3 monolayers after UHV storage.
- The surface hydroxylation was found to be reversible by high vacuum anneals.
- The observations of higher CaO reactivity and faster CaO coalescence appear to be related, since the hydroxylation stabilizes the rocksalt {111} face (see Chapter Seven) which in turn eliminates a driving force for surface faceting and 3-D growth. Thus we hypothesize that using the flux controlling capabilities of MBE, it may be possible to grow smooth MgO films under the presence of some partial pressure of water.
- The GaN surface stoichiometry of as-grown films is consistently, significantly Ga-rich.
- GaN surfaces were exposed to a variety of chemical etchants known to alter the electronic properties of subsequent device structures. None of the pretreatments were found to alter the Ga:N ratio in a manner visible to XPS, and no affect on the surface topography was identified.
- A minor difference in the GaN valence band spectrum was observed which implies some reduction in surface states, but further investigation here is required.

- p-type GaN surface was found to consistently exhibit nm-scale coverages of an oxide phase, due to the high-temperature Mg dopant activation anneals performed directly after growth.

9.2 Future Work

Further investigations of experiments performed in this thesis should concentrate primarily on the work presented in Chapter Eight; the data shown there is preliminary in nature and should be elaborated upon. The GaN surface stoichiometry data would benefit from additional investigation, especially in terms of elucidating the nature of the excess Ga, further ways to control the stoichiometry either during GaN growth or by subsequent processing, and investigating the effect the excess Ga has on electrical behavior of GaN-oxide stacks. The GaN surface stoichiometry may be controllable by modifying the specifics of the GaN growth termination and cool-down, for example. If not, further post-processing experiments (wet chemistry, vacuum/ NH_3 anneals, or polishing) should be investigated. The impact on electrical behavior can be explored by fabricating MOS capacitors and evaluating leakage current and interface state density, and more advanced experiments involving the ferroelectric-GaN interface can also be explored. Such experiments will require good understanding of the nature of the Ga excess, as well as the ability to control its extent.

The observation of improved coalescence behavior of CaO, and its concomitant increased surface reactivity, present an interesting possibility for MgO growth. If a hydroxyl-terminated $\{111\}$ MgO film can be grown, it may coalesce more rapidly than the bulk-

terminated {100} films previously grown, as the driving force for faceting would be reduced. If such a microstructure could be realized, the larger band offsets of MgO on GaN could be utilized, while improving the electrical behavior of the MgO, which is currently limited by a high population of grain boundaries. MBE experiments would be ideal for this investigation, as it provides the ability to closely control fluxes of cation species, oxidants, and water-containing species, combined with *in-situ* characterization using RHEED.

Appendix

Band offsets of SrTiO₃, GdScO₃/SrTiO₃, and LaAlO₃/SrTiO₃ epitaxial heterostructures with (0001) GaN

J. F. Ihlefeld,^{1,2,†)} H. S. Craft,³ T. Heeg,¹ R. Collazo,³ S. Mita,³ Z. Sitar,³ J-P. Maria,³ R. Ramesh,^{2,4} and D. G. Schlom^{1,‡)}

¹Department of Materials Science and Engineering, Cornell University, Ithaca, New York 14853

²Department of Materials Science and Engineering, University of California, Berkeley, California 94720

³Department of Materials Science and Engineering, North Carolina State University
Raleigh, North Carolina 27695

⁴*Department of Physics, University of California, Berkeley, California 94720*

^{†)} Present address: Sandia National Laboratories, Albuquerque, NM 87185

^{‡)} Electronic mail: schlom@cornell.edu

Epitaxial (111) SrTiO₃ films and (011) GdScO₃ / (111) SrTiO₃ and (0001) LaAlO₃ / (111) SrTiO₃ bilayers were deposited on (0001)-oriented Ga-polar *n*-type GaN by reactive molecular-beam epitaxy. Band offsets were determined by x-ray photoelectron spectroscopy. The band offsets between SrTiO₃ and GaN are $\Delta E_v = 0.1 \pm 0.2$ eV and $\Delta E_c = -0.2 \pm 0.2$ eV. The band offsets between GdScO₃ and GaN with an intervening SrTiO₃ layer are $\Delta E_v = 0.4 \pm 0.2$ eV and $\Delta E_c = 2.0 \pm 0.2$ eV. The band offsets between LaAlO₃ and GaN with an intervening SrTiO₃ layer are $\Delta E_v = -0.3 \pm 0.2$ eV and $\Delta E_c = 2.5 \pm 0.2$ eV.

Integrating ferroelectric oxides with wide band-gap semiconductors including GaN and AlGaIn/GaN high electron mobility transistors (HEMTs) is of interest for multifunctional sensors¹ and high-temperature, high-voltage, and high-current transistor applications.² While several successful integration examples exist,³⁻¹² additional challenges must be surpassed to realize efficient and reliable devices utilizing ferroelectric polarization transistor gate control. One such challenge is the similar band-gaps of the ferroelectrics of interest including (Ba,Sr)TiO₃ (~3.0-3.2 eV),^{13,14} Pb(Zr,Ti)O₃ (~3.4 eV),¹⁵ and BiFeO₃ (~2.8 eV)¹⁶ in comparison to GaN (~3.4 eV),¹⁷ which may allow for undesirable gate-drain leakage and diminished ferroelectric polarization retention. Identification of compatible wide band-gap barriers and their band offsets with GaN are therefore of interest. To date there have been studies on rocksalt oxides MgO,^{18,19} CaO,²⁰ and Mg_{0.5}Ca_{0.5}O,²¹ rutile (TiO₂),²² and the bixbyites Sc₂O₃²³ and Gd₂O₃.²⁴ Missing are studies of the band offsets between perovskite oxides and GaN. As the majority of ferroelectric oxides are perovskites, examination of wide band-gap perovskite buffer layers is pertinent. Two potential perovskite insulating barriers are GdScO₃ and LaAlO₃, which have band-gaps of 5.8 eV²⁵ and 5.6 eV, respectively.²⁶ In this work we have studied the band offsets of SrTiO₃, GdScO₃/SrTiO₃, and LaAlO₃/SrTiO₃ epitaxial heterostructures with *n*-type (0001)-oriented GaN.

Oxide heterostructures were deposited on 3 μm thick, Ga-polar, silicon-doped, *n*-type (0001) GaN substrates grown by metal-organic chemical vapor deposition on sapphire²⁷ and

0.5 μm thick, Ga-polar, silicon-doped *n*-type GaN from a commercial supplier (Lumilog). Prior to oxide heterostructure growth, the GaN surfaces were exposed to 1:1 HCl:H₂O and 1:99 buffered-HF:H₂O solutions for 1 minute each followed by de-ionized water rinses to minimize surface carbon contamination.²⁸ Oxide films were deposited within a Veeco 930 molecular-beam epitaxy (MBE) system described elsewhere.²⁹ SrTiO₃ films were deposited as reported previously by reacting SrO with (100)-oriented TiO₂ to form a (111)-oriented SrTiO₃ film.^{8,9} Approximately 0.6 nm of (100)-oriented TiO₂ (equivalent to 5 monolayers (MLs) of Ti in the (111)-oriented SrTiO₃ structure) was deposited on the (0001) GaN surface at a substrate temperature of ~ 600 °C and a molecular oxygen background pressure of 1×10^{-6} Torr. An SrO dose corresponding to 4 MLs in the SrTiO₃ structure was subsequently deposited under identical conditions and allowed to react with the TiO₂ to form (111)-oriented SrTiO₃. The resulting thickness of the SrTiO₃ film was approximately 2 nm. For band offset measurements an additional 40 nm thick sample was prepared by depositing alternating individual MLs of SrO₃-Ti-SrO₃-Ti- SrO₃-... on top of the 2 nm reacted layer.

Multiple MBE routes were employed to attempt to deposit epitaxial GdScO₃ and LaAlO₃ directly on the (0001) GaN surface. All attempts resulted in amorphous films by RHEED, similar to results observed in films deposited by electron-beam evaporation.³⁰ Epitaxial (0001)-oriented BiFeO₃ films on GaN has previously been demonstrated using a 2 nm thick (111)-oriented SrTiO₃ buffer layer.^{8,9} The same template technique was used to deposit both (111)_{*p*}-oriented GdScO₃ and LaAlO₃ (where the *p* subscript denotes

pseudocubic notation) films. Films were deposited by supplying alternating doses of $\text{GdO}_3\text{-Sc-GdO}_3\text{-Sc}\cdots$ and $\text{LaO}_3\text{-Al-LaO}_3\text{-Al}\cdots$ for GdScO_3 and LaAlO_3 films, respectively. A molecular oxygen background pressure of $\sim 5 \times 10^{-7}$ Torr and a substrate temperature of $\sim 700^\circ\text{C}$ were used for the growth of GdScO_3 . A (10% O_3 + 90% O_2) background pressure of $\sim 5 \times 10^{-6}$ Torr and substrate temperature of $\sim 680^\circ\text{C}$ were used for the growth of LaAlO_3 . Figure 1 shows representative reflection high-energy electron diffraction (RHEED) patterns along the substrate $\langle 11\bar{2}0 \rangle$ azimuth for the growth of TiO_2 , SrTiO_3 , $\text{LaAlO}_3 / \text{SrTiO}_3$, and $\text{GdScO}_3 / \text{SrTiO}_3$ on (0001) GaN. The patterns of the SrTiO_3 , GdScO_3 , and LaAlO_3 are in transmission indicating a rough growth surface as has been previously observed for the growth of perovskites in a $\langle 111 \rangle_p$ direction.^{8,31} Additional spots are observed in the perovskite transmission patterns indicative of in-plane 180° rotation twins and are identified by arrows. Figure 2(a) shows a θ - 2θ x-ray diffraction (XRD) scan of a 40 nm $\text{LaAlO}_3 / 2$ nm $\text{SrTiO}_3 / (0001)$ GaN heterostructure. The LaAlO_3 film is phase-pure and (0001)-oriented (using hexagonal indices, space group #167 ($R\bar{3}c$)). XRD of the 40 nm $\text{GdScO}_3 / 2$ nm $\text{SrTiO}_3 / (0001)$ GaN heterostructure (not shown) revealed a preferred (011) orientation (using the standard crystallographic setting, space group #62 ($Pnma$)). Figure 2(b) shows azimuthal ϕ scans for the GaN $10\bar{1}1$ and LaAlO_3 $20\bar{2}4$ families of peaks. The LaAlO_3 $20\bar{2}4$ family is equivalent to the 002_p family. Six distinct peaks are observed for LaAlO_3 indicating that the film is epitaxial and that it also contains 180° in-plane rotation twins, verifying the twinning observed in the RHEED patterns. In-plane twins have been observed for other pseudocubic and cubic oxides deposited on hexagonal substrates.^{8,32-35}

The twin structure has been replicated from the SrTiO₃ buffer layer as observed previously in BiFeO₃ / SrTiO₃ / TiO₂ / GaN heterostructures.⁸

X-ray photoelectron spectra (XPS) were collected within a VG Clam II semi-hemispherical electron spectrometer equipped with a dual anode x-ray source. Al K_α radiation (1486.6 eV) and a spectrometer pass energy of 20 eV were used. The positions of photoelectric lines were established using the Voigt peak shapes with an equal width and shape constraint. Valence band maxima (VBM) were determined by the linear intercept technique, in which fits are applied to the leading edge of the valence band and to the background signal in the band-gap region. Band offset measurements were performed in the manner described by Waldrop and Grant.³⁶ Offsets were determined in accordance with:

$$\Delta E_v^{\text{SrTiO}_3/\text{GaN}} = (\text{Ga}_{3d} - \text{GaN}_{\text{VBM}})_{\text{GaN}} - (\text{Ga}_{3d} - \text{Ti}_{3p})_{\text{SrTiO}_3/\text{GaN}} - (\text{Ti}_{3p} - \text{SrTiO}_3_{\text{VBM}})_{\text{SrTiO}_3}, \quad (1)$$

$$\Delta E_v^{\text{LaAlO}_3/\text{SrTiO}_3} = (\text{Ti}_{3p} - \text{SrTiO}_3_{\text{VBM}})_{\text{SrTiO}_3} - (\text{Ti}_{3p} - \text{Al}_{2p})_{\text{LaAlO}_3/\text{SrTiO}_3} - (\text{Al}_{2p} - \text{LaAlO}_3_{\text{VBM}})_{\text{LaAlO}_3}, \quad (2)$$

$$\Delta E_v^{\text{GdScO}_3/\text{SrTiO}_3} = (\text{Ti}_{3p} - \text{SrTiO}_3_{\text{VBM}})_{\text{SrTiO}_3} - (\text{Ti}_{3p} - \text{Sc}_{3p})_{\text{GdScO}_3/\text{SrTiO}_3} - (\text{Sc}_{3p} - \text{GdScO}_3_{\text{VBM}})_{\text{GdScO}_3}, \quad (3)$$

where the Ga 3*d* peak was measured on a bare substrate. The Ti 3*p*, Al 2*p*, and Sc 3*p* peaks were measured on 40 nm thick films to screen photoelectrons originating from the underlying substrate. The second term on the right-hand side of Eqns. (1)-(3) was determined on 2 nm thick films to allow sufficient electron transparency for collection of both core level energies.

In the case of LaAlO_3 and GdScO_3 the valence band offsets were calculated with respect to the SrTiO_3 layer. Conduction band offsets were calculated by:

$$\Delta E_c^{\text{SrTiO}_3/\text{GaN}} = E_g^{\text{SrTiO}_3} - E_g^{\text{GaN}} - \Delta E_v^{\text{SrTiO}_3/\text{GaN}}, \quad (4)$$

$$\Delta E_c^{\text{LaAlO}_3/\text{SrTiO}_3} = E_g^{\text{LaAlO}_3} - E_g^{\text{SrTiO}_3} - \Delta E_v^{\text{LaAlO}_3/\text{SrTiO}_3}, \quad (5)$$

$$\Delta E_c^{\text{GdScO}_3/\text{SrTiO}_3} = E_g^{\text{GdScO}_3} - E_g^{\text{SrTiO}_3} - \Delta E_v^{\text{GdScO}_3/\text{SrTiO}_3}, \quad (6)$$

for $\text{SrTiO}_3/\text{GaN}$, $\text{LaAlO}_3/\text{SrTiO}_3$, and $\text{GdScO}_3/\text{SrTiO}_3$, respectively.

Figure 3 shows the representative spectra used to determine the core levels and VBM. The core levels Ga $3d$, Ti $3p$, and Al $2p$ are fit using two peaks to account for some asymmetry.¹⁹ The Sc $3p$ photoelectron line was fit using one peak; the feature seen in Fig. 3(d) at ~ 29 eV was included as a background feature. Due to spectral overlap of the 2 nm thick SrTiO_3 film with the 40 nm thick GdScO_3 film, charge referencing with adventitious carbon, as has been conducted in previous studies,²⁰ was not possible. Therefore results cannot be provided on an absolute energy scale, nor can band bending be determined. As the band offset values are calculated from the energy difference between features, however, these are not affected by static charging. Absolute energies and band bending were resolved for the $\text{LaAlO}_3 / \text{SrTiO}_3$ interfaces utilizing the carbon $1s$ photoelectron line for charge correction. Results of the calculated band offsets are summarized in Table I and the schematic band diagrams are shown in Fig. 4. It is observed that there is approximately 0.3 eV positive (lower energy) band bending in SrTiO_3 at the $\text{LaAlO}_3 / \text{SrTiO}_3$ interface. This is opposite in direction to that observed for LaAlO_3 deposited on TiO_2 -terminated (001)-

oriented SrTiO₃.³⁷ We do not understand the cause of this difference, but do note that the interface discontinuity values for our work and the previous study are in agreement within the measurement uncertainty. Regardless, the -0.4 eV band offset makes LaAlO₃ / SrTiO₃ heterostructures an unattractive choice as an insulating barrier layer between GaN and a lower band-gap ferroelectric. GdScO₃, however, possesses a positive valence band offset and a large conduction band offset and therefore is a more promising candidate, particularly for *n*-type GaN devices. It is prudent to mention the possibility of GaN states influencing the band alignments of the oxide bilayers given the thin SrTiO₃ template layer. We cannot discount any effect originating from this; however, in evaluating the Ga 3*d* and Sc 3*p* core level energies on the thinnest bilayer we observe agreement with the valence band offset calculated from the GaN/SrTiO₃ and SrTiO₃/GdScO₃ interfaces independently.

In summary, epitaxial SrTiO₃ films and LaAlO₃ / SrTiO₃ and GdScO₃ / SrTiO₃ bilayers have been deposited on (0001)-oriented GaN. Band offsets of each structure were measured using XPS. It was determined that GdScO₃ / SrTiO₃ heterostructures possess sufficient valence and conduction band offsets for *n*-type GaN devices. The integration of a wide band-gap perovskite oxide with GaN provides a promising step toward realizing devices integrating ferroelectric oxides with wide band-gap semiconductors. These wide band-gap gate oxides are also of interest for *n*-channel metal-oxide-semiconductor heterostructure field-effect transistors (MOSHETs).

This work was supported by the Office of Naval Research through grants N00014-03-1-0721 and N00014-04-1-0426 monitored by Dr. Colin Wood, by NSF through grants DMR-0820404 and IIP-0737759, and by the Director, Office of Science, Office of Basic Energy Sciences, Materials Science and Engineering Division, of the U.S. DoE under Contract No. DE-AC02-05CH11231. The authors acknowledge informative discussions with Professors Jasprit Singh and Yuh-Renn Wu.

REFERENCES

- ¹ Y. R. Wu and J. Singh, *IEEE Trans. Electron Devices* **52** (2), 284-293 (2005).
- ² M. Singh, Y. R. Wu, and J. Singh, *Solid-State Electron.* **47** (12), 2155-2159 (2003).
- ³ V. Fuflyigin, A. Osinsky, F. Wang, P. Vakhutinsky, and P. Norris, *Appl. Phys. Lett.* **76** (12), 1612-1614 (2000).
- ⁴ W. A. Doolittle, G. Namkoong, A. G. Carver, and A. S. Brown, *Solid-State Electron.* **47** (12), 2143-2147 (2003).
- ⁵ C. R. Cho, J. Y. Hwang, J. P. Kim, S. Y. Jeong, S. G. Yoon, and W. J. Lee, *Jpn. J. Appl. Phys. Part 2* **43** (11A), L1425-L1428 (2004).
- ⁶ G. Namkoong, K. K. Lee, S. M. Madison, W. Henderson, S. E. Ralph, and W. A. Doolittle, *Appl. Phys. Lett.* **87** (17), 171107 (2005).
- ⁷ W. Cao, S. Bhaskar, J. Li, and S. K. Dey, *Thin Solid Films* **484** (1-2), 154-159 (2005).
- ⁸ A. Posadas, J. B. Yau, C. H. Ahn, J. Han, S. Gariglio, K. Johnston, K. M. Rabe, and J. B. Neaton, *Appl. Phys. Lett.* **87** (17), 171915 (2005).
- ⁹ I. Stolichnov, L. Malin, P. Mural, and N. Setter, *Appl. Phys. Lett.* **88** (4), 043512 (2006).
- ¹⁰ Y. Chye, T. Liu, D. Li, K. Lee, D. Lederman, and T. H. Myers, *Appl. Phys. Lett.* **88** (13), 132903 (2006).
- ¹¹ W. Tian, V. Vaithyanathan, D. G. Schlom, Q. Zhan, S. Y. Yang, Y. H. Chu, and R. Ramesh, *Appl. Phys. Lett.* **90** (17), 172908 (2007).
- ¹² S. Y. Yang, Q. Zhan, P. L. Yang, M. P. Cruz, Y. H. Chu, R. Ramesh, Y. R. Wu, J. Singh, W. Tian, and D. G. Schlom, *Appl. Phys. Lett.* **91** (2), 022909 (2007).
- ¹³ G. A. Cox, G. G. Roberts, and R. H. Tredgold, *Br. J. Appl. Phys.* **17** (6), 743-745 (1966).
- ¹⁴ M. Cardona, *Phys. Rev.* **140** (2A), A651-A655 (1965).
- ¹⁵ C. E. Land and P. S. Percy, *Info. Display J.* **13**, 20-23 (1977).

- ¹⁶ J. F. Ihlefeld, N. J. Podraza, Z. K. Liu, R. C. Rai, X. Xu, T. Heeg, Y. B. Chen, J. Li, R. W. Collins, J. L. Musfeldt, X. Q. Pan, J. Schubert, R. Ramesh, and D. G. Schlom, *Appl. Phys. Lett.* **92** (14), 142908 (2008).
- ¹⁷ R. Dingle, D. D. Sell, S. E. Stokowski, and M. Ilegems, *Phys. Rev. B* **4** (4), 1211-1218 (1971).
- ¹⁸ J. J. Chen, B. P. Gila, M. Hlad, A. Gerger, F. Ren, C. R. Abernathy, and S. J. Pearton, *Appl. Phys. Lett.* **88** (4), 042113 (2006).
- ¹⁹ H. S. Craft, R. Collazo, M. D. Losego, S. Mita, Z. Sitar, and J. P. Maria, *J. Appl. Phys.* **102** (7), 074104 (2007).
- ²⁰ H. S. Craft, R. Collazo, M. D. Losego, S. Mita, Z. Sitar, and J. P. Maria, *Appl. Phys. Lett.* **92** (8), 082907 (2008).
- ²¹ J. J. Chen, M. Hlad, A. P. Gerger, B. P. Gila, F. Ren, C. R. Abernathy, and S. J. Pearton, *J. Electron. Mater.* **36** (4), 368-372 (2007).
- ²² P. J. Hansen, V. Vaithyanathan, Y. Wu, T. Mates, S. Heikman, U. K. Mishra, R. A. York, D. G. Schlom, and J. S. Speck, *J. Vac. Sci. Technol. B* **23** (2), 499-506 (2005).
- ²³ J. J. Chen, B. P. Gila, M. Hlad, A. Gerger, F. Ren, C. R. Abernathy, and S. J. Pearton, *Appl. Phys. Lett.* **88** (14), 142115 (2006).
- ²⁴ T. S. Lay, Y. Y. Liao, W. H. Hung, M. Hong, J. Kwo, and J. P. Mannaerts, *J. Cryst. Growth* **278** (1-4), 624-628 (2005).
- ²⁵ T. Heeg, M. Wagner, J. Schubert, C. Buchal, M. Boese, M. Luysberg, E. Cicerrella, and J. L. Freeouf, *Microelectronic Engineering* **80**, 150-153 (2005).
- ²⁶ S. G. Lim, S. Kriventsov, T. N. Jackson, J. H. Haeni, D. G. Schlom, A. M. Balbashov, R. Uecker, P. Reiche, J. L. Freeouf, and G. Lucovsky, *J. Appl. Phys.* **91** (7), 4500-4505 (2002).
- ²⁷ R. Collazo, S. Mita, A. Aleksov, R. Schlessler, and Z. Sitar, *J. Cryst. Growth* **287** (2), 586-590 (2006).
- ²⁸ L. L. Smith, S. W. King, R. J. Nemanich, and R. F. Davis, *J. Electron. Mater.* **25** (5), 805-810 (1996).

- ²⁹ J. Lettieri, J. H. Haeni, and D. G. Schlom, *J. Vac. Sci. Technol., A* **20** (4), 1332-1340 (2002).
- ³⁰ G. Heidelberger, M. Roeckerath, R. Steins, M. Stefaniak, A. Fox, J. Schubert, N. Kaluza, M. Marso, H. Luth, and P. Kordos, in *Sixth International Conference on Advanced Semiconductor Devices and Microsystems*, edited by J. Breza, D. Donoval, and E. Vavrinsky (IEEE, Piscataway, NJ, 2006), pp. 241-244.
- ³¹ J. F. Ihlefeld, A. Kumar, V. Gopalan, D. G. Schlom, Y. B. Chen, X. Q. Pan, T. Heeg, J. Schubert, X. Ke, P. Schiffer, J. Orenstein, L. W. Martin, Y. H. Chu, and R. Ramesh, *Appl. Phys. Lett.* **91** (7), 071922 (2007).
- ³² H. S. Craft, J. F. Ihlefeld, M. D. Losego, R. Collazo, Z. Sitar, and J. P. Maria, *Appl. Phys. Lett.* **88** (21), 212906 (2006).
- ³³ M. D. Losego, S. Mita, R. Collazo, Z. Sitar, and J. P. Maria, *J. Vac. Sci. Technol. B* **25** (3), 1029-1032 (2007).
- ³⁴ M. D. Losego, S. Mita, R. Collazo, Z. Sitar, and J. P. Maria, *J. Cryst. Growth* **310** (1), 51-56 (2008).
- ³⁵ T. L. Goodrich, Z. Cai, M. D. Losego, J. P. Maria, L. F. Kourkoutis, D. A. Muller, and K. S. Ziemer, *J. Vac. Sci. Technol. B* **26** (3), 1110-1114 (2008).
- ³⁶ J. R. Waldrop and R. W. Grant, *Appl. Phys. Lett.* **68** (20), 2879-2881 (1996).
- ³⁷ K. Yoshimatsu, R. Yasuhara, H. Kumigashira, and M. Oshima, *Phys. Rev. Lett.* **101** (2), 026802 (2008).

Table A.1: Summary of band offsets determined for the heterostructures in this study.

Interface	ΔE_v	ΔE_c	E_g^{oxide}
SrTiO ₃ / GaN	0.1 ± 0.2 eV	-0.2 ± 0.2 eV	3.2 eV
LaAlO ₃ / SrTiO ₃	-0.4 ± 0.2 eV	2.5 ± 0.2 eV	5.6 eV
GdScO ₃ / SrTiO ₃	0.3 ± 0.2 eV	2.0 ± 0.2 eV	5.8 eV

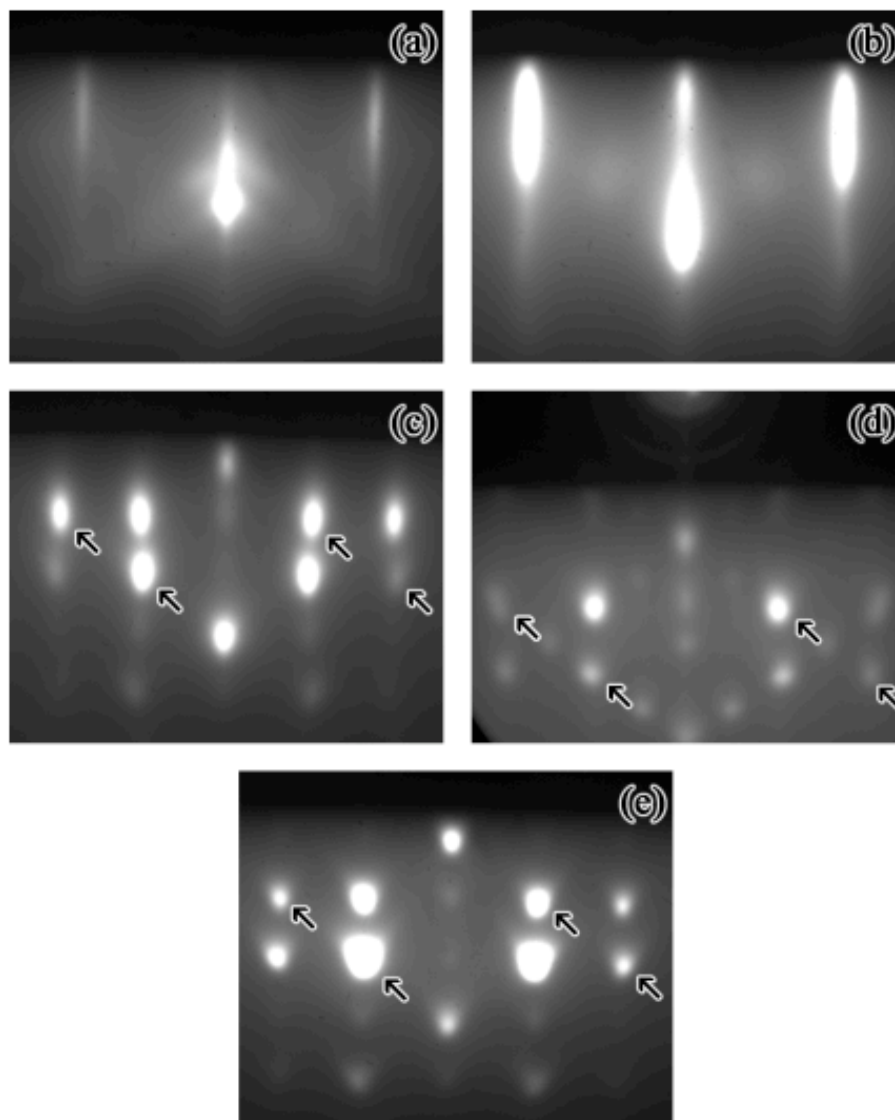


Figure A.1: RHEED images collected along the substrate $\langle 11\bar{2}0 \rangle$ azimuth of (a) GaN, (b) 5 ML (100)-oriented TiO_2 , (c) 2 nm (111)-oriented SrTiO_3 , (d) 40 nm $(111)_p$ -oriented GdScO_3 , and (e) 40 nm $(111)_p$ -oriented LaAlO_3 . Arrows indicate diffraction spots originating from in-plane twins.

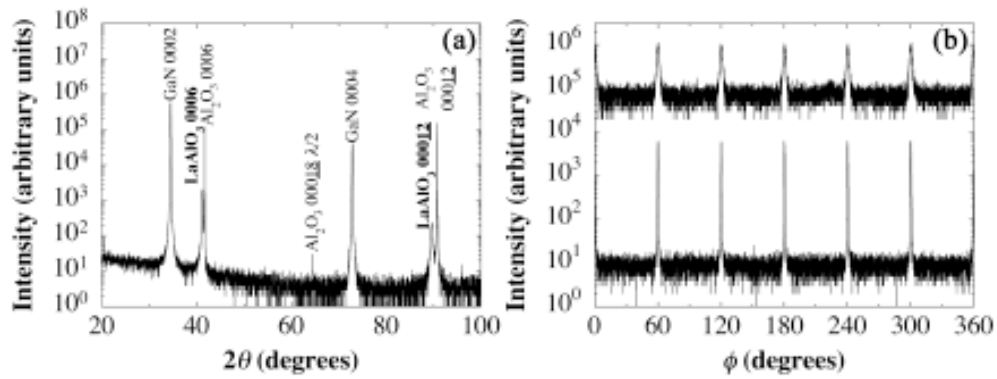


Figure A.2: (a) θ - 2θ and scan of a 40nm LaAlO₃ / 2nm SrTiO₃ / (0001)-oriented GaN heterostructure. (b) Azimuthal ϕ -scans of the LaAlO₃ 20 $\bar{2}$ 4 family (top) ($\chi=35.33^\circ$) and GaN 10 $\bar{1}$ 1 family (bottom) ($\chi=28.03^\circ$) with 0° aligned parallel to the $[10\bar{1}0]$ GaN direction. $\chi=90^\circ$ aligns the diffraction vector to be perpendicular to the plane of the substrate. 6-fold symmetry of the LaAlO₃ 20 $\bar{2}$ 4 family verifies 180° in-plane twinning.

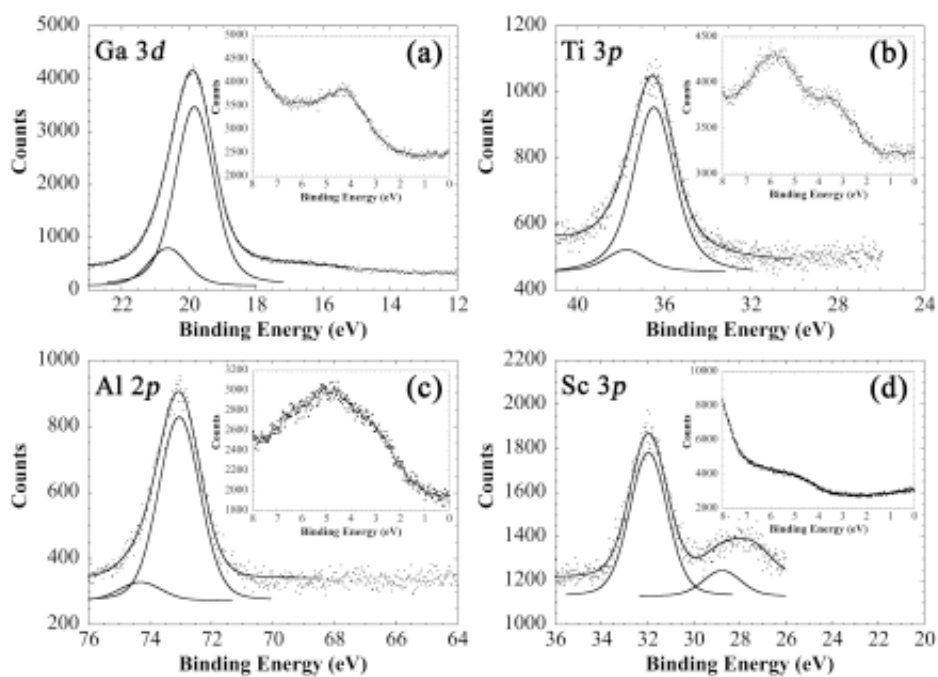


Figure A.3: X-ray photoelectron spectra of the (a) Ga 3*d*, (b) Ti 3*p*, (c) Al 2*p*, and (d) Sc 3*p* photoelectron lines. Insets show the respective valence band maxima for GaN, SrTiO₃, LaAlO₃, and GdScO₃.

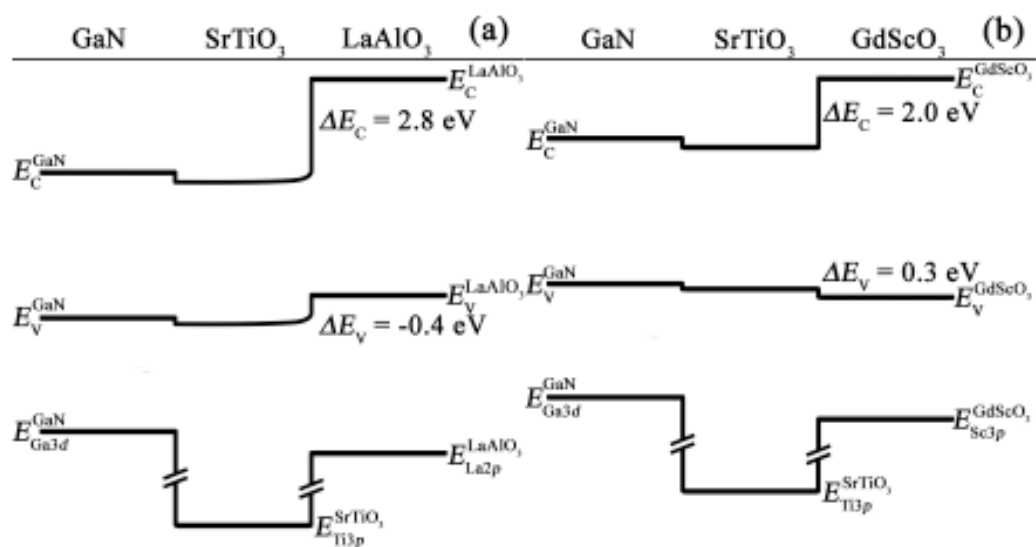


Figure A.4: Simplified schematic band diagram of the (a) LaAlO₃ / SrTiO₃ / GaN interface and (b) GdScO₃ / SrTiO₃ / GaN interface.